(Al,Ga,In)N heterostructures grown along polar and non-polar directions by plasma-assisted molecular beam epitaxy

DISSERTATION

zur Erlangung des akademischen Grades
doctor rerum naturalium
(Dr. rer. nat.)
im Fach Physik

eingereicht an der
Mathematisch-Naturwissenschaftlichen Fakultät I
Humboldt-Universität zu Berlin

von
Herrn Dipl.-Phys. Patrick Waltereit
geboren am 7.12.1971 in Münster

Präsident der Humboldt-Universität zu Berlin:
Prof. Dr. Jürgen Mlynek

Dekan der Mathematisch-Naturwissenschaftlichen Fakultät I:
Prof. Dr. Bernhard Ronacher

Gutachter:

1. Prof. Dr. Klaus H. Ploog
2. Prof. Dr. Fritz Henneberger
3. Prof. Dr. Friedhelm Bechstedt

PAUL-DRUDE-INSTITUT FÜR FESTKÖRPERELEKTRONIK BERLIN
2001

eingereicht am:	26. 1. 2001
Tag der mündlichen Prüfung:	11. 7. 2001

Abstract

In this work, we investigate the synthesis of wurtzite (Al,Ga,In)N heterostructures by plasma-assisted molecular beam epitaxy. The layers are grown along the polar [0001] and the non-polar [$1\bar{1}00$] direction on SiC(0001) and γ-LiAlO$_2$(100) substrates, respectively. We examine the impact of deposition conditions on the structural, morphological, optical, vibrational and electrical properties of the films.

An introduction is given to the most important properties of wurtzite nitride semiconductors: strain and electrical polarization fields of a magnitude not found in other III-V semiconductors. Particular emphasis is paid on [0001] and [$1\bar{1}00$] oriented layers. In order to correctly account for these phenomena in the samples under investigation, an efficient model for the dynamical simulation of x-ray diffraction (XRD) profiles is formulated and presented for wurtzite and zincblende crystals.

The deposition of GaN buffer layers on two substrates, SiC(0001) and γ-LiAlO$_2$(100), is discussed. The conventional polar [0001] direction is obtained on SiC(0001) substrates. A new degree of freedom for GaN epitaxy is demonstrated by the growth of GaN along a non-polar direction, namely, [$1\bar{1}00$] on γ-LiAlO$_2$(100). An *in-situ* strategy for the reproducible growth of these GaN buffers is developed based on reflection high-energy electron diffraction (RHEED). The films are single-phase within the detection limit of high-resolution XRD and exhibit smooth surface morphologies well suited for subsequent growth of heterostructures. The structural properties of these samples are shown to be very sensitive to substrate preparation before growth. Smooth and clean SiC(0001) substrates result in excellent structural properties of GaN(0001) layers whereas GaN($1\bar{1}00$) films still suffer from the inferior morphological and chemical quality of γ-LiAlO$_2$(100) substrates.

Identically designed GaN / (Al,Ga)N multiple quantum wells (MQWs) are deposited on these two types of buffer layers. Significant differences in recombination due to the different orientations of the polar c-axis with respect to the growth direction are detected in photoluminescence (PL). It is demonstrated that flat-band conditions are established in [$1\bar{1}00$] oriented wells whereas strong electrostatic fields have to be taken into account for the [0001] oriented wells. Consequently, the transition energy of the [0001] oriented wells is red-shifted with respect to the [$1\bar{1}00$] oriented wells. Furthermore, [0001] oriented wells exhibit significantly prolonged PL decay times. These results are in quantitative agreement with theoretical predictions based on self-consistent effective-mass Schrödinger-Poisson calculations of the band profiles and wave functions. Finally, while the emission from [0001] oriented wells is isotropic, the emission from [$1\bar{1}00$] oriented wells is strongly polarized ($>$90%) normal to the [0001] axis in sound agreement with the different valence band structures of the wells.

The growth of (In,Ga)N / GaN MQWs is studied. Massive In surface segregation (evidenced by RHEED, XRD, secondary-ion mass-spectrometry and PL) is shown to result in top-hat profiles and is therefore a zeroth order process instead of a first order process as observed for other materials systems. In segregation during metal-stable growth results in quantum wells with poor electron-hole wavefunction overlap since the actual well width is much larger than the intended one. Reduction of In segregation by N-stable conditions is possible but inevitably delivers rough interfaces. A strategy for obtaining (In,Ga)N / GaN MQWs with smooth interfaces and high quantum efficiency is devised.

The radiative recombination from (In,Ga)N / GaN MQWs is examined. It is demonstrated that both compositional fluctuations and electrostatic fields have to be taken into account for a thorough understanding of the emission from these structures. The temperature dependence of the radiative decay time is measured to probe the dimensionality of the system. For a quantitative understanding, a rate-equation model is utilized for analyzing the data. For low temperatures, recombination is governed by localized states whereas for high temperatures extended states dominate. This analysis shows that the localization depth in these structures is below 25 meV.

Zusammenfassung

Thema dieser Arbeit ist die Synthese von hexagonalen (Al,Ga,In)N-Heterostrukturen mittels plasmaunterstützter Molekularstrahlepitaxie. Die Proben werden entlang der polaren [0001]-Richtung und der unpolaren $[1\bar{1}00]$-Richtung auf SiC(0001)- bzw. γ-LiAlO$_2$(100)-Substraten gewachsen. Der Einfluß der Wachstumsbedingungen auf die strukturellen, morphologischen, optischen, vibronischen und elektrischen Eigenschaften der Proben wird untersucht.

Im Vergleich zu den übrigen III-V-Halbleitern zeichnen sich die hexagonalen Nitride besonders durch die Größe ihrer Fehlpassungen und elektrischen Polarisationsfelder aus. Eine Einführung in diese beiden wichtigen Eigenschaften wird gegeben, insbesondere für [0001]- und $[1\bar{1}00]$-orientierte Schichten. Um Verspannungen und elektrische Polarisationsfelder in korrekter Art und Weise zu berücksichtigen, wird ein effizientes Modell zur dynamischen Simulation von Röntgenbeugungsprofilen formuliert und auf hexagonale sowie kubische Kristalle angewandt.

Die Synthese von GaN-Pufferschichten auf SiC(0001)- und γ-LiAlO$_2$(100)-Substraten wird diskutiert. Das GaN-Wachstum auf SiC(0001) erfolgt entlang der üblichen polaren [0001]-Richtung. Ein neuartiger Freiheitsgrad der GaN-Epitaxie wird durch das Wachstum von GaN entlang der unpolaren $[1\bar{1}00]$-Richtung auf γ-LiAlO$_2$(100) erreicht. Eine *in-situ* Strategie zur reproduzierbaren Abscheidung von GaN-Pufferschichten wird erarbeitet, die auf der Kontrolle der Wachstumsparameter durch Beugung von hochenergetischen Elektronen beruht. Die Schichten sind einphasig innerhalb der Nachweisgrenze von Röntgenbeugung und zeichnen sich durch glatte Oberflächen aus, die für das weitere Wachstum von Heterostrukturen gut geeignet sind. Es wird gezeigt, daß die strukturellen Eigenschaften der Pufferschichten sehr stark von der Substratpräparation abhängen. Ausgezeichnete strukturelle Eigenschaften werden auf sauberen und glatten SiC(0001)-Substraten erzielt, wogegen GaN$(1\bar{1}00)$-Filme unter der schlechteren Oberflächenqualität der γ-LiAlO$_2$(100)-Substrate leiden.

GaN / (Al,Ga)N-Multiquantenwells (MQWs) mit identischer Schichtfolge werden auf den beiden Sorten von GaN-Pufferschichten gewachsen. Wegen der verschiedenen Orientierungen der polaren c-Achse relativ zur Wachstumsrichtung treten in der Rekombination von Ladungsträgern erhebliche Unterschiede auf. Es wird gezeigt, daß in $[1\bar{1}00]$-orientieren Wells Flachbandbedingungen herrschen. Im Gegensatz dazu existieren starke elektrostatische Felder in [0001]-orientierten Wells. Daher ist die Übergangsenergie von [0001]-orientierten Wells rotverschoben relativ zur Übergangsenergie der $[1\bar{1}00]$-orientierten Wells. Weiterhin besitzen die [0001]-orientierten Wells sehr viel längere Zerfallszeiten in der Photolumineszenz (PL). Beide Ergebnisse sind in quantitativer Übereinstimmung mit theoretischen Vorhersagen, die auf selbstkonsistenten Berechnungen von Bandprofilen und Wellenfunktionen mittels der Poisson- und Schrödingergleichungen in der Effektivmassen-Näherung basieren. Die Emission der [0001]-orientierten Wells ist isotrop, während die Emission der $[1\bar{1}00]$-orientierten Wells stark ($>$90%) senkrecht zur [0001]-Richtung polarisiert ist. Diese Ergebnisse sind in sehr guter Übereinstimmung mit den unterschiedlichen Valenzbandstrukturen der Wells.

Das Wachstum von (In,Ga)N / GaN-MQWs wird untersucht. Massive Oberflächensegregation von In wird mit Beugung hochenergetischer Elektronen, Sekundärionenmassenspektrometrie, Röntgenbeugung und PL nachgewiesen. Rechteckige In-Profile belegen einen Segregationsmechanismus nullter Ordnung und nicht (wie bei anderen Materialsystemen beobachtet) einen erster Ordnung. Diese In-Segregation während des metallstabilen Wachstums resultiert in MQWs mit geringem Überlapp der Elektronen- und Lochwellenfunktionen, weil die Wells sehr viel dicker als beabsichtigt sind. Eine Verminderung der In-Segregation ist möglich durch N-stabiles Wachstum, führt jedoch zu rauhen Grenzflächen. Eine Strategie zum Wachstum von MQWs mit glatten Grenzflächen und hohen Quanteneffizienzen wird vorgestellt.

Die strahlende Rekombination von (In,Ga)N / GaN-MQWs wird diskutiert. Es wird gezeigt, daß sowohl Zusammensetzungsfluktuationen als auch elektrostatische Felder für ein eingehendes Verständnis der Rekombination berücksichtigt werden müssen. Die Temperaturabhängigkeit der strahlenden Lebensdauer wird gemessen, um die Dimensionalität des Systems aufzuklären. Für ein quantitatives Verständnis wird ein Ratengleichungsmodell zur Analyse der Daten benutzt. Bei niedrigen Temperaturen wird die Rekombination von lokalisierten Zustände geprägt, wohingegen ausgedehnte Zustände bei höheren Tenmperaturen dominieren. Diese Analyse zeigt, daß die Lokalisierungstiefe in diesen Strukturen unterhalb von 25 meV liegt.

Parts of this work have already been published:

P. Waltereit, O. Brandt, A. Trampert, M. Ramsteiner, M. Reiche, M. Qi, and K. H. Ploog, *Influence of AlN nucleation layers on growth mode and strain relief of GaN grown on 6H-SiC(0001)*, Appl. Phys. Lett. **74**, 3660 (1999).

P. Waltereit, O. Brandt, and K. H. Ploog, *Violet and blue emitting (In,Ga)N/GaN multiple quantum wells grown on* γ*-LiAlO*$_2$*(100) by RF plasma-assisted molecular beam epitaxy*, Appl. Phys. Lett. **75**, 2029 (1999).

O. Brandt, R. Muralidharan, P. Waltereit, A. Thamm, A. Trampert, H. von Kiedrowski, and K. H. Ploog, *Critical issues for the growth of high quality (Al,Ga)N/GaN and GaN/(In,Ga)N heterostructures on SiC(0001) by molecular beam epitaxy*, Appl. Phys. Lett. **75**, 4019 (1999).

O. Brandt, R. Muralidharan, A. Thamm, P. Waltereit, and K. H. Ploog, *Essential strategies for the growth of high-quality (Al,Ga)N/GaN and GaN/(In,Ga)N heterostructures on SiC(0001) by molecular beam epitaxy*, Proceedings 10th International Workshop on the Physics of Semiconductor Devices, Delhi (India) 1999, edited by V. Kumar and S. K. Agarwal (Allied Publishers Ltd., New Delhi, 2000), 1495–1506.

P. Waltereit, O. Brandt, M. Ramsteiner, and K. H. Ploog, *Growth of M-plane GaN/(Ga,In)N heterostructures: way out of the dilemma of electrical polarization in nitrides*, Proceedings 3rd SANKEN International Symposium on Advanced Nanoelectronics: Devices, Materials and Computing, Osaka (Japan) 2000, Memoirs of the ISIR Vol. 57, 171 2000.

O. Brandt, R. Muralidharan, A. Thamm, P. Waltereit, and K. H. Ploog, *Key issues for the growth of high-quality (Al,Ga)N/GaN and GaN/(In,Ga)N heterostructures by molecular beam epitaxy*, Proceedings 10th International Conference on Solid Films and Surfaces, Princeton (USA) 2000. Appl. Surf. Sci. **175**, 419 (2001).

P. Waltereit, O. Brandt, A. Trampert, H. T. Grahn, J. Menniger, M. Ramsteiner, M. Reiche, and K. H. Ploog, *Nitride semiconductors free of electrostatic fields for efficient white light-emitting diodes*, Nature **406**, 865 (2000).

P. Waltereit, O. Brandt, M. Ramsteiner, K. H. Ploog, R. Uecker, and P. Reiche, *Growth of M-plane GaN*$(1\bar{1}00)$ *on* γ*-LiAlO*$_2$*(100)*, J. Cryst. Growth **218**, 143 (2000).

P. Waltereit, O. Brandt, M. Ramsteiner, J. Ringling, A. Trampert, and K. H. Ploog, *Coexistence of electric fields and composition fluctuations in (In,Ga)N/GaN quantum wells grown on 6H-SiC(0001)*, 26th Internat. Symposium on Compound Semiconductors, Berlin (Germany) 1999, Int. Phys. Conf. Ser. No. 166, 453 (2000).

P. Waltereit, O. Brandt, M. Ramsteiner, and K. H. Ploog, *M-plane GaN*$(1\bar{1}00)$*: a way to evade polarization fields in nitrides*, Proc. 3rd International Symposium on Blue Laser and Light Emitting Diodes (ISBLLED), Zeuthen (Germany) 2000, phys. stat. sol. (a) **180**, 133 (2000).

K. H. Ploog, O. Brandt, R. Muralidharan, A. Thamm, and P. Waltereit, *Growth of high quality (Al,Ga,In)N heterostructures on SiC(0001) by both plasma-assisted and reactive MBE*, 27th Conference on the Physics and Chemistry of Semiconductor Interfaces, Salt Lake City (USA) 2000, J. Vac. Sci. Technol. B **18**, 2290 (2000).

B. Rau, P. Waltereit, O. Brandt, M. Ramsteiner, K. H. Ploog, J. Puls and F. Henneberger, *In-plane polarization anisotropy of the spontaneous emission of M-plane GaN/(Al,Ga)N quantum wells*, Appl. Phys. Lett. **77**, 3343 (2000).

P. Waltereit, O. Brandt, M. Ramsteiner, A. Trampert, H. T. Grahn, J. Menniger, M. Reiche, and K. H. Ploog, *M-plane GaN*$(1\bar{1}00)$ *grown on* γ*-LiAlO*$_2$*(100): nitride semiconductors free of internal electric fields*, 11th International Conference on Molecular Beam Epitaxy, Beijing (China) 2000, J. Cryst. Growth **227**, 437 (2001).

M. Giehler, M. Ramsteiner, P. Waltereit, O. Brandt, and K. H. Ploog, *Substrate dependent halfwidth and frequency of the* E_2*(high) phonon line in GaN studied by Raman spectroscopy*, J. Appl. Phys. **89**, 3634 (2001).

O. Brandt, P. Waltereit, and K. H. Ploog, *Determination of strain-state and composition of highly mismatched group-III nitride heterostructures by x-ray diffraction*, Phys. Rev. B (submitted).

H. T. Grahn, A. Thamm, P. Waltereit, O. Brandt, and K. H. Ploog, *Influence of internal electric fields on the carrier dynamics in GaN/(Al,Ga)N multiple quantum wells with different orientation and strain state*, International Workshop on Nitride Semiconductors, Nagoya (Japan) 2000, Jpn. J. Appl. Phys. (to be published).

B. Rau, J. Puls, F. Henneberger, P. Waltereit, O. Brandt, M. Ramsteiner, and K. H. Ploog, *Comparative study of the spontaneous and stimulated emission of M- and C-plane GaN/(Al,Ga)N quantum wells*, Proceedings of SPIE Vol. 4283 (to be published).

C. Cobet, N. Esser, J. T. Zettler, W. Richter, P. Waltereit, O. Brandt, K. H. Ploog, S. Peters, N. V. Edwards, O. P. A. Lindquist, and M. Cardona, *Optical properties of wurtzite AlGaN parallel and perpendicular to the optical axis*, Phys. Rev. B (to be published).

P. Waltereit, O. Brandt, K. H. Ploog, M. A. Tagliente, and L. Tapfer, *In-surface segregation during growth of (In,Ga)N/GaN multiple quantum wells by plasma-assisted molecular-beam epitaxy*, Phys. Rev. B (submitted).

P. Waltereit, O. Brandt, J. Ringling, and K. H. Ploog, *Electrostatic fields and compositional fluctuations in (In,Ga)N/GaN multiple quantum wells grown by plasma-assisted molecular beam epitaxy*, Phys. Rev. B (submitted).

S. Ghosh, P. Waltereit, O. Brandt, H. T. Grahn, and K. H. Ploog, *Polarization-dependent spectroscopic study of M-plane GaN on* γ*-LiAlO*$_2$, Appl. Phys. Lett. (submitted).

P. Waltereit, O. Brandt, K. H. Ploog, M. A. Tagliente, and L. Tapfer, *In-surface segregation during growth of (In,Ga)N/GaN multiple quantum wells by plasma-assisted molecular-beam epitaxy*, Proc. 4th International Conference on Nitride Semiconductors (ICNS), Denver (USA) 2001, phys. stat. sol. (to be published).

Patent application:

P. Waltereit, O. Brandt, and K. Ploog, *Highly efficient UV emitter on the basis of hexagonal nitrides*, European Patent Application Nr. PCT/EP00/11044.

Contents

1 Introduction

General The 20th century has been coined the age of solid-state-electronics, as the replacement of vacuum tubes with transistors had revolutionary impact on the economic and sociological aspects of our society. At the advent of the 21st century, an analogous technological transition takes place which is culminating in the age of solid-state photonics. Modern communication technology has been made possible by optoelectronic devices, such as light-emitting diodes (LEDs) and laser diodes (LDs). Furthermore, Edison's fragile and bulky light bulb is beginning to be replaced by rugged and compact solid state lamps based on light-emitting diodes (LEDs). In fact, initiators of these two revolutions (Z. Alferov, J. Kilby and H. Kroemer) have been awarded with the physics Nobel prize 2000.

The first LEDs were demonstrated by General Electric in 1962 and commercialized in 1968 by Monsanto and Hewlett-Packard. However, throughout the 1970's and 1980's, the electrical-to-optical power efficiency of these devices was well below that of conventional incandescent lamps (12 lm / W). Moreover, only group-III arsenides and phosphides were utilized as LED materials thus restricting the available colors from red to green. Therefore, the use of these low brightness LEDs was limited to indoor indicator applications. During the last decade, however, the technology of LEDs has improved remarkably in two ways. First, higher conversion efficiencies (more than 100 lm / W for red LEDs) are obtained. Second, the entire visible spectrum is now covered including green (30 lm / W) and blue (10 lm / W).

These high brightness LEDs have reached the status of illuminators, hence, making them (in the case of red LEDs) superior to the most efficient conventional light sources such as halogen and fluorescent lamps (70 lm / W). The replacement of conventional light sources by LEDs will have vast economic and ecological consequences. At present, the total value of LEDs shipped worldwide amounts to $2 billion, one quarter being high brightness LEDs. [1] The replacement of all traffic lights by LEDs would save around 2.5 billion kWh annually in the USA. [2] White LEDs, as used for lighting applications, are realized either by combining red, green and blue LEDs or by employing a blue / ultraviolet (UV) LED which excites a phosphor to achieve the white color impression. Short-wavelength LDs pave the way to additional important applications, namely data storage and color printing / copying. Data storage densities and printer resolutions scale inversely with the square of the LD wavelength. Many other potential applications for short wavelength devices can be envisaged, such as, e.g., solar-blind photo-detectors, x-ray detectors or accousto-optical modulators.

Prime candidates for all of these short wavelength applications are the group-III nitrides (Al,Ga,In)N whose band gap can be continuously tuned from the ultraviolet (6.1 eV for AlN) to the red (1.8 eV for InN). Moreover, their excellent thermal, mechanical and chemical stabilities make them ideal even for applications in hostile environments.

In the following, a brief history of the group-III nitrides is given. GaN was synthesized for the first time by Johnson *et al.* [3] in 1932 by passing ammonia over hot Ga. This method produced small GaN needles and platelets. The other nitride semiconductors, AlN and InN, were fabricated in 1928 by Tiede *et al.* [4] and in 1938 by Juza *et al.* [5], respectively. The first epitaxial growth of GaN was achieved in 1969 by Maruska and

Tietjen [6] by a chloride vapor transport technique to obtain large-area layers of GaN on sapphire. Pankove *et al.* [7] realized the first electroluminescence from GaN. They employed an Zn doped n-type GaN metal-insulator-semiconductor diode that could emit either blue, green, yellow or red light depending on the Zn doping level. However, the efficiency of these devices was very low. The fabrication of actual pn-junctions was impeded by the fact that GaN was always highly n-type, even when not deliberately doped. The first p-type doped GaN was reported by Akasaki *et al.* [8] in 1988 and Amano *et al.* [9] in 1989 after electron beam treatment of Mg doped GaN. Further development of the nitrides is unthinkable without Shuji Nakamura from Nichia Chemicals (Japan) leading to the commercialization of ultraviolet, blue and green high-brightness LEDs [10] in 1993 and finally blue/ultraviolet continuous-wave injection LDs [10] in 1996. It should be noted here that the lifetime of these laser (more than 10,000 h) well exceeds that (below 400 h) of blue-green lasers based on II-VI compounds.

Group-III nitrides are usually grown by two different techniques, either metal-organic chemical vapor deposition (MOCVD) or molecular beam epitaxy (MBE). For a long time, MOCVD delivered crystals having a better overall quality. The inferior quality of MBE grown material mainly originated from technological issues. In particular, nitrogen sources for MBE were very inefficient and of rather low purity. At the time of starting this PhD project (March 1998), group-III nitrides grown by MBE exhibited very rough interfaces and surfaces, high dislocation densities as well as poor optical and electrical data.

However, in the last two years, MBE has become a competitive technique for electronic device applications of nitrides. In fact, the best mobilities of GaN/(Al,Ga)N two-dimensional electron gases were reported for MBE grown samples. [11] In contrast, the field of nitride optoelectronics is still controlled by MOCVD.

Despite the successful realization of high brightness LEDs and injection LDs, there is still a lack of knowledge about many fundamental properties of nitrides. Generally, the impact of growth conditions of (Al,Ga,In)N on the materials properties is still under debate. (In,Ga)N/GaN multiple quantum wells (MQWs) are used in LEDs and LDs, but only little insight into the actual structural properties of these MQWs, in particular their interfaces, has been gained yet. Moreover, the optical properties of these structures are still controversially discussed in terms of compositional fluctuations and/or strong electrostatic fields.

The foundation for the tailored growth and the understanding of properties of thin layers is the study of their fundamental growth processes. Investigations of the impact of growth temperature and surface stoichiometry on epilayer deposition are the strength of MBE due to its *in-situ* tools, such as reflection high energy electron diffraction (RHEED). This technique has become extremely valuable for the understanding of growth mechanisms of thin films.

MBE of nitrides can be divided into two approaches, reactive MBE (RMBE) and plasma-assisted MBE (PAMBE), depending on the nitrogen precursor. In RMBE, ammonia is catalytically cracked on the sample surface to deliver active nitrogen, whereas in PAMBE the chemically inert nitrogen molecule is activated by a plasma discharge. Hence, the amount of active nitrogen is coupled to the deposition temperature in RMBE analogously to the case of MOCVD. In contrast, the amount of active nitrogen is independent of deposition temperature in the case of PAMBE, thus allowing rather flexible growth parameters. PAMBE enables low-temperature growth while maintaining an arbitrarily high nitrogen flux as required, e.g., for (In,Ga)N / GaN MQWs.

Aim of this work The above mentioned variety of issues already outlines the objectives of the present work. The overall objective is to investigate the individual steps required for the growth of a blue / UV LED by PAMBE. These steps range from the choice of a suitable substrate, over the synthesis of GaN layers to the deposition of (In,Ga)N / GaN and GaN / (Al,Ga)N MQWs. The quality of the samples is desired to be high and reproducibly so. In addition to these goals related to crystal growth, it is aimed to gain insight into the structure-property relationship of (Al,Ga,In)N.

This thesis is organized as follows. Starting point in Chapter 2 is the understanding of the most important properties of wurtzite nitrides semiconductors: strains and electrical polarization fields of a magnitude not found in other III-V semiconductors. In order to correctly account for these phenomena, an accurate structural characterization (e.g. composition, strain state and structural integrity) of all samples is mandatory. Therefore, in Chapter 3, an efficient model for the dynamical simulation of x-ray diffraction (XRD) profiles is developed. In Chapter 4, the deposition of GaN buffer layers on two substrates, SiC(0001) and γ-LiAlO$_2$(100), is discussed. Compared to the ubiquitous sapphire substrate, these alternative substrates offer—in principle—a variety of promising advantages such as a smaller lattice mismatch to GaN(0001), a high thermal and electrical conductivity [(SiC(0001)] and selectivity in wet-chemical etching [γ-LiAlO$_2$(100)]. At the beginning of this work, both substrates were very rarely used and their preparation and handling was still in its infancy. Development and optimization of substrate preparation is necessary for the reproducible growth of high quality structures.

The most interesting discovery in Chapter 4 is the formation of the non-polar M-plane GaN($1\bar{1}00$) on γ-LiAlO$_2$(100) substrates in contrast to the polar C-plane GaN(0001) orientation obtained on SiC(0001) and Al$_2$O$_3$(0001). Based on this finding, the following investigations were motivated. In Chapter 5, a direct comparison of the properties of C-plane and M-plane GaN epilayers grown under optimized conditions is presented. The results demonstrate the impact of crystal orientation of the GaN films on their morphological, structural, optical and vibrational properties. The by far most interesting difference between these two orientations manifests itself in thin films such as MQWs. The conventional C-plane oriented MQWs exhibit strong electrostatic fields since the polar c-axis of GaN is parallel to the growth direction. These fields lead to a quantum-confined Stark-effect and a substantial reduction in room temperature quantum efficiency. In contrast, M-plane oriented MQWs are free of these fields because the c-axis of GaN is normal to the growth direction. Furthermore, an in-plane anisotropy of the spontaneous emission from M-plane oriented MQWs is found. Chapter 6 covers growth, structural and optical characterization of GaN / (Al,Ga)N MQWs which are ideally suited model systems for studying recombination properties of group-III nitride MQWs due to their high structural perfection. The photoluminescence (PL) results are in excellent agreement with the theoretical predictions.

Chapter 7 treats the synthesis of (In,Ga)N / GaN MQWs which are required for LEDs emitting in the visible spectral range. Growth of (In,Ga)N / GaN MQWs is impeded by In surface segregation as well as spinodal and thermal decomposition. Compared to MOCVD and RMBE, very low growth temperatures can be used in PAMBE to explore deposition of these MQWs far away from thermodynamic equilibrium. Understanding the In surface segregation turns out to be crucial for the realization of high quality (In,Ga)N / GaN MQWs. This segregation manifests itself in RHEED, XRD, secondary-ion-mass-spectrometry (SIMS) and photoluminescence (PL). Finally, the radiative recombination from (In,Ga)N / GaN MQW is studied in Chapter 8. It is shown that both compositional fluctuations and electrostatic fields have to be taken into account for a thorough understanding of the emission from these structures.

A large variety of characterization techniques is employed in this thesis. Experimental details are not presented in a separate Chapter but are given at the relevant part of the text.

2 Strain and electrical polarization fields in wurtzite nitride semiconductors

This Chapter gives an introduction to two of the most important properties of wurtzite nitride semiconductors: strains and polarization fields of a magnitude not found in other III-V semiconductors. First, the consequences of strains on the structural, optical and vibrational properties are presented. Then, the impact of the huge spontaneous and piezoelectric polarization fields on radiative recombination from quantum wells is outlined. Each subject is discussed for an arbitrary crystal orientation as well as for the special cases of C-plane [0001] and M-plane $[1\bar{1}00]$ oriented quantum wells.

2.1 Strain and stress

Group-III nitrides constitute a materials systems with individual lattice mismatches of several percent. A proper treatment of strains and stresses is therefore required in order to correctly describe all phenomena involving strain, e.g., piezoelectric polarization. In this section, the concept of strain and stress is outlined and applied to the two growth directions employed in this thesis, namely, [0001] and $[1\bar{1}00]$.

Unit cell geometry The equilibrium structure of the group-III nitrides is wurtzite. The hexagonal unit cell (Fig. 2.1) is defined by the edge length a of the basal hexagon, the height c of the hexagonal prism, and an internal parameter u defined as the anion-cation bond length along the [0001] axis in units of c. Here, we will restrict ourselves to the elastic properties of this unit cell type. The primitive translational vectors $\mathbf{a}_1$, $\mathbf{a}_2$ and $\mathbf{a}_3$ are readily expressed in terms of the unstrained lattice constants a_r and c_r by

$$\mathbf{a}_1 = a_\mathrm{r}\hat{\mathbf{e}}_x, \quad \mathbf{a}_2 = -\frac{a_\mathrm{r}}{2}\hat{\mathbf{e}}_x + \frac{\sqrt{3}\,a_\mathrm{r}}{2}\hat{\mathbf{e}}_y, \quad \mathbf{a}_3 = c_\mathrm{r}\hat{\mathbf{e}}_z \tag{2.1}$$

with the set of orthonormal basis vectors $(\hat{\mathbf{e}}_x, \hat{\mathbf{e}}_y, \hat{\mathbf{e}}_z)$ in a Cartesian frame of reference. The vector $\mathbf{a}_3$ is parallel to the c-axis and normal to the basal plane which is defined by $\mathbf{a}_1$ and $\mathbf{a}_2$. The angle between the two latter vectors is 120°.

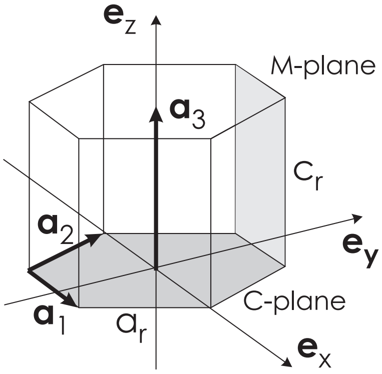

Figure 2.1: Geometry of the unstrained unit cell of nitride semiconductors with the primitive translation vectors $\mathbf{a}_i$ and the set $(\hat{\mathbf{e}}_x, \hat{\mathbf{e}}_y, \hat{\mathbf{e}}_x)$ of Cartesian unit vectors. a_r and c_r denote the unstrained lattice constants. The light and dark shaded areas correspond to the M-plane and the C-plane, respectively.

Strain tensor The strain tensor is used to describe changes of the unit cell geometry due to distortion. In the case of strain, the lengths and/or the directions of the primitive translational vectors are modified. These modified vectors are then expressed using Eq. (2.1) by a new set of basis vectors $\mathbf{e}_x^{'}$, $\mathbf{e}_y^{'}$ and $\mathbf{e}_z^{'}$ in a linear superposition of $\hat{\mathbf{e}}_x$, $\hat{\mathbf{e}}_y$ and $\hat{\mathbf{e}}_z$. For a general strain, we obtain

$$\begin{array}{rcrcrcr} \mathbf{e}_x^{'} & = & (1+\epsilon_{xx})\,\hat{\mathbf{e}}_x & + & \epsilon_{xy}\,\hat{\mathbf{e}}_y & + & \epsilon_{xz}\,\hat{\mathbf{e}}_z \\ \mathbf{e}_y^{'} & = & \epsilon_{yx}\,\hat{\mathbf{e}}_x & + & (1+\epsilon_{yy})\,\hat{\mathbf{e}}_y & + & \epsilon_{yz}\,\hat{\mathbf{e}}_z \\ \mathbf{e}_z^{'} & = & \epsilon_{zx}\,\hat{\mathbf{e}}_x & + & \epsilon_{zy}\,\hat{\mathbf{e}}_y & + & (1+\epsilon_{zz})\,\hat{\mathbf{e}}_z \end{array} \tag{2.2}$$

with the strain tensor elements ϵ_{ij}. The strain tensor may be separated in a symmetric and an asymmetric part. The former contains normal and shear strains while the latter expresses any rotation of the unit cell. [12] For a given sample, one can measure all components of the distortion tensor by a thorough analyis of x-ray diffraction scans. [13] For the samples under investigation in this work, it has been shown by x-ray diffraction that rotations of the unit cells are, if any, negligible. The distortion tensor is thus symmetric and from hereon called strain tensor. This tensor consists of normal strain components ϵ_{xx}, ϵ_{yy} and ϵ_{zz} as well as shear strain components ϵ_{xy}, ϵ_{xz} and ϵ_{yz}.

Stress tensor The stress tensor expresses the pressure which is applied to the crystal. In the present case, the stress tensor is symmetric since the strain tensor is also symmetric. There are normal stresses σ_{xx}, σ_{yy} and σ_{zz} as well as shear stresses σ_{xy}, σ_{xz} and σ_{yz}. The stress and strain tensors are related via the elastic properties of the crystal in the generalization of Hooke's law for systems having more than one degree of freedom. In general, this generalization reads $\sigma_{ij} = C_{ijkl}\epsilon_{kl}$ (Einstein sum convention) with the elements C_{ijkl} of the stress-strain tensor. However, in our case both the stress and the strain tensor are symmetric such that we can simplify this relation. Both the stress and the strain tensors are written as (pseudo-)vectors with 6 elements (Voigt scheme [14]). Consequently, the stress-strain tensor C_{ij} is of (pseudo-)second-rank instead of the original fourth-rank form C_{ijkl}. Furthermore, we take into account the symmetry of the hexagonal unit cell for the symmetry of the stress-strain tensor and arrive at [14]

$$\begin{pmatrix} \sigma_{xx} \\ \sigma_{yy} \\ \sigma_{zz} \\ \sigma_{yz} \\ \sigma_{xz} \\ \sigma_{xy} \end{pmatrix} = \begin{pmatrix} C_{11} & C_{12} & C_{13} & 0 & 0 & 0 \\ C_{12} & C_{11} & C_{13} & 0 & 0 & 0 \\ C_{13} & C_{13} & C_{33} & 0 & 0 & 0 \\ 0 & 0 & 0 & C_{44} & 0 & 0 \\ 0 & 0 & 0 & 0 & C_{44} & 0 \\ 0 & 0 & 0 & 0 & 0 & C_{66} \end{pmatrix} \begin{pmatrix} \epsilon_{xx} \\ \epsilon_{yy} \\ \epsilon_{zz} \\ \epsilon_{yz} \\ \epsilon_{xz} \\ \epsilon_{xy} \end{pmatrix} \tag{2.3}$$

In the following, we will apply this expression to epitaxial layers grown along the [0001] or [1$\bar{1}$00] direction. In both orientations, shear stresses and shear strains are absent since the angles between the primitive translational vectors [Eq. (2.1)] are conserved by stress along one of the unit vectors $\hat{\mathbf{e}}_x$, $\hat{\mathbf{e}}_y$ or $\hat{\mathbf{e}}_z$. A useful boundary condition is the fact that epitaxial films do not experience stress along the growth direction as they are free to expand or contract along this direction. This fact allows us to derive expressions for the strain along the growth direction as a function of the strains within the growth plane.

Strain for growth along [0001] In this orientation, the growth plane corresponds to the xy-plane and deposition takes place along the z direction. The treatment of this orientation is simplified by the fact that the in-plane strain is always isotropic for growth on SiC(0001) as performed in this thesis. Consider an epitaxial layer with unstrained lattice constants a_r and c_r which is grown on a [0001] oriented, lattice mismatched substrate with lattice constants a_s and c_s. Depending on the relaxation of the in-plane lattice mismatch $(a_\mathrm{r} - a_\mathrm{s})/a_\mathrm{s}$, the deposited epilayer has the lattice constants a and c. Hence, the films is under biaxial strain characterized by an isotropic in-plane component $\epsilon_\parallel = (a - a_\mathrm{r})/a_\mathrm{r} = \epsilon_{xx} = \epsilon_{yy}$ within the growth plane and an out-of-plane component $\epsilon_\perp = (c - c_\mathrm{r})/c_\mathrm{r} = \epsilon_{zz}$ along the growth direction (an analogous notation is used for the stress tensor elements).

Eq. (2.3) now reads

$$\begin{pmatrix} \sigma_\parallel \\ \sigma_\perp \end{pmatrix} = \begin{pmatrix} C_{11} + C_{12} & C_{13} \\ 2C_{13} & C_{33} \end{pmatrix} \begin{pmatrix} \varepsilon_\parallel \\ \varepsilon_\perp \end{pmatrix} \tag{2.4}$$

Since the film is free of stress along the growth direction ($\sigma_\perp = 0$) we obtain

$$\frac{\epsilon_\perp}{\epsilon_\parallel} = -2\frac{C_{13}}{C_{33}} \tag{2.5}$$

which describes Poisson's effect. An epilayer under compressive in-plane strain will expand along the growth direction and vice versa. The in-plane stress $\sigma_\parallel$ and in-plane strain $\epsilon_\parallel$ are related by the Young modulus

$$Y = C_{11} + C_{12} - 2C_{13}^2/C_{33} \tag{2.6}$$

via $\sigma_\parallel = Y\epsilon_\parallel$. Note that this equation is equivalent to Hooke's law within the growth plane.

Strain for growth along [1$\bar{1}$00] In this orientation, the growth plane corresponds to the xz-plane, growth takes place along the y direction. The in-plane strain of a lattice mismatched grown epilayer is, in general, not isotropic ($\epsilon_{xx} \neq \epsilon_{zz}$) in contrast to the [0001] growth direction. Nevertheless, one can readily derive a relation for the out-of-plane strain as a function of the two in-plane strains in analogy to the [0001] growth direction. We obtain

$$\epsilon_{yy} = \frac{-C_{12}\epsilon_{xx} - C_{13}\epsilon_{zz}}{C_{11}} \tag{2.7}$$

which is the analogue of Eq. (2.5) of the [0001] orientation.

Choice of materials constants The use of the concept of strain and stress critically relies on the choice of materials parameters. Consequently, great care is used in this work to use the most recent and most reliable data for the unstrained lattice constants and elastic constants (Tab. 3.1). To be as consistent as possible in this thesis, also the optical and vibrational deformation potentials in the next section are taken from the same reference as the elastic constants. [15]

2.2 Optical and vibrational deformation potentials

In this section, we will discuss the consequences of strain on the band gap energy and phonon energies of epitaxial layers. In the course of this thesis, these relations are often used, e.g., in order to support strains determined by x-ray diffraction.

Hydrostatic and uniaxial strain For both the optical and the vibrational properties, it is generally useful to express the strain state of the unit cell in terms of a hydrostatic strain ϵ_h and an uniaxial strain ϵ_u along the c-axis which conserves the unit cell volume. The latter requirement is—to first order—fulfilled if the sum of the normal strains is zero. Hence, we re-write the strain state in terms of ϵ_h and ϵ_u as

$$\begin{pmatrix} \epsilon_{xx} \\ \epsilon_{yy} \\ \epsilon_{zz} \end{pmatrix} = \epsilon_\mathrm{h} \begin{pmatrix} 1 \\ 1 \\ 1 \end{pmatrix} + \epsilon_\mathrm{u} \begin{pmatrix} 1 \\ \alpha \\ -(1+\alpha) \end{pmatrix} \tag{2.8}$$

with the parameter α. This equation can be solved using the boundary conditions given by Eq. (2.5) and (2.7). For the C-plane orientation we get

$$\epsilon_\mathrm{h} = \frac{1}{3}\left(2\epsilon_\parallel + \epsilon_\perp\right), \quad \epsilon_\mathrm{u} = \frac{1}{3}\left(-\epsilon_\parallel + \epsilon_\perp\right) \tag{2.9}$$

while the corresponding expressions for M-plane are

$$\epsilon_\mathrm{h} = \frac{(C_{11} - C_{12})\epsilon_{xx} + (C_{11} - C_{13})\epsilon_{zz}}{3C_{11}}, \quad \epsilon_\mathrm{u} = \frac{(C_{11} + 2C_{12})\epsilon_{xx} + (C_{13} - C_{11})\epsilon_{zz}}{3C_{11}} \tag{2.10}$$

Optical properties A compression of the unit cell will, at least in case of all III-V semiconductors, result in a blue-shift of intrinsic optical transitions whereas an expansion leads to a red-shift in emission and absorption. In the quasicubic approximation, [15] the transition energy associated with the free A exciton ($\Gamma_{1c} - \Gamma_{6v}$) of wurtzite nitrides is shifted according to

$$\Delta E_\mathrm{A} = 3a_g\epsilon_\mathrm{h} - \frac{3}{2}\frac{d_5}{\sqrt{6}}\epsilon_\mathrm{u} \tag{2.11}$$

with the deformation potentials a_g and d_5. This expression is valid for small strains and is then exact for [0001] oriented samples but only an approximation in the case of $[1\bar{1}00]$ oriented films. The numerical values of the deformation potentials used in this thesis are listed in Tab. 2.1.

Vibrational properties The E_2 phonon mode is generally used to examine the strain state of GaN by Raman measurements. A linear superposition of hydrostatic and uniaxial components is also assumed to be valid for the frequency shift $\Delta\omega_{E_2}$ of the E_2 phonon. Hence, we find

$$\Delta\omega_{E_2} = 3\omega\gamma\epsilon_h + \beta\epsilon_u \tag{2.12}$$

Table 2.1: Optical deformation potentials (eV) in the quasi-cubic approximation for wurtzite nitride semiconductors. [15]

Material	a_g	d_5
GaN	-6.9	-5.3
AlN	-9.0	-7.5
InN	-2.8	- 3.8

where ω is the E_2 phonon wave number and β a constant. γ=$\partial \ln \omega / \partial \ln V$ is the Grüneisen parameter which relates relative changes in phonon frequencies to relative changes of the unit cell volume.

Once again, the value of $\Delta\omega_{E_2}$ substantially depends on the correct choice of materials constants. We use the same *ab-initio* calculations [15] as before to extract the Grüneisen parameter of γ=1.8 for GaN. The E_2 mode of unstrained GaN has a frequency of ω=566.2 cm^{-1} [16]. The constant β=5692 cm^{-1} is deduced by comparison Eq. (2.12) to recent experimental results. [16]

2.3 Electrical polarization

A sizable red-shift of the ground-level transitions of wurtzite nitride semiconductor quantum wells has been observed by various groups [17–20] for increasing well width. This phenomenon is sometimes accompanied by the concomitant reduction of the oscillator strength and by the increase of the decay time of the transition. All together, these effects point towards the existence of strong built-in electrostatic fields in wurtzite nitride semiconductors, which causes a substantial quantum-confined Stark effect (QCSE). The underlying phenomenon is the presence of huge electrical polarization fields in wurtzite nitride semiconductors: The spontaneous polarizations are of the same order of magnitude as those of ferroelectrics. The magnitude of the piezoelectric constants exceeds that of other III-V semiconductors by more than one order of magnitude.

GaN unit cell symmetries The presence of electrical polarization is strongly connected to the unit cell symmetry of a crystal. Nitride semiconductors exist in both the zincblende and wurtzite modifications[*] which are closely related to each other. Ball-and-stick models of these two structures are given in Fig. 2.2. In both cases, each group-III atom is tetrahedrally coordinated to four nitrogen atoms. The main difference between these two structures is the stacking sequence of close packed diatomic planes. These stacking sequences are ABABAB along the wurtzite $\{0001\}$ directions and ABCABC along the zincblende $\{111\}$ directions. This difference in stacking sequence results in distinct space group symmetries: P6$_3$mc for wurtzite and F$\bar{4}$3m for zincblende.

In the absence of external electric fields, the total macroscopic polarization $\mathbf{P}$ of a solid is the sum of the spontaneous polarization of the equilibrium structure and of the strain-induced, piezoelectric polarization.

Spontaneous[†] polarization The zincblende compound semiconductors such as, e.g., GaAs or GaN have four symmetry equivalent polar $\langle 111 \rangle$ axes whose contributions cancel each other in equilibrium. Hence, these materials are free of electrical polarization at equilibrium. In contrast, the wurtzite phase has a singular polar axis, namely, the [0001] axis. Thus, the wurtzite phase carries spontaneous electrical polarization along [0001] even at equilibrium.

Piezoelectric polarization In practice, semiconductor layers are often grown under

---

[*] There also exists the high-pressure rocksalt modification.

[†] Sometimes the term 'pyroelectric polarization' is used as the magnitude of the spontaneous polarization changes with temperature due to thermal expansion of the crystal.

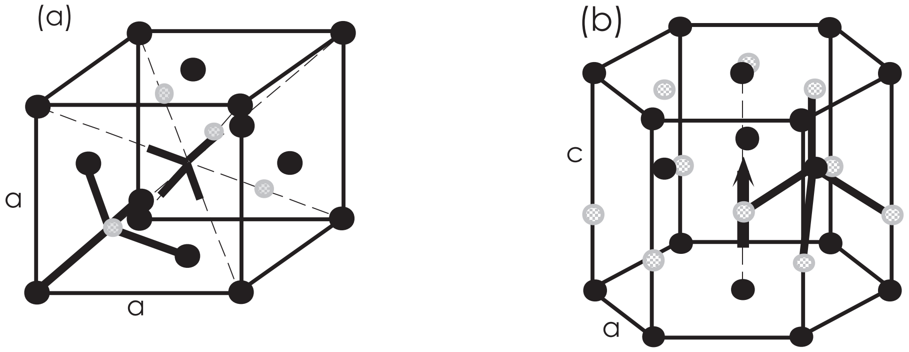

Figure 2.2: Ball-and-stick models of crystals with zincblende (a) and wurtzite (b) structure. Note the tetrahedral coordination in both cases.

strain due to the lattice mismatch to the underlying layer. Such deformations of the unit cell can lead to additional piezoelectric polarization. The presence of this kind of polarization is again closely related to the unit cell symmetry, namely, the lack of inversion symmetry. The contributions of the four polar axes of zincblende structures cancel each other for growth along a $\langle 001 \rangle$ direction. However, growth along one of the polar axes lifts the symmetry and the crystal exhibits piezoelectric polarization. In contrast, the wurtzite structure with its unique polar [0001] axis always carry piezoelectric polarization for any growth direction.

In the following, we discuss nitride semiconductors in this wurtzite structure. The total electric polarization $\mathbf{P}$ is the sum of spontaneous polarization $\mathbf{P}_{\mathrm{SP}}$ and piezoelectric polarization $\mathbf{P}_{\mathrm{PZ}}$.

In general, the unit cell can be under arbitrary strain. The piezoelectric polarization is calculated using the piezoelectric tensor [21] of the space group P6$_3$mc by

$$\mathbf{P}_{\mathrm{PZ}} = \begin{pmatrix} 0 & 0 & 0 & 0 & e_{15} & 0 \\ 0 & 0 & 0 & e_{15} & 0 & 0 \\ e_{31} & e_{31} & e_{33} & 0 & 0 & 0 \end{pmatrix} \begin{pmatrix} \epsilon_{xx} \\ \epsilon_{yy} \\ \epsilon_{zz} \\ \epsilon_{yz} \\ \epsilon_{xz} \\ \epsilon_{xy} \end{pmatrix} = \begin{pmatrix} e_{15}\epsilon_{xz} \\ e_{15}\epsilon_{yz} \\ e_{31}(\epsilon_{xx} + \epsilon_{yy}) + e_{33}\epsilon_{zz} \end{pmatrix} \tag{2.13}$$

with the elements e_{ij} of the piezoelectric tensor, the uniaxial strain components ϵ_{xx}, ϵ_{yy}, ϵ_{zz} and the shear strains ϵ_{xy}, ϵ_{xz}, ϵ_{yz}.

For growth along [0001], it is expected that shear strain is absent. As already mentioned in section 2.1, this assumption has been verified by x-ray diffraction for the samples under investigation. Additionally, the in-plane strain is isotropic ($\epsilon_{xx} = \epsilon_{yy}$). With the usual conventions $\epsilon_{\|} = \epsilon_{xx}$ and $\epsilon_{\perp} = \epsilon_{zz}$ we arrive at

$$P_{\mathrm{PZ},[0001]} = e_{33}\epsilon_{\perp} + 2e_{31}\epsilon_{\|} \tag{2.14}$$

with the piezoelectric constants e_{33} and e_{31} and the elastic constants C_{13} and C_{33}. Hence, the piezoelectric polarization is along [0001].

For growth along [1$\bar{1}$00], we can also simplify Eq. (2.13). Again, no shear strain is present in the growth plane, hence, both ϵ_{xz} and ϵ_{yz} vanish. The total piezoelectric

Table 2.2: Spontaneous polarization and piezoelectric constants (both in units of C m^{-2}) of wurtzite group-III nitride semiconductors. [25]

	P_{SP}	e_{33}	e_{31}
AlN	-0.081	1.46	-0.60
GaN	-0.029	0.73	-0.49
InN	-0.032	0.97	-0.57

polarization is parallel to [0001] and has the magnitude

$$P_{\mathrm{PZ},[1\bar{1}00]} = e_{31}(\epsilon_{xx} + \epsilon_{yy}) + e_{33}\epsilon_{zz} \tag{2.15}$$

Polarization constants Materials constants of group-III nitrides are generally determined in *ab-initio* density-functional theory (DFT) calculations in the framework of the local-density approximation (LDA). The data obtained have been shown to be in excellent agreement with experimental values (see, e.g., [15]). In the case of spontaneous and piezoelectric polarization constants, it is important to note that these materials constants critically rely on structural data such as, e.g., the lattice constant ratio c/a and the anion-cation bond length uc along the [0001] axis. Ideally, the wurtzite structure has c/a=5/3 and u=3/8 but the actual values [22, 23] found for GaN, AlN and InN significantly deviate from these ideal values. Very recently, is it was demonstrated by Bechstedt *et al.* [24] that even small uncertainties in the structural parameters substantially modify the calculated polarization constants. This statement is particularly important for InN as the lattice constants of this material are subject to a large uncertainty due to lack of reliable experimental data.

In this thesis, the polarization constants determined by Bernadini *et al.* [25] are used (Tab. 2.2). These parameters are obtained by DFT-LDA using the Berry phase approach to the polarization of solids. For several years, these data constituted the only available values apart from the very recent work of Bechstedt *et al.* [24] who obtained significantly different absolute parameters in their approach. However, the strength of electrostatic fields in thin layers only depends on the differences in electrical polarization between well and barrier material as shown below. In fact, for the structurally well-known GaN/(Al,Ga)N system the two sets of data result in electrostatic fields of very comparable magnitude. In contrast, the predicted electrostatic fields in the (In,Ga)N/GaN system scatter, most probably due to the lack of reliable structural data. From the data of Bernadini *et al.* [25] (Tab. 2.2) one can calculate the total polarization **P** of (Al,Ga,In)N layers. After having clarified the origin (unit cell symmetry), the direction (parallel to [0001] for C-plane and M-plane MQWs) and the magnitude of electrical polarization [Eq. (2.14), (2.15)] we now turn to the consequences of these fields. In the following, we will show that polarization changes normal to interfaces induce internal electrostatic fields which can be as strong as several MV/cm.

2.4 Internal electrostatic fields due to electrical polarization

In this section, the consequences of electrical polarization on [0001] and [1$\bar{1}$00] oriented quantum wells are discussed. It will be shown that the former exhibit strong internal

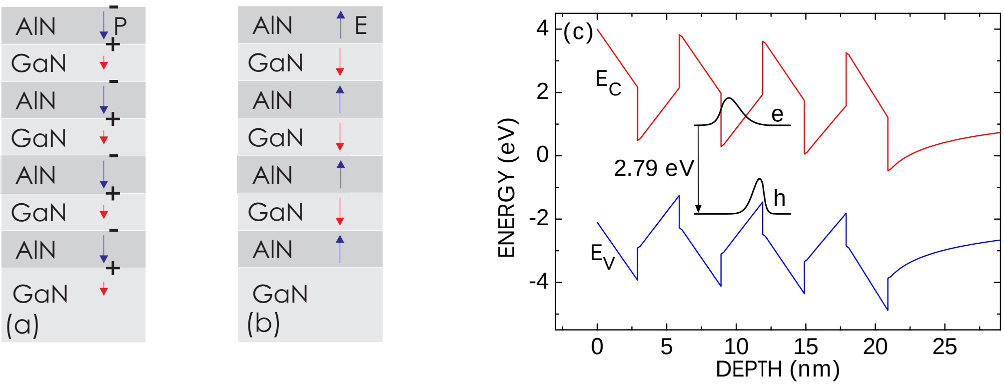

Figure 2.3: Effect of electrical polarization on a (3 nm GaN)/(3 nm AlN) MQW with 3 periods grown coherently on a GaN(0001) buffer. The changes in total polarization of the individual layers lead to interface charges (a) which result in strong internal electrostatic fields (b). Note the red-shift of the transition energy with respect to flat-bands conditions (Quantum-confined Stark-effect) and the spatial separation of electron (e) and hole (h) wavefunction (c).

electrostatic fields normal to the wells whereas the latter are free of these fields.

[0001] oriented quantum wells: Electrostatic fields In this orientation the growth direction is parallel to the total polarization vector. Any discontinuity ΔP in the polarization component results in a sheet charge density ΔP at the corresponding interface or surface. [26] For example, consider a GaN / AlN superlattice with thicknesses t_{GaN} and t_{AlN} grown coherently on a GaN(0001) buffer layer (Fig. 2.3). The total polarization of unstrained GaN and coherently strained AlN differs, resulting in charges with alternating sign which are built up at the interfaces and the surface [Fig. 2.3(a)]. These interface charges result in internal electrostatic fields E_{GaN} and E_{AlN} within the layers [Fig. 2.3(b)]. One may calculate these fields in an analytic expression. [27] Although this approach is widely used, it is strictly valid only in certain circumstances since it neglects free carrier screening and the finite number of periods. Screening, for example, limits the total potential drop across the structure to the band gap energy. Hence, a self-consistent approach is required. In this work, a freeware program[‡] is used to simultaneously solve the Poisson and Schrödinger equations in the effective mass approximation. Polarization charges are introduced by 1 Å thin doping spikes with volume doping levels of $n_{3\mathrm{D}} = \Delta P/(e\ \text{Å})$ with the elementary charge e. The n-type background doping level is set to 10^{17} cm^{-3}. The results of these calculations are crosschecked by other methods. Excellent agreement is found with band profiles obtained by a well-established device simulations program ('Tosca') and various examples reported in the literature. The obtained wavefunction are also verified by a independent numerical solution of the Schrödinger equation for each of the calculated band profiles.

In Fig. 2.3(c) the result of such a calculation is shown. The electric field in the wells is as large as 7 MV / cm. The different quantum wells have different fields due to finite number of periods. This phenomenon results in different transition energies. The strong internal electrostatic fields within the layers lead to a localization of the electron and hole wavefunctions at either side of the quantum well [Fig. 2.3(c)]. This separation of carriers has two important consequences. First, the interband transition energy at 300 K

[‡] G. Snider, 1D Poisson / Schrödinger: A band diagram calculator, `http://www.nd.edu/~gsnider/`

is red-shifted from 3.58 eV (flat-band conditions including quantum confinement) to 2.79 eV [quantum-confined Stark-effect (QCSE)]. Second, the spatial separation leads to a decrease in wavefunction overlap and thus to a reduction in transition probability. Consequently, the radiative decay time is prolonged due to the reduced oscillator strength for recombination. This reduced transition probability can be measured via prolonged radiative decay times in photoluminescence. The QCSE and the spatial separation of wavefunctions are more pronounced as the well thickness increases.

[1$\bar{1}$00] oriented quantum wells: Flat-band conditions For growth on the non–polar [28] M-plane the growth direction is normal to the direction of the total polarization. Thus, there is no change in the polarization component along the growth direction. Hence, no interface charges are built up. Moreover, vertical electrostatic fields induced by electrical polarization *do not* exist in M-plane oriented MQWs. Flat-band conditions are achieved in this crystal orientation.

This finding has two important consequences which are in contrast to the C-plane wells. First, the emission energy from quantum wells is solely determined by quantum confinement. Second, the electron and hole wavefunctions are not spatially separated, hence, their overlap is close to unity.

From the discussion in this Chapter, it is obvious that a reliable and accurate determination of composition and strain state of samples under study is vital for the correct calculation of polarization fields in wurtzite nitride MQWs. Therefore, the next Chapter treats the resolute determination of these structural parameters by x-ray diffraction.

3 Dynamical x-ray diffraction for accurate determination of strain state and composition of highly-mismatched group-III nitrides

This Chapter deals with x-ray diffraction for the accurate determination of structural parameters of the nitride semiconductor films grown in this work. First, the usual kinematical analysis of x-ray diffraction profiles is discussed in terms of its potential and its limits. Second, the generally employed scans in reciprocal space and real space are discussed. Third, a model for the dynamical simulation of x-ray diffraction profiles is formulated and presented for wurtzite and zincblende crystals. This model is in excellent agreement with existing dynamical models but much easier to implement and computationally very efficient. Fourth, the validity of the model is demonstrated by various experimental examples.

3.1 Accurate kinematical analysis of x-ray diffraction profiles

Need for a reliable determination of structural parameters The value of an exact structural characterization of epitaxially grown films cannot, in general, be exaggerated. For example, the electrostatic fields introduced in the last Chapter are extremely sensitive to the interplay of composition, strain state and layer thickness. [19,20,29,30] Another example is the unusually large band gap bowing calculated and observed, particularly for (In,Ga)N. [31–34] However, the available experimental data on both electrostatic fields and band gap bowing are neither in agreement with each other nor with theory. This fact is at least partly the consequence of an insufficient or incorrect structural characterization of the samples under investigation.

Generally, a solution to the following problem is required. Consider an epilayer which is grown on a substrate with (known) interplanar spacings c_s and a_s perpendicular and parallel to the crystal surface, respectively. Then, one faces the task to determine as accurately as possible the composition and the strain state of the epilayer.

A very sensitive structural characterization method is x-ray diffraction. This technique is widely employed for the structural investigation of epitaxial layers and multilayer systems. In an x-ray diffraction experiment, a monochromatic and collimated x-ray beam of wavelength λ is focussed on the sample surface under an angle ω with respect to the sample surface. The diffracted intensity is detected under an angle of 2θ with respect to the incident beam [see also Fig. 3.2(a)].

A rather common approach to perform the above mentioned task is the kinematical analysis of x-ray diffraction profiles. In a kinematical analysis, the peak positions of the x-ray reflectivity as a function of ω are used for determining the lattice constants c_e and a_e of the film.

Failure of conventional first-order kinematical analysis Very commonly, a linear relation between lattice mismatch and angular separation is employed for evaluation of x-ray diffraction profiles. In this widely used and closed analytical form [35], the lattice mismatches $\Delta a/a_\mathrm{s} = (a_\mathrm{e} - a_\mathrm{s})/a_\mathrm{s}$ [$\Delta c/c_\mathrm{s} = (c_\mathrm{e} - c_\mathrm{s})/c_\mathrm{s}$] parallel (normal) to the sample surface are linear combinations of the measured angular separations $\Delta\omega^{\mathrm{I,II}}$ of substrate and epilayer peaks for two different reflections I and II:

$$\begin{pmatrix} \Delta c/c_\mathrm{s} \\ \Delta a/a_\mathrm{s} \end{pmatrix} = \begin{pmatrix} A^\mathrm{I} & B^\mathrm{I} \\ A^\mathrm{II} & B^\mathrm{II} \end{pmatrix}^{-1} \begin{pmatrix} \Delta\omega^\mathrm{I} \\ \Delta\omega^\mathrm{II} \end{pmatrix} \tag{3.1}$$

with

$$A^\mathrm{I,II} = \cos\phi_\mathrm{s}^\mathrm{I,II}\left(\cos\phi_\mathrm{s}^\mathrm{I,II}\tan\theta_\mathrm{s}^\mathrm{I,II} + \sin\phi_\mathrm{s}^\mathrm{I,II}\right) \tag{3.2}$$

$$A^\mathrm{I,II} = \sin\phi_\mathrm{s}^\mathrm{I,II}\left(\sin\phi_\mathrm{s}^\mathrm{I,II}\tan\theta_\mathrm{s}^\mathrm{I,II} - \cos\phi_\mathrm{s}^\mathrm{I,II}\right) \tag{3.3}$$

The angles $\theta_\mathrm{s}^\mathrm{I,II}$ and $\phi_\mathrm{s}^\mathrm{I,II}$ denote the Bragg angle and angle between crystal surface and lattice plane of the substrate for reflection I,II, respectively.

These expressions are almost exclusively used for the investigations of systems with low mismatch such as, e.g., arsenides. [36] However, Eq. (3.1) are first-order approximations in $\Delta\omega$ and only valid for values of $\Delta\omega$ below 0.2°. In the case of the highly mismatched group-III nitrides, the error in Δc and Δa of this approximation can be as high as 50% preventing a reliable structural investigation. Therefore, great care is required for a correct evaluation of x-ray diffraction profiles.

Parameters for the exact kinematical analysis Several researchers have recognized the restriction of Eq. (3.1) to small values of $\Delta\omega$ and developed second-order approximations. [37,38] Here, we will use an alternative approach which yields exact expressions for the lattice mismatch. This approach is based on the use of absolute angles instead of angular separations.

Consider a set of parallel lattice planes which are defined by a spacing d and a vector $\mathbf{h}$ normal to the planes. Both d and $\mathbf{h}$ are obtained from the lattice constants and the Miller indices. The Bragg angles θ_n of this set of planes is related then to d via the Bragg condition

$$n\lambda = 2d\sin\theta_n \quad n = 1, 2, 3, \ldots \tag{3.4}$$

with the x-ray wavelength λ. The lattice plane inclination ϕ denotes the angle between the unit surface normal vector $\hat{\mathbf{n}}$ of the crystal and the lattice plane normal vector $\mathbf{h}$, namely

$$\phi = \arccos\frac{\mathbf{h}\cdot\hat{\mathbf{n}}}{h} \tag{3.5}$$

where h denotes the length of $\mathbf{h}$.

Diffraction geometries From these expressions, one readily calculates the kinematical angles of incidence at which a specific crystal plane diffracts. Our model as presented in this Chapter supposes the usually employed coplanar geometry where both the incident and the diffracted beams are in the plane defined by linear combinations of $\mathbf{h}$ and $\hat{\mathbf{n}}$ (Fig. 3.1). In the case of symmetric reflections, ϕ is equal to zero and the angle of incidence ω equals the Bragg angle θ of the lattice plane. However, for asymmetric reflections ϕ is non-zero, hence, the angle of incidence ω is either $\theta + \phi$ (steep incidence) or $\theta - \phi$ (glancing incidence). Reflections are only accessible if both $\theta \pm \phi$ are between 0° and 180°.

Exact kinematical analysis The usually employed expressions [Eq. (3.1)] to obtain lattice mismatches from peak separations require only two scans but utterly fail in the

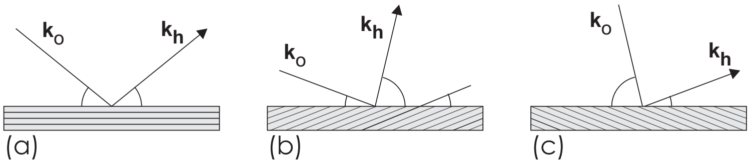

Figure 3.1: Different coplanar geometries used in x-ray diffraction experiments: (a) symmetric, (b) asymmetric with glancing incidence and (c) asymmetric with steep incidence. θ and ϕ denote Bragg angles and lattice inclination angles, respectively. $\mathbf{k_o}$ ($\mathbf{k_h}$) corresponds to the incident (diffracted) beam.

case of large mismatches (a few percent) as present in nitride semiconductors. A direct and exact kinematical analysis of x-ray diffraction profiles of highly mismatched systems is still possible but requires at least three scans (one symmetric and two asymmetric ones). This procedure will, if correctly done, return correct values [39, 40] for the epilayer composition and strain state. Generally, an exact kinematical analysis is composed of two steps.

First, the lattice constants of the individual layers are calculated from the measured absolute reflections angles of substrate and corresponding layer. The lattice constant c parallel to the growth direction is directly obtained from the symmetric scan via the Bragg condition [Eq. (3.4)]. In contrast, the asymmetric diffraction angle depends on both c and the lattice constant a within the growth plane. The ratio c/a can be determined via ϕ which is measured by the combination of two asymmetric scans of the same lattice plane, the first with glancing incidence and the second with steep incidence. [41]

Second, the obtained set (a,c) is converted into a set of strain state and composition via boundary conditions imposed by the elastic constants which relate elastic strains parallel and normal to the sample surface.

3.2 From the kinematical to the dynamical analysis

Existing dynamical simulations A kinematical analysis does not give any clue as to the perfection of the structure, as intensities and linewidths cannot be calculated. An indirect analysis via simulation of profiles with the strain components as input parameters would thus be preferable. In particular, a dynamical analysis enables one to correctly account for extinction and thus reflection intensities. Existing dynamical diffraction models for multilayer structures, however, break down for strains on the order of one percent, [12, 42] with the noticeable exceptions of the models of Zaus [42] and of De Caro *et al.* [12] The former model is a significant improvement over those commonly used, but is conceptually questionable. Attempts to describe extremely asymmetric reflections close to total reflection by dynamical corrections as those forwarded by Zaus are necessarily futile. The Takagi-Taupin formulation is based on the quadratic dispersion relation and therefore not applicable to this situation. The latter model of De Caro *et al.* is generally valid but difficult to implement, poses significant numerical problems and is computationally very intensive. Furthermore, this model takes into account only one Bragg reflection. For example, a simulation around the symmetric GaN(0002) reflection ignores contributions of other reflections such as, e.g., GaN(0004).

Validity of present model Here, we present a simple and computationally fast, yet accurate model for the dynamical x-ray diffraction analysis of highly mismatched materials systems in the coplanar geometry. We focus on zincblende and hexagonal systems, such as GaN-based heterostructures. Our model features exact calculations of the parameters critical for dynamical x-ray simulations (incidence parameter α^*, Bragg angle θ and lattice plane inclination ϕ). The model presented here thus surpasses any of its predecessors which utilized second-order approximations for these values. [37, 38]

Our approach is based on the standard Takagi-Taupin equations which take into account the transmitted and the diffracted beams. Therefore, our model is *not* valid for diffraction close to total internal or external reflection, [12, 43] or for situations involving more than one Bragg reflection. [44] However, both restrictions are only of interest for rather exceptional experiments. In practice (see section 3.5), the contributions of total reflections and / or other Bragg reflections cannot be detected as they are well below the background level imposed by the experimental set-up.

The model presented in this thesis has been tested extensively and it was found that the results are virtually identical to those of De Caro *et al.* [12] except for cases close to total reflection. The validity of our model is demonstrated by experimental examples of simple GaAs / AlAs and GaN / AlN / SiC heterostructures. In the next Chapters of this thesis, this model is applied to various samples such as GaN / (Al,Ga)N and (In,Ga)N / GaN heterostructures. Therefore, the results of this Chapter guarantee a reliable structural characterization in the following chapters of this thesis.

3.3 Scans in reciprocal and real space

There exist several different types of scans in the coplanar geometry. Unfortunately, these various types of measurements are often confused and wrong or misleading statements are given. Therefore, different types of scans which are carried out in this thesis are discussed in this section.

The reciprocal space for heteroepitaxially grown samples Consider a heteroepitaxially grown zincblende epilayer on a zincblende substrate such as, e.g., (In,Ga)As grown on GaAs(001). The origin (000), the symmetric (004) reflection and the asymmetric (224) reflection are part of the reciprocal space of this system [Fig. 3.2(a)].

For both reflections, the substrate spots have a circular shape and minimum broadening as the substrate corresponds to an (ideally) perfect crystal. The coordinates of these reflections are well-known from the lattice constants of the bulk substrate material. These substrate coordinates serve as reference for the subsequent determination of the epilayer coordinates in reciprocal space. The epilayer spots are elliptically shaped due to the orientational spread (mosaicity) of the crystal caused by imperfections such as dislocations. It is important to note in this context that the symmetric orientational spread only contains the tilt components of a Burgers vector. In contrast, the asymmetric orientational spread depends on both the tilt and the twist component of a Burgers vector. In C-plane oriented wurtzite nitrides, dislocation lines are parallel to the c-axis such that the tilt solely depends on the density of screw dislocations whereas the twist

---

[*] This parameters describes the angular separation of the actual angle of incidence with respect to the kinematical Bragg angle.

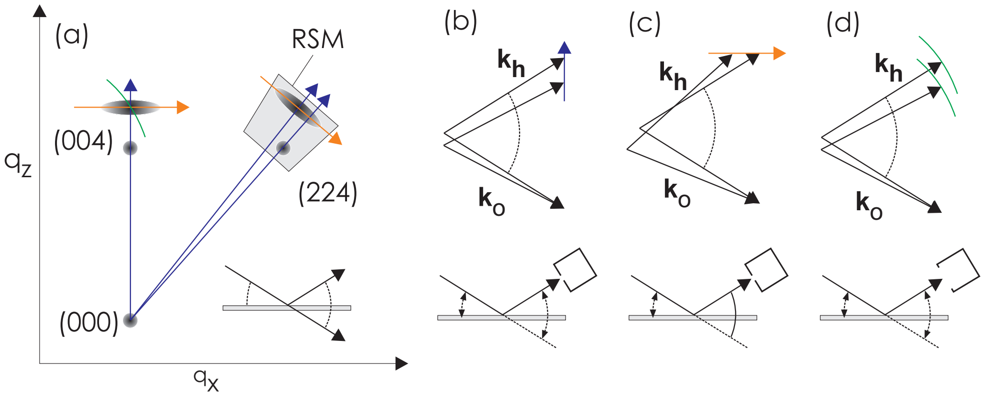

Figure 3.2: (a) Schematic of x-ray diffraction geometries in reciprocal space as well as reciprocal and real space for (b) θ-2θ, (c) ω and (d) x-ray rocking curve scans. RSM in (a) denotes a reciprocal space map. q_x and q_z denote the directions in reciprocal space parallel and normal to the surface, respectively. Note in (a) that for each reflection both the spot separation and size are grossly exaggerated for clarity.

depends on the density of edge dislocations. [45]

All symmetric diffraction spots lie along the [001] axis, hence, the spot position is a direct measure of the lattice constant c parallel to the growth direction. In contrast, the asymmetric diffraction spot positions also depend on the lattice constant a within the growth plane. Both a_e and c_e of the epilayer are functions of the strain state and composition. Therefore, the exact polar angle of the epilayer spot—in contrast to the substrate spot—is *a priori* not known. However, for a detailed structural investigation, information on both a and c is required. In the following, it will be outlined how the coordinates of the epilayer spot are accurately determined.

θ-2θ and ω scans First, we discuss the two different scan types carried out with an analyzer crystal in front of the detector. The analyzer crystal minimizes the angular acceptance of the detector to a few arcsec [see also Fig. 3.2(b)], and thus a high spatial resolution in reciprocal space is achieved. In the θ-2θ scan [Fig. 3.2(b)], the detector angle θ is changed with twice the speed of the sample angle ω. A θ-2θ scan corresponds to a radial scan in reciprocal space. In contrast, the detector angle θ is fixed in the ω scan [Fig. 3.2(c)] but the sample angle ω is changed. Hence, the reflectivity as a function of polar angle at fixed distance to the origin in reciprocal space is measured. Both scan types are indicated in Fig. 3.2 for the symmetric and the asymmetric epilayer diffraction spots.

The symmetric θ-2θ scan always crosses both the epilayer and the substrate diffraction spots resulting in an accurately determined lattice constant c_e of the epilayer. The peaks are not broadened by the mosaicity of the crystal. Information on this symmetric orientational spread (tilt) is gained from symmetric ω scans.

A single asymmetric θ-2θ scan is pointless. A radial scan can only cross either the substrate or the epilayer spot which have different polar angles. If the q_x coordinate of the spots of interest is identical and known, e.g., for coherently grown structures, then a vertical scan in reciprocal space crossing asymmetric spots is possible via ω-2θ scans. In this case, the ratio $\Delta\omega/\Delta\theta$ of sample and detector amounts to $1/(1 + \|b\|)$ where b is called the asymmetry factor (see next Section). In most practical circumstances, however, the q_x coordinates of the epilayer spots are unknown. These positions can be gained from a reciprocal space map (RSM). Such a map [Fig. 3.2(a)] requires a series of radial θ-2θ scans with continuously changed polar angle and is therefore very time consuming (several days). The asymmetric orientational spread (tilt and twist) can—in principle—be measured in an asymmetric ω scan.

X-ray rocking curves An attractive alternative is the x-ray rocking curve (XRC) which represents a combination of both the θ-2θ and the ω scan. In the XRC [Fig. 3.2(d)], the angular acceptance of the detector angle is maximized (usually around 10°). Therefore, the measured reflectivity does not correspond to a single point in reciprocal space but the integrated intensity along a circular segment [Fig. 3.2(a)] of the Ewald sphere. The XRC is performed such that the circular segment crosses all relevant diffraction spots with continuously changing incidence angle ω. Due to the large size of this circular segment it usually does not matter if the detector is moved analogously to the θ-2θ scan [Fig. 3.2(d)] or fixed.

The symmetric XRC exhibits the same peak positions as the symmetric θ-2θ scan but the peaks are broadened by the orientational spread (tilt) allowing for a quick check of the structural perfection. However, if this spread is too large then the individual peaks cannot be clearly resolved and one has to resort to high-resolution θ-2θ scans.

The full advantage of the XRC is evidenced for asymmetric scans. The series of circular segments covers both the substrate and the epilayer peaks in a single scan such that both the peak positions and also the asymmetric orientational spread (tilt and twist) are determined. Hence, only a single scan with substantially reduced measurement time is required in contrast to the series of scans for a reciprocal space map. In this thesis, all asymmetric scans are therefore performed as XRCs.

3.4 Formulation of the model

The following model accurately describes dynamical x-ray rocking curves of perfect crystals with atomically abrupt interfaces. Particularly, this model is ideally suited for the simulation of symmetric θ-2θ scans which are not sensitive to broadening due to mosaicity.

Let us first pursue the parameters of crucial importance, namely, the incidence parameter α and the direction cosines γ_i. These parameters are given by [46]

$$\alpha = \frac{(\mathbf{k_o} + \mathbf{h})^2 - k_o^2}{2k_o^2} \quad \text{and} \quad \gamma_{o,h} = \frac{\mathbf{k_{o,h}} \cdot \hat{\mathbf{n}}}{k}, \tag{3.6}$$

where $\mathbf{k_{o,h}}$ are the wavevectors of the incident and diffracted beams, $\mathbf{h}$ is the reciprocal lattice vector of the specific reflection, and $\hat{\mathbf{n}}$ is the unit surface vector.

Most x-ray simulation programs (even some of those commercially available) [44] rely on a first-order approximation [analogous to Eq. (3.1)] α, [42,43,47,48] namely

$$\alpha = -\left(\Delta\omega + \Delta\theta + \Delta\phi\right) \sin 2\theta_s, \tag{3.7}$$

where $\Delta\omega$ is the scan angle, and

$$\Delta\theta = \left(\frac{\Delta a}{a_\mathrm{s}} \sin\phi_\mathrm{s}^2 + \frac{\Delta c}{c_\mathrm{s}} \cos\phi_\mathrm{s}^2\right) \tan\theta_\mathrm{s}, \tag{3.8}$$

$$\Delta\phi = \left(\frac{\Delta c}{c_\mathrm{s}} - \frac{\Delta a}{a_\mathrm{s}}\right) \sin\phi_\mathrm{s} \cos\phi_\mathrm{s}, \tag{3.9}$$

are first-order approximations for the changes $\Delta\theta$ of Bragg angle (θ_s) and $\Delta\phi$ of the lattice plane inclination (ϕ_s) where the subscript s denotes the substrate. In the case of a symmetric reflection, $\phi_\mathrm{s} = 0$, leading to the well-known (and incorrect) linear relation $\Delta c/c_\mathrm{s}{=}{-}\Delta\omega \cot\theta_\mathrm{s}$.[†] The correct expression which follows directly from Bragg's law is $\Delta c/c_\mathrm{s} = (\sin\theta_\mathrm{e} - \sin\theta_\mathrm{s})/\sin\theta_\mathrm{s}$ with the epilayer peak positions θ_e. Note that the commonly used linear expressions [36] relating the angular separation $\Delta\theta$ between the m^{th} and $m \pm 1^{st}$ order of superlattice reflections (or interference fringes) with the period of the superlattice (the thickness of the cap layer) are first-order approximations as well.

In the following, we will use the exact expression for the incidence parameters and the direction cosines. In contrast to the commonly used trigonometric approach, [37,38,42] we choose a vectorial formalism since it introduces the crystal symmetry in a natural and flexible way, and makes generalization to arbitrary lattice distortions (leading, in the worst case, to unit cells with triclinic symmetry) straightforward.

Structural definitions The reciprocal lattice vectors are given by

$$\mathbf{h} = \mathrm{h}\mathbf{b}_1 + \mathrm{k}\mathbf{b}_2 + \mathrm{l}\mathbf{b}_3 \tag{3.10}$$

where (hkl) are the Miller indices of the specific reflection, and the reciprocal basis is set in the standard way as

$$\mathbf{b}_u = \frac{\mathbf{a}_v \times \mathbf{a}_w}{\mathbf{a}_u \cdot \mathbf{a}_v \times \mathbf{a}_w}. \tag{3.11}$$

Now, we define the real space lattice vectors of zincblende and hexagonal unit cells under possible biaxial strain within the growth plane. The zincblende structure is described by the Bravais lattice

$$\mathbf{a}_1 = \begin{pmatrix} a \\ 0 \\ 0 \end{pmatrix}, \quad \mathbf{a}_2 = \begin{pmatrix} 0 \\ a \\ 0 \end{pmatrix}, \quad \mathbf{a}_3 = \begin{pmatrix} 0 \\ 0 \\ c \end{pmatrix} \tag{3.12}$$

while the hexagonal symmetry of the wurtzite structure is accounted for by the following Bravais lattice:

$$\mathbf{a}_1 = \begin{pmatrix} a \\ 0 \\ 0 \end{pmatrix}, \quad \mathbf{a}_2 = \frac{1}{2}\begin{pmatrix} -a \\ \sqrt{3}a \\ 0 \end{pmatrix}, \quad \mathbf{a}_3 = \begin{pmatrix} 0 \\ 0 \\ c \end{pmatrix}, \tag{3.13}$$

For biaxial strain, the lattice constants a and c of a layer with unstrained lattice constants a_r and c_r are given by

$$a = a_\mathrm{r}\left(1 + \epsilon_{\|}\right), \quad c = c_\mathrm{r}\left(1 + \epsilon_{\perp}\right), \tag{3.14}$$

[†] This expression readily follows from the differential form of Bragg's law: $0 = \Delta d \sin\theta + d\cos\theta\Delta\theta$. The different sign with respect to Eq. (3.9) is obtained from Eq. (3.7) by $\Delta\omega = -\Delta\theta$.

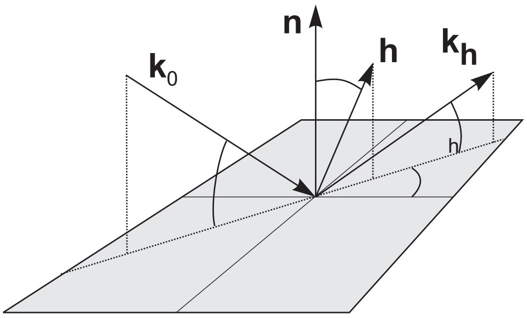

Figure 3.3: Diffraction geometry showing the incident beam $\mathbf{k_o}$, the diffracted beam $\mathbf{k_h}$, the reciprocal lattice vector $\mathbf{h}$ and the surface normal $\hat{\mathbf{n}}$. Note the coplanar geometry as all these vectors have the same azimuth ψ within the growth plane.

where the parallel strain $\epsilon_{\parallel}$ is uniquely determined by the degree of relaxation R on a substrate (or buffer layer) with in-plane lattice constant a_{s}

$$a = a_{\mathrm{s}} + R\left(a_{\mathrm{r}} - a_{\mathrm{s}}\right). \tag{3.15}$$

R ranges continuously from R=0 (coherent growth) to R=1 (fully relaxed layer). Finally, the perpendicular strain $\epsilon_{\perp}$ follows from Poisson's effect of continuum elasticity theory

$$\epsilon_{\perp} = -2\beta\epsilon_{\parallel}, \tag{3.16}$$

with $\beta = C_{12}/C_{11}$ for the zincblende and $\beta = C_{13}/C_{33}$ for the wurtzite structure, where the C_{ij} are the respective elastic constants. Both lattice constants and elastic constants are linearly interpolated for ternary alloys if information on a deviation from Vegard's law is not available.

Incident and diffracted beams In our simulation, we assume coplanar geometry, i.e., the incident and diffracted beams have the same azimuth ψ within the sample surface as the reciprocal lattice vector $\mathbf{h}$ (Fig. 3.3). The wavevectors for the incident and diffracted beams are given by

$$\mathbf{k_{o,h}} = \frac{1}{\lambda_{o,h}} \begin{pmatrix} \cos\theta_{o,h}\cos\psi \\ \cos\theta_{o,h}\sin\psi \\ \pm\sin\theta_{o,h} \end{pmatrix}, \tag{3.17}$$

where $\lambda_{o,h}$ is the x-ray wavelength in vacuum and in the medium, respectively, and

$$\theta_o = \Delta\omega + \theta_s - \phi_s, \quad \theta_h = \Delta\omega + \theta_s + \phi_s, \tag{3.18}$$

with the scan angle $\Delta\omega$ corrected for refraction, [44] and the Bragg angles and lattice plane inclinations [see Eq. (3.4), (3.5)]

$$\theta_s = \arcsin\left(\frac{h_{\mathrm{s}}}{2k}\right), \quad \phi_s = \arccos\left(\frac{\mathbf{h}_s \cdot \hat{\mathbf{n}}}{h_{\mathrm{s}}}\right), \tag{3.19}$$

where the subscript s denotes, as before, the substrate. h_{s} and k are the lengths of the reciprocal substrate plane lattice vector and the wavevectors, respectively.

Equations (3.6), (3.10)–(3.19) contain the approximate models published previously [37, 38] as can be easily derived by a Taylor expansion of corresponding order. The crucial advantage of our expressions is their applicability to materials with arbitrarily large lattice mismatch.

Recursive Takagi-Taupin algorithm We implement the above expressions into the recursive solution of the Takagi-Taupin equation for the dynamical simulation of diffraction profiles. The x-ray reflection amplitude of the n-th layer of a multilayer structure is then given in closed analytical form by [42,47,48]

$$\mathcal{X}_n = \eta + \zeta \frac{\sigma_- - \sigma_+}{\sigma_- + \sigma_+}, \tag{3.20}$$

with the deviation parameter

$$\eta = \frac{b\left[\alpha - \rho \mathsf{F}_0 \left(1-b\right)/2b\right]}{\rho\sqrt{|b|}\sqrt{\mathsf{F}_\mathsf{h}\mathsf{F}_{\bar{\mathsf{h}}}}}, \tag{3.21}$$

and

$$\zeta = \sqrt{\eta^2 - 1}, \quad \sigma_\pm = e^{\mp i\zeta\tau}\left(1 \pm \frac{\eta - \mathcal{X}_{n-1}}{\zeta}\right), \quad \tau = \frac{\pi\rho\sqrt{\mathsf{F}_\mathsf{h}\mathsf{F}_{\bar{\mathsf{h}}}}\, t\left(1+\epsilon_\perp\right)}{\lambda\sqrt{\left|\gamma_o^B \gamma_h^B\right|}}. \tag{3.22}$$

Here, $\rho = r_e\lambda_o/\pi V_C$ with the classical electron radius r_e and the unit cell volume $V_C = a^2 c$ for the zincblende and $V_C = \sqrt{3}a^2c/2$ for the wurtzite structure, $b = \gamma_o/\gamma_h$ is the asymmetry factor, the $\mathsf{F}_{\mathsf{h},\bar{\mathsf{h}}}$ are the structure factors of the corresponding reflection, t is the thickness of the layer, and γ_o^B and γ_h^B are the direction cosines at the exact Bragg condition of the respective layer.

To obtain the x-ray reflection amplitude for a multilayer structure, we start with the first layer ($n = 1$) at the bottom (i. e., the substrate) and $\mathcal{X}_0 = 0$. We then add layer upon layer until we reach the topmost layer. All parameters in the above equations are to be understood to apply to the respective layer in the recursion process, although the index n has been skipped for simplicity. The x-ray reflectivity is finally given by the reflection amplitude $\mathcal{X}$ of the topmost layer:

$$\mathcal{R} = \left|\frac{\mathsf{F}_\mathsf{h}}{\mathsf{F}_{\bar{\mathsf{h}}}}\right| \left|\mathcal{X}\right|^2. \tag{3.23}$$

3.5 Application to arsenide and nitride samples

Material parameters The practical use of the above stated model stands or falls by proper choice of materials parameters. For example, correct lattice constants but wrong elastic constants inevitably lead to inconsistencies and / or faulty compositions estimated. Hence, there is the need for parameters of highest possible precision.

A literature search has been performed in order to ensure that only the most reliable materials parameters (Tab. 3.1) are utilized. Whenever possible, data obtained by Brillouin scattering [49] and / or Bond measurements [50] are employed as these techniques are among the most accurate characterization tools for determination of structural and elastic properties.

Table 3.1: Material constants for the simulation of x-ray diffraction profiles. Note that β corresponds to C_{13}/C_{33} for nitrides and C_{12}/C_{11} for arsenides. If no information on a deviation from Vegard's law is available then all materials parameters are linearly interpolated for alloys.

	6H-SiC	GaN	AlN	InN	GaAs	AlAs
a_r (nm)	0.30806	0.31876	0.3112	0.3548	0.565359	0.566164
c_r (nm)	1.51170	0.51846	0.4982	0.5760	0.565359	0.566164
β	—	0.2551	0.3038	0.47	0.453	0.478
F_0	40.49−0.67i	73.01−1.56i	40.37−0.52i	110.85−10.53i	247.14+7.13i	181.13+5.00i
F_{004}	—	—	—	—	143.29+6.6i	105.85+4.79i
F_{224}	—	—	—	—	120.98+6.37i	91.68+4.68i
F_{117}	—	—	—	—	43.16−31.71	45.80−12.70i
F_{002}	19.77−0.61i	46.79−1.48i	19.20−0.45i	79.29−10.15i	—	—
F_{105}	−5.51−0.37i	−20.92−1.08i	−7.62−0.78i	−38.51−7.23i	—	—
F_{114}	6.67+0.43i	20.88+1.22i	5.25+0.29i	41.01+8.43i	—	—

The lattice parameters and elastic constants used in the present work for (Al,Ga)As largely rely on measurements of similar structures grown at the Paul-Drude-Institute. These values agree within the error margin of those determined by a combination [41] of Brillouin scattering and Bond measurements. This work represents, to the best of our knowledge, the most resolute and reliable attempts to accurately determine the actual composition of (Al,Ga)As taking into account any possible deviation from Vegard's law.

The lattice constants of 6H-SiC(0001) substrate wafers used in this work are taken from a recent report [51] on wafers from the same supplier (Cree Inc.) in order to provide a reliable reference for determination of the absolute diffraction angles of nitride samples. The most reliable measurement of the GaN lattice constants has been reported by Porowski [52] for GaN epilayers grown by molecular-beam epitaxy on perfectly lattice matched GaN bulk crystals. Data with equivalent precision for AlN and InN are, unfortunately, not available so that values from a recently published review [53] are used.

The elastic constants of nitride semiconductors used in this work originate from *ab-initio* calculations of Kim *et al.* [15] which have been demonstrated to be in excellent agreement with very recent, diligent experiments. [54]

All structure factors for both arsenides and nitrides were determined[‡] utilizing the most recent atomic scattering factors.

Computational realization of the model The above algorithm was readily implemented in two different environments. A C++ implementation processes about 100,000 points/s on an Athlon™ 750 whereas a Matlab® version processes around 50,000 points/s. The 10501 point simulation depicted in Fig. 6.3(a) for a structure with a total of 43 layers took 2.5 s in the C++ version. Compared to the sophisticated theory of De Caro *et al.* [12], the presented model is easier to implement, computationally more efficient and returns virtually identical results except for situations involving specular reflection.

Experimental All samples studied here are grown by molecular beam epitaxy. De-

---

[‡] employing the method described by S. Stepanov at `http://sergey.bio.aps.anl.gov/x0h.html`

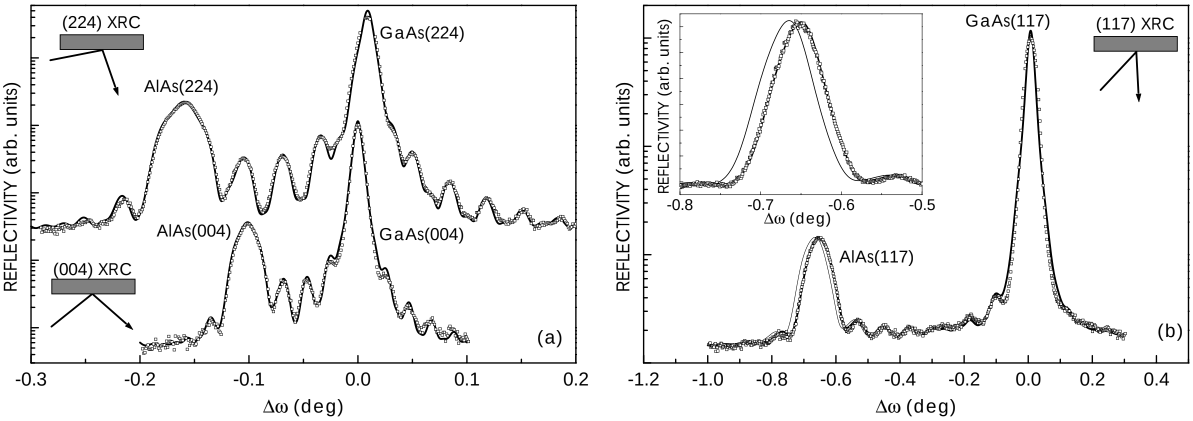

Figure 3.4: Experimental (squares) and simulated (solid line) rocking curves across (a) the symmetric (004) and the asymmetric (224) and (b) the asymmetric (117) reflection, respectively, for a heterostructure consisting of 229 nm AlAs on GaAs(001) and capped with 276 nm GaAs. The thin line in (b) displays the simulation based on the conventional first-order approximation. The deviation from the experiment is obvious, particularly in the inset. Note that for the (117) reflection, the broadening amounts to 80 arcsec. Since our instrumental setting is nondispersive, this broadening is due to crystal imperfections.

tails on the growth conditions for the nitride heterostructures can be found in the next Chapters of this thesis. Both symmetric and asymmetric x-ray rocking curves are recorded with a double-crystal diffractometer equipped with an asymmetricly cut Bartels-type Ge(022) monochromator with the detector wide open and staying at the Bragg angle of the substrate. All asymmetric reflections are measured in coplanar geometry with glancing incidence. symmetric θ-2θ scans are taken with a Bede D3 triple-axis diffractometer equipped with a Bartels-type Ge(022) monochromator and a Si(111) analyzer. Both systems utilize Cu Kα_1 radiation, and their instrumental broadening, accounted for in the simulations by convolution with a Lorentzian, amounts to 20 and 11 arcsec, respectively, unless otherwise mentioned. Our model is fit to the experimental data by a Levenberg-Marquardt routine. If several profiles were recorded, the data are fit simultaneously with identical parameters.

GaAs/AlAs/GaAs example Figure 3.4 shows the symmetric (004) and asymmetric (224) and (117) rocking curves of a structure consisting of a 229 nm thick AlAs layer overgrown by 276 nm GaAs, on GaAs(001). This sample serves as a model structure in order to test the ability of our approach to accurately describe the diffraction patterns of an essentially ideal crystal. Additionally, the results demonstrate that the conventional first-order approximation fails already in the closely matched materials system GaAs / AlAs, if appropriate reflections sensitive to strain are selected. In fact, despite the low strain in the present structure, the conventional first-order approximation is unable to exactly reproduce the angular position of the AlAs reflection, particularly so for the (117) reflection [Fig. 3.4 (b)]. Any attempt to fit this profile with the first-order approximation thus would lead to the use of incorrect lattice constants and / or elastic constants. Even then, however, it proves to be impossible to fit all profiles consistently with one set of lattice constants and elastic constants. In contrast, our model exactly reproduces all experimental profiles with our choice for the parameter (Tab. 3.1).

AlN/GaN/SiC example In Fig. 3.5, we show the rocking curves of a structure consisting of a 250 nm thick AlN layer on a 900 nm thick GaN layer, on 6H-SiC(0001). Despite

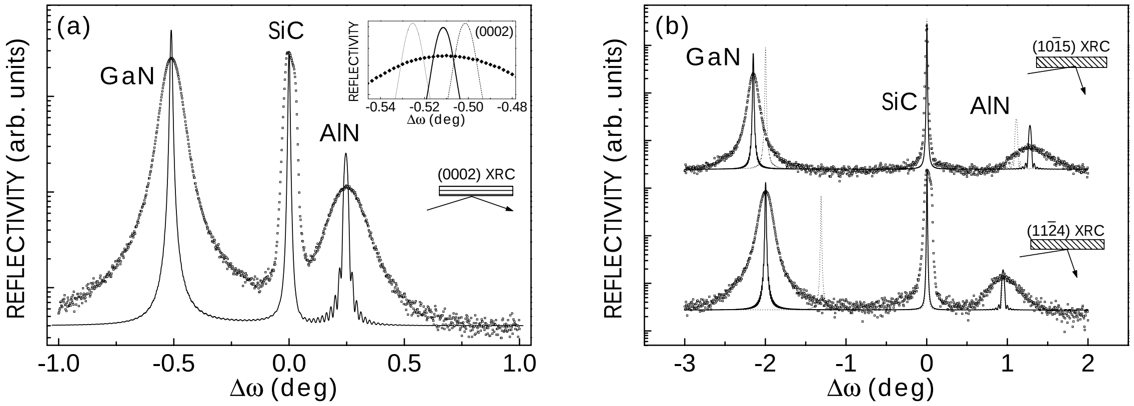

Figure 3.5: Experimental (squares) and simulated (solid line) rocking curves across the (a) symmetric (0002) and (b) the asymmetric $(10\bar{1}5)$ and $(11\bar{2}4)$ reflections for a heterostructure consisting of 900 nm GaN on 6H-SiC(0001), capped with 250 nm AlN. The dashed lines display the simulations based on the conventional first-order approximation. In the inset, the rocking curve in the vicinity of the (0002) reflection is shown together with the simulations based on the current model (solid line) as well as on first-order (dotted) and second-order (dashed) approximations.

the significant broadening of the reflections due to mosaicity induced by a dislocation density on the order of 10^9 cm^{-2}, the peak positions are still sufficiently well-defined for a quantitative determination of the strain state of GaN-based layers. The broadening may, in fact, be actually seen as an advantage: rocking curves can be acquired very rapidly and are thus ideally suited for the routine assessment of the layers' structural properties. A direct kinematical analysis of the three profiles with Eq. (3.6), however, proves to be not as accurate as desired. Since we have more equations than unknowns, the problem is overdetermined, and a simultaneous solution may not exist due the inherent imprecision in determining the exact angles of the reflections. Independent solutions, on the other hand, will generally yield values for the strain components which differ from each other. In contrast, by approaching the problem indirectly and simulating the profiles with our model, we easily achieve a unique solution. The theoretical profiles shown in Fig. 3.5 are all calculated with the same parameter set, namely, a residual tensile strain in the GaN layer of 0.05%, and a degree of relaxation of 0.9 for the AlN layer.

Failure of approximations for nitride examples We stress that, because of the large mismatch between the constituents and the correspondingly large angular range, these profiles by far exceed the validity of both first- and second-order approximations, which are consequently unable to reproduce these profiles with reasonable values for the lattice strains. Particularly, neither first- nor second-order approximations are able to reproduce these profiles with the same parameter set, in contrast to our model. If we rely on the symmetric reflection alone, the first-order approximation would return a far too high tensile strain within the GaN layer, while the second-order approximation would even indicate a compressive strain state.

To give an idea about the maximum error one is likely to encounter when using the first-order approximation: if we were to analyze a fully strained InN film (which is, of course, a most unlikely proposition) by the first-order approximation, and we would rely solely on the symmetric (0002) reflection, the result would suggest that the layer is partly relaxed with a relaxation degree of 0.5. If we would deal with an (In,Ga)N alloy of comparable strain, the In content would be underestimated by as much as a factor of two if assuming that the layer is fully strained.

Summary Concluding, we believe our model to be an efficient means for accurately determining strain-state and composition of highly mismatched materials systems. In comparison to a direct kinematical analysis, a unique solution is obtained more rapidly, and it additionally allows the determination of the layers' thicknesses and the interfacial quality.

4 Development and optimization of GaN heteroepitaxy on SiC(0001) and γ-LiAlO$_2$(100)

In this Chapter, we discuss the synthesis of GaN(0001) and GaN($1\bar{1}00$) layers on SiC(0001) and γ-LiAlO$_2$(100) substrates, respectively. These layers serve as buffer for subsequent growth of heterostructures. Hence the simultaneous accomplishment of a high morphological and structural quality of the GaN layer is required in order to realize heterostructures with smooth interfaces and low dislocation densities, respectively. Additionally, the carrier concentration of these buffer layers has to be controlled over a wide range for fulfilling the electrical demands of device structures, such as light-emitting diodes (high n-type conductivity) or heterojunction field-effect transistors (semi-insulating buffer layer).

This Chapter is organized as follows. First, a description of the molecular-beam epitaxy (MBE) system used for growth is given. Second, the two substrates utilized here, SiC(0001) and γ-LiAlO$_2$(100) are discussed. Third, the individual steps for the *reproducible* growth of GaN layers complying with the above mentioned quality criteria are presented.

4.1 MBE system and substrate mounting

All samples are grown by plasma-assisted molecular beam epitaxy (PAMBE) in a commercial three chamber system (modified RIBER-32) which was previously used for arsenides and antimonides. The growth chamber is equipped with a water-cooled radio-frequency N$_2$ plasma discharge cell (EPI) to supply active nitrogen and conventional effusion cells for the group-III elements Ga, Al and In and the dopants Si and Mg[*]. All cells are provided with mechanical shutters to abruptly switch on and off the individual beams. The fluxes of the effusion cells depend on the cell temperatures which are measured by thermocouples and controlled via feedback-loops which adjust the heating of the source elements. In the case of the plasma cell, the flux of active nitrogen is adjusted by the flow of N$_2$ into the cell and the excitation power. The fluxes of the effusion cells are very stable over a long time, but there is a loss in efficiency of the plasma source.[†] For a new cell, typical growth rates of 1 μm / h are achieved with a power of 200 W and a flow of 0.1 sccm[‡]. However, the efficiency dropped by more than two thirds after growth of about 100 samples. Subsequently, the source parameter values had to be continuously increased to 450 W and 0.5 sccm in order to obtain a growth rate of about 0.5 μm / h.

The base pressure of the growth chamber is below 10^{-10} Torr and maintained by ion-getter and Ti-sublimation pumps. During growth, the chamber is cryo-pumped and has a pressure around 3×10^{-5} Torr for typical N$_2$ flows of 0.2 sccm. The growth front

---

[*] During the first two months of this project, an As cell was installed in the Mg cell port in order to determine the individual fluxes of the Ga, Al, In and Si cells.

[†] The most likely reason for this deterioration in efficiency seems to be blocking of aperture holes of the source. In fact, cleaning of the aperture restored the efficiency to the as-received value.

[‡] 1 sccm is equivalent to a flow rate of 1 cm^3 at room temperature and atmospheric pressure per minute

is monitored *in-situ* by RHEED using a 20 kV electron gun under a glancing incidence angle of 1–2°. The diffraction pattern is recorded using a CCD camera.

The two substrate materials, SiC(0001) and γ-LiAlO$_2$(100), are transparent in the infrared emission range of the filaments utilized for sample heating. Thin absorbing metal layers which are evaporated onto the substrate backside are destroyed during the cleaning procedure of SiC before mounting (see below). It was therefore decided to mount the substrates with In on a Si wafer which is in turn mounted In-free on a Mo sample holder. This adhesive mounting is only stable if evaporation of In *between* substrate and Si wafer is minimized during the growth at around 700°C. Such a minimization is achieved by use of extremely thin In films which results in very reliable thermal contacts stable over the entire growth run which may take up to 10 hours.

After loading, the sample is thoroughly outgassed at around 400°C for two hours and transferred into the growth chamber. A thermocouple controls the sample holder temperature which, however, does not represent the actual temperature on the sample surface. The thermocouple temperature is therefore calibrated by the oxide desorption temperature of GaAs (580°C). All substrate temperatures given here thus correspond to the actual temperatures on the substrate surface.

4.2 Choice of SiC(0001) and γ-LiAlO$_2$(100) substrates

The aim of this work is to assess the individual steps for the growth of light-emitting devices such as light-emitting diodes (LEDs) or laser diodes (LDs). The first step is the choice of a suitable substrate. Table 4.1 compiles properties of various substrates currently used for group-III nitride epitaxy along the c-axis. [52, 55] For selecting the optimum substrate, several issues have to be considered which may be divided into growth related and device related ones.

For growth, it is generally accepted that lower lattice and thermal mismatches, smoother and cleaner surfaces as well as higher chemical and thermal stabilities result in lower defect densities. However, it is *a priori* not possible to predict if one substrate is better suited than another one from such numerical values, as epitaxial growth is influenced by a large number of parameters and effects. The ideal substrate for growth will be selected on the basis of experimental results and, of course, the price.

For device operation, it is easier to judge which substrate is best suited. A good choice will in general depend on the individual demands of the device. In the case of high-power applications, like LDs or FETs, the substrate acts as a heat sink. Thus, the thermal conductivity should be as high as possible. Furthermore, the best mirrors for LDs are usually obtained by cleavage such that at least one cleavage plane of substrate and epilayer should coincide. Finally, the price per device depends also on the number of required processing steps.

At the beginning of this work, it was decided to grow all GaN(0001) layers on SiC(0001) substrates. In the following it is outlined in detail why each of the other substrates was excluded.

GaN(0001) Outstanding structural, optical and electrical properties of GaN epilayers are published for homoepitaxial growth on bulk GaN substrates. [56] However, these substrates are not commercially available as—even after intense efforts—only

Table 4.1: Properties of substrates commonly used for GaN(0001) epitaxy. a, f, α and κ denote the effective in-plane lattice constant, the in-plane lattice mismatch, the in-plane thermal expansion coefficient and the thermal conductivity, respectively. The values in brackets for sapphire are obtained by a rotation of 30° around the GaN[0001] axis. SI-SiC(0001) stands for semi-insulating SiC(0001). The price corresponds to a 2-inch wafer.

Substrate	a (Å)	f (%)	α ($10^{-6}K^{-1}$)	κ(W cm^{-1} K^{-1})	Price ($)
GaN(0001)	3.1876	0	5.59	1.3	—
Al_2O_3(0001)	4.758 (2.747)	+49 (−13.8)	7.5	0.4	150
Si(111)	3.8396	+20.4	3.59	1.5	20
SiC(0001)	3.0806	−3.4	3.2	4.9	1000
SI-SiC(0001)	3.0806	−3.4	3.2	4.9	2000

tiny platelets (1 cm^2 area with a thickness well below 1 mm) have been obtained [52]. Possible alternatives are very thick (several hundred micrometers) free-standing GaN epilayers grown by hydride vapor-phase epitaxy (HVPE) on a conventional substrate like sapphire which is removed either by mechanical polishing or laser ablation. These free-standing layers are also not commercially available and exhibit high dislocation densities around 10^{10} cm^{-2}. The latter can be reduced to about 10^6 cm^{-2} by epitaxial lateral overgrowth (ELOG) on partially masked GaN epilayers [57] as practiced by Nichia for their commercially available continuous-wave LD. [58] However, the benefit of low dislocation densities comes at the expense of additional processing steps culminating in prices of around $2,000 for a single Nichia LD.

Si(111) The use of Si(111) with its extremely low price and excellent wafer quality is tempting but impeded by large defect densities originating from the large lattice mismatch to GaN, the high reactivity of Si with active nitrogen which may result in the formation of amorphous Si_xN_y during nucleation [59] and antiphase domain boundaries formed within the GaN epilayer due to single atomic steps on the Si(111) surface.

Al_2O_3(0001) Historically, sapphire is the substrate used for nitride epitaxy as it is inexpensive, chemically resistive and has a mature wafer preparation technology leading to smooth and clean surfaces. Excellent material quality meeting the requirements of even high brightness LEDs [60] is reported for layers grown on this substrate. This fact is very surprising considering the large lattice mismatch of +49% (reduced to −14% by in-plane rotation of 30° around the c-axis of GaN) and difference in thermal expansions coefficients to the basal plane of GaN. However, there are several drawbacks of sapphire. It is an electrical insulator such that mesa-etching is necessary for contacting. This processing step increases the required size and thus the real substrate costs per device are comparable to SiC(0001). Additionally, the poor thermal conductivity of sapphire seriously impedes its use for high power devices.

SiC(0001) Due to the excellent materials properties of GaN grown on SiC(0001) this material is a very promising substrate for growth. [61, 62] Furthermore, its cleavage planes coincide with those of GaN(0001). It is the best thermal conductor and can be made either electrically conducting or insulating. In the past, SiC(0001) was often abandoned because of inferior substrate quality due to poor polishing. However, the recent progress in H_2 etching of this surface (section 4.4) resulted in a morphological quality comparable to Si(111) or Al_2O_3(0001). The only drawback is the relatively high price of SiC which is, however, dropping at present due to increasing demand. At present, SiC(0001) is thus the best choice for LEDs as well as LDs and this material is now used by several companies such as, e.g., Cree, Fujitsu or Osram.

It seems as if sapphire or SiC are the ultimate choices for LEDs as these devices are already commercially available on these substrates (Cree and Osram on SiC, Nichia on sapphire). However, light generation in these nitride devices is handicapped by the presence of strong electrostatic fields (several MV / cm) within the active region due to huge electrical polarization fields *parallel* to the [0001] growth direction. There are two ways to evade these malevolent polarization fields. First, use of the zincblende phase or, second, growth of the wurtzite phase *normal* to the polar c-axis. However, even after intensive efforts [63] the growth of zincblende nitrides is still in its infancy displaying poor crystal quality and rough surfaces. Thus, the only option is to grow the wurtzite phase normal to the c-axis.

Wurtzite GaN has been grown so far only in the C-plane (0001) orientation despite attempts on various planes of sapphire like the A-plane ($11\bar{2}0$) or the R-plane ($1\bar{1}02$). In both cases, C-plane GaN(0001) and mixtures of different orientations of the zincblende and the wurtzite phase with extremely rough surfaces are found. [64–66] Additionally, the large densities of dislocations resulted in mosaicities up to 1°. The formation of GaN(0001) on these planes is due to the fact that GaN(0001) is the preferred orientation in the case of poor epitaxial match[§] as evidenced by the formation of GaN(0001) on amorphous silica glass. Thus, for a (new) growth direction off the GaN c-axis a (new) substrate with very low mismatch to that specific plane of GaN is mandatory. Other planes of SiC are no option as the different stacking sequences of the SiC substrate (6H or 4H) and the GaN epilayer (2H) will inevitably lead to antiphase domains boundaries. Also, the costs are too high (around \$1,500 per one-inch wafer) for LED mass production. Furthermore, the H_2 etching which is successfully employed for the C-plane of SiC cannot be applied to other surface orientations of SiC. In H_2 etching, the C-plane possesses the energetically most favorable orientation. Consequently, any attempt to polish other planes would utterly fail.

γ-LiAlO$_2$(100) At the beginning of this project, it was planned to employ γ-LiAlO$_2$(100) as an alternative substrate for GaN(0001) for investigating a device concept that was originally demonstrated for arsenides: the external quantum efficiency is substantially increased by enhancement of the escape probability of photons. [67]

In this concept, first the substrate is removed to obtain a free-standing epitaxial structure. γ-LiAlO$_2$ can be selectively etched with respect to GaN, in contrast to sapphire or SiC. The free-standing film is then bonded onto an integrated reflector. Hence, photons which are generated in the active region are not lost via absorption by the substrate. Furthermore, this processing step enables the production of on-chip LEDs. In a second step, the GaN surface may be textured by dry chemical etching [68] to reduce total internal reflection at the GaN / air interface.

In the course of the present work, it is discovered that γ-LiAlO$_2$(100) allows the fabrication of GaN($1\bar{1}00$). For the first time, growth off the ubiquitous GaN(0001) has been achieved. This unique finding is of extreme interest both scientifically and technologically. Several questions may be addressed regarding, for example, surface re-

---

[§] The natural reduction of mismatch by rotation around GaN[0001] does only apply to the basal plane of sapphire.

constructions, dopant incorporation and surface segregation. However, the most fascinating property of the GaN(1$\bar{1}$00) is the absence of any polarization vector component normal to the surface. Hence, electrostatic fields are not present in quantum wells. Light-emitting devices grown in this orientation are expected to have superior quantum efficiencies compared to their C-plane counterparts.

4.3 Crystal structures of the substrate surfaces and orientational relationships

The surfaces of both SiC(0001) and γ-$LiAlO_2$(100) are shown in ball-and-stick models in Fig. 4.1. Nucleation sites for GaN(0001) and GaN(1$\bar{1}$00) are indicated by dark and light shaded areas, respectively.

SiC(0001) Wurtzite SiC(0001) is available as both 4H and 6H modification. This surface offers hexagons as nucleation sites for GaN(0001) with a lattice mismatch of -3.4% [Fig. 4.1(a)]. The orientational relationship is

$$\mathrm{GaN}[11\bar{2}0] \parallel \mathrm{SiC}[11\bar{2}0] \quad \mathrm{GaN}[1\bar{1}00] \parallel \mathrm{SiC}[1\bar{1}00] \quad \mathrm{GaN}[0001] \parallel \mathrm{SiC}[0001]$$

γ-$LiAlO_2$(100) $LiAlO_2$ has a tetragonal unit cell with dimensions $a = b = 5.1687$ Å and $c = 6.2679$ Å and belongs to the space group $P4_12_12$. [69] Its (100) face is displayed schematically in Fig. 4.1(b). The commonly observed growth of GaN(0001) is believed to be the consequence of the quasi-hexagonal symmetry [dark shaded areas in Fig. 4.1(b)] on this surface. [70] The bond length in these hexagons varies from 2.875 to 3.301 Å for anions (O) and from 3.055 to 3.154 Å for cations (Li, Al). Thus, the local

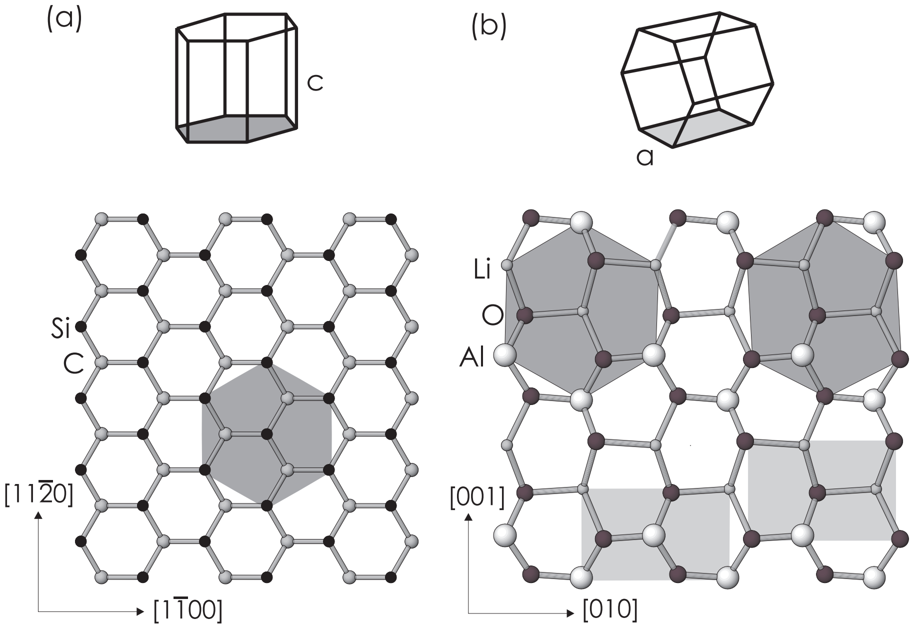

Figure 4.1: Unit cells and ball-and-stick models for the growth of GaN on (a) SiC(0001) and (b) γ-$LiAlO_2$(100). The dark and light shaded areas indicate nucleation sites for GaN(0001) and GaN(1$\bar{1}$00), respectively.

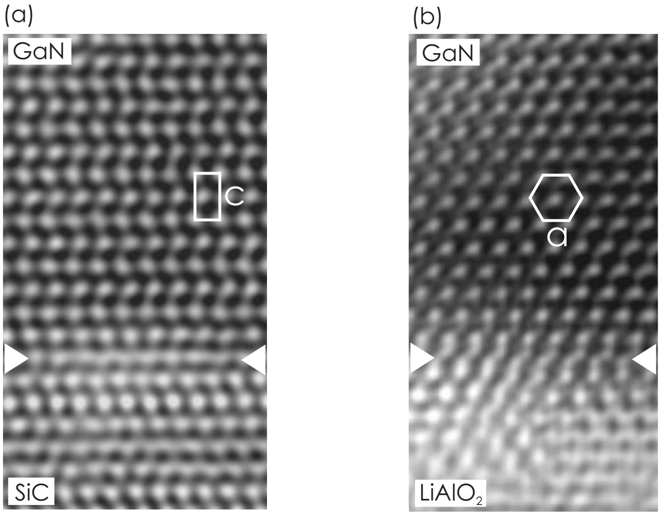

Figure 4.2: Cross-sectional high-resolution transmission electron micrographs of the GaN(0001)/6H-SiC(0001) interface along $[11\bar{2}0]$ in (a) and the GaN$(1\bar{1}00)$/γ-LiAlO$_2$(100) interface along [0001] in (b). Note the 2H stacking sequence in (a) and the hexagonal symmetry in (b).

mismatch to the GaN in-plane lattice constant may be as large as 10%.

However, as pointed out by Hellman *et al.* [70], the C-plane of GaN is not the orientation with the best match. Instead, the orientation relationship

$$\text{GaN}[0001] \parallel \gamma\text{-LiAlO}_2[010] \quad \text{GaN}[11\bar{2}0] \parallel \gamma\text{-LiAlO}_2[001] \quad \text{GaN}[1\bar{1}00] \parallel \gamma\text{-LiAlO}_2[100]$$

offers a superior match to M-plane GaN$(1\bar{1}00)$ with its lattice constants $a = 3.1876$ Å and $c = 5.1846$ Å as indicated by the light shaded areas in Fig. 4.1(b). The lattice match to GaN is better for the cation rectangle as it is less distorted than the anion rectangle and of identical size throughout. The size of the anion rectangle varies but its chemical match is better as it is composed solely of O.

Epilayer/substrate interface We now consider cross-sectional high-resolution transmission electron microscopy (HREM) images of GaN(0001)/SiC(0001) and GaN$(1\bar{1}00)$/γ-LiAlO$_2$(100) nucleated under optimized conditions (Figure 4.2). In (a) an atomically smooth interface is observed with a well ordered GaN(0001) epilayer. The interface in (b) is blurred due to the rough γ-LiAlO$_2$(100) substrate surface (see below). Besides these differences in interface quality the clear difference in crystal orientations is directly seen. In (a) the 6H stacking sequence of the substrate abruptly changes into the 2H stacking sequence of GaN, the GaN[0001] axis is thus perpendicular to the interface. In contrast, in (b) the hexagonal symmetry is visible, the GaN[0001] axis is parallel to the growth plane.

4.4 Substrate preparation before growth

As-received wafers The surfaces of commercially available SiC(0001) and γ-LiAlO$_2$(100) wafers as detected by atomic force microscopy (AFM) are shown in Fig. 4.3. As-received Si-face SiC(0001) wafers (Cree Inc.) usually exhibit a surface with

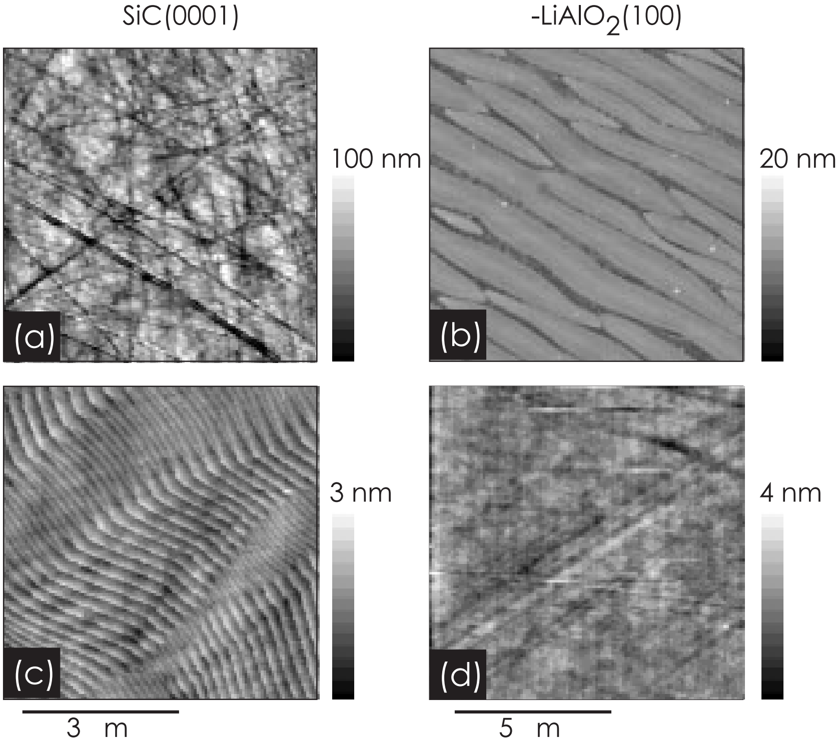

Figure 4.3: AFM images of SiC(0001) [(a),(c)] and γ-LiAlO$_2$(100) [(b),(d)] wafers. As-received wafers [(a),(b)] exhibit very rough surfaces whereas a significant improvement is observed for SiC(0001) after thermo-chemical H_2 etching (c) and for γ-LiAlO$_2$(100) after careful mechanical polishing (d).

scratches along different directions [Fig. 4.3(a)]. The peak-to-valley roughness amounts to 100 nm over an area of 3×3 μm^2. This poor surface quality leads to a high density of parasitic dislocations in the GaN epilayer. [71] Also the γ-LiAlO$_2$(100) wafers (MarkeTec Inc.) exhibit a rather poor morphology with long trenches along a preferential direction [Fig. 4.3(b)] and peak-to-valley roughnesses of 20 nm.

These surface morphologies originate from chemo-mechanical polishing leading to preferential scratches along the cleavages planes of the individual wafers. These are the three SiC$\{11\bar{2}0\}$ planes separated by 60° and the γ-LiAlO$_2$(001) plane. Additionally, TEM images of these as-received wafers clearly reveal damage layers extending to depths of around 200 nm. [71]

Ex-situ improvements of substrate surface For SiC(0001) substrates, a dramatic improvement in surface quality is attained after annealing the wafers to about 1600°C in flowing H_2. [72] At these temperatures, H_2 is cracked such that very reactive H atoms etch the surface with the SiC(0001) being the energetically favored plane. Etched wafers [Fig. 4.3(c)] exhibit a well-ordered array of unit cell high steps, separated by about 1 μm. The peak-to-valley roughness of these wafers amounts to values as low as 3 nm over an area of 3×3 μm^2. It is important to note that unit cell high steps have been etched as the stacking sequence of SiC (4H or 6H) differs from that of wurtzite GaN (2H). Thus, stacking mismatch boundaries would be formed at substrate surface steps if the step height does not match the periodicity of the GaN unit cell. Hence, multiples of the unit cell height and half of the unit cell height must be achieved for 4H and 6H SiC(0001) wafers, respectively. [73] Before mounting the substrates are degreased in trichlorethylen, acetone and methanol and hydrogen passivated for about 15 min by an HF dip to reduce oxidation of the substrate surface before loading. However, note that—in contrast to Si surfaces—the Si terminated SiC(0001) surface is only partially passivated by an HF dip. [74,75] This finding evidences the need for an *in-situ* cleaning step which is achieved here by Ga deposition and flash-off (see below).

γ-$LiAlO_2$ is a rarely used substrate and thus both bulk growth and wafer polishing are still in their infancies. The surface of γ-$LiAlO_2$ is roughened by acids such that the application of chemical solutions for chemo-mechanical polishing and cleaning is very restricted. Growth experiments on commercial γ-$LiAlO_2$(100) wafers always resulted in the formation of C-plane GaN(0001). Commercial wafers were abandoned because their poor surface quality. The substrates used here are 200 μm thick (100) oriented γ-$LiAlO_2$ wafers grown by the Czochralski method at the Institut für Kristallzüchtung and chemo-mechanically polished by a commercial vendor[¶]. The structural and morphological quality of these wafers is much improved compared to the commercial γ-$LiAlO_2$(100) wafers. Symmetric XRC widths below 25 arcsec are now routinely measured. Commercial wafers always exhibited multiple-peak x-ray diffraction profiles with total widths well in excess of 50 arcsec. The peak-to-valley roughness of these new wafers as detected by AFM is below 5 nm over an area of 10×10 μm^2 [Fig. 4.3(d)] which is a substantial improvement compared to values of around 20 nm as detected for as-received γ-$LiAlO_2$(100) wafers [Fig. 4.3(b)]. This surface roughness of these new γ-$LiAlO_2$ wafers is still only comparable to as-received SiC on a nanometer scale with no detectable atomic steps resolved. However, it was found that the better morphology of these wafers with respect to the commercial ones is crucial for the successful realization of GaN($1\bar{1}00$).

Before loading, the γ-$LiAlO_2$(100) substrates are degreased in an ultrasonic acetone bath for one hour as this cleaning steps does not attack the substrate surface.

In-situ treatment by Ga deposition and desorption During mounting and loading the substrate surface is in contact to ambient air and thus contaminated. Although outgassing removes a large fraction of these contaminants, like water, it would be desirable to have a method for substrate cleaning within the MBE system. For Si terminated surfaces, like SiC(0001), it was originally proposed by Kaplan [76] and experimentally verified by Strite *et al.* [77] that Ga can be used for cleaning. The strategy is to deposit Ga on the surface where it reacts with contaminants on the surface to form products like, e.g., Ga_2O. These reaction products and remaining Ga droplets are then desorbed at around 750°C by an annealing step. In principle, also Al or Si could be used for such a treatment but the low vapor pressures of these elements require substrate temperature for desorbing not compatible with the MBE system used for this work.

Before the first Ga treatment cycle a SiC(1×1) pattern is observed. During several cycles of the Ga treatment the intensity of the bulk streaks gains considerably, indicating a removal of contaminants. Furthermore, a threefold-reconstruction along the [$1\bar{1}00$] azimuth is observed after the first cycle (Fig. 4.4). The intensity of this reconstruction also increases with each cycle. A comparison with the literature suggests that a $(\sqrt{3} \times \sqrt{3})R30^\circ$ reconstructed SiC(0001) surface is obtained. This reconstruction is reported to be formed by a fractional monolayer of Si as determined by Auger electron

---

[¶] CrysTec GmbH Kristalltechnologie, Köpenicker Straße 325, D-12555 Berlin, Germany.

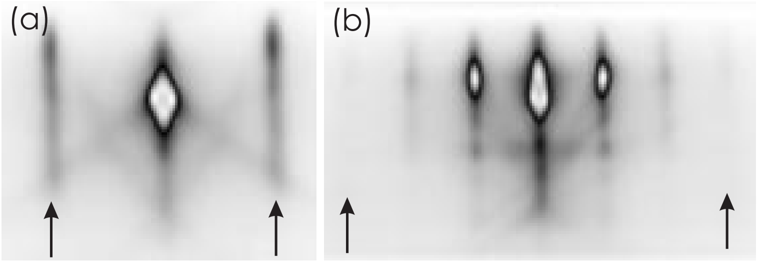

Figure 4.4: RHEED patterns along (a) $[11\bar{2}0]$ and (b) $[1\bar{1}00]$ of a H_2 etched 6H-SiC(0001) wafer after Ga deposition and flash-off. The arrows indicate bulk streaks. Note the appearance of the three-fold reconstruction in (b).

spectroscopy [78] and scanning tunneling microscopy [79].

The RHEED pattern of γ-LiAlO$_2$(100) before growth is streaky but diffuse compared to that of SiC(0001). Therefore, an analogous Ga treatment was also investigated on this material. However, no improvement in layer quality was detected and thus the Ga treatment is restricted to SiC.

4.5 Impact of AlN and GaN nucleation layers on SiC(0001)

Nucleation is generally believed to be the most critical step for achieving high-quality heteroepitaxially grown layers. The lattice mismatch to the substrate has to be relieved by the formation of misfit dislocations. For the -3.4% mismatch of GaN(0001) / SiC(0001) a misfit dislocation density around 10^{12} cm^{-2} is required at the interface. However, the density of dislocations penetrating the whole layer is determined by the nucleation conditions which thus have to be optimized. As a figure of merit, we choose—as generally done—the width of the x-ray rocking curve across the symmetric GaN(0002) reflection which is sensitive to the density of screw dislocations present in the layer. This measurement is ideally suited for routine characterization as it fast (15 min) and non-destructive. It has to be pointed out in this context that the width of the GaN(0002) reflection does not contain information on the density of edge type dislocations. In fact, this type of dislocation is detected in asymmetric scans as discussed in Chapter 5.

For deposition of GaN on SiC(0001), it is occasionally claimed that the use of AlN nucleation layers has a positive impact on materials properties. However, also conflicting results on the actual strain state of the samples have been published, i.e., both tensile and compressive strain states for yet unknown reasons (see the discussion in [80]). Indeed, the strain induced by lattice mismatch strain between GaN / SiC, GaN / AlN, and AlN / SiC is compressive as evident from the different in-plane lattice constants ($a_{\mathrm{GaN}} = 3.1876$ Å, $a_{\mathrm{AlN}} = 3.112$ Å, $a_{\mathrm{SiC}} = 3.081$ Å) at room temperature. If this mismatch is fully relieved during growth, however, cooling to room temperature introduces a tensile strain in the overlayers induced by the different thermal expansion coefficients ($\alpha_{\mathrm{GaN}} = 5.6 \times 10^{-6}$/K, $\alpha_{\mathrm{AlN}} = 4.2 \times 10^{-6}$/K, $\alpha_{\mathrm{SiC}} = 3.2 \times 10^{-6}$/K).

In order to systematically explore the difference in AlN and GaN nucleation layers a sample series is assessed. GaN layers of 1 μm thickness are grown either directly on SiC(0001) or on a 5 nm thin, coherently strained AlN nucleation layer. The two

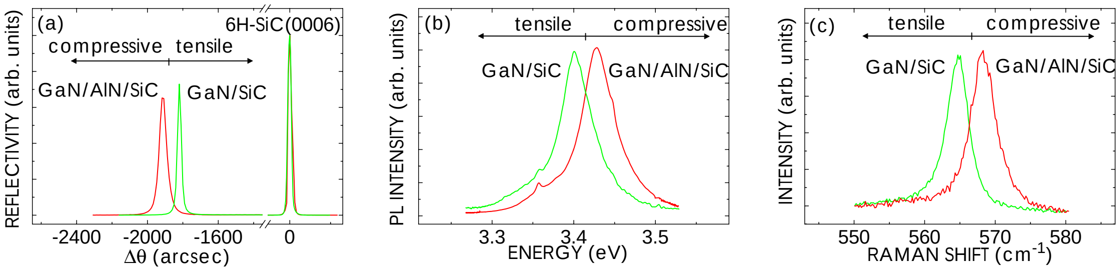

Figure 4.5: Strain state of GaN / SiC and GaN / AlN / SiC at room temperature as probed by the positions of (a) the GaN(0002) peak in XRD, (b) the free exciton transition in PL and (c) the E_2 phonon mode in Raman scattering. Note that GaN / SiC is under tensile strain whereas GaN / AlN / SiC is under compression.

sets of samples are grown under identical conditions. Nucleation is carried out at 660°C whereas growth of GaN takes place at 720°C. After growth the samples are cooled down at a rate of 10°C / min. The strain state of the samples is determined by a combination of XRD, photoluminescence (PL) and Raman[‖] measurements.

Figure 4.5 displays representative results of these measurements in comparison with resent values published for homoepitaxial, strain-free GaN layers. [16, 52, 81] These data reveal that GaN / SiC samples are—as intuitively expected—under tension whereas GaN / AlN / SiC samples exhibit compressive strain. This residual strain should originate from unrelieved lattice mismatch strain since the amount of tensile strain induced by cooling is the same due to the identical growth temperatures. Prior to this conclusion, however, we should examine three important questions. (i) Is the strain purely biaxial or does it have an additional hydrostatic component induced by point defects or impurities ? (ii) Is the strain homogeneous over the sample thickness ? (iii) What is the origin of these different strain states ?

(i) Nature of strain The exact nature of the strain can be determined by independent measurements of the lattice constants a and c as discussed in Chapter 3. With the lattice constants a_0 and c_0 of unstrained GaN [52], one gets the in-plane strain $\epsilon_{\|} = (a - a_0)/a_o$ and the out-of-plane strain $\epsilon_{\perp} = (c - c_0)/c_0$. The values for $\epsilon_{\perp}$ and $\epsilon_{\|}$ are found to be in good agreement with the relation for pure biaxial strain [Eq. (2.5)]. We thus conclude that any hydrostatic strain components, if present, average to zero and can therefore be neglected.

(ii) Homogeneity of strain Representative data probing the strain state of the layers are compiled in Tab. 4.2 in comparison with recent values for homoepitaxial GaN layers in the literature. [16, 52, 81] Information on the strain distribution may be gained from the different penetration depths κ of x-ray diffraction, photoluminescence (PL) and Raman measurements[**]: $\kappa_{\mathrm{PL}} < \kappa_{\mathrm{XRD}} < \kappa_{\mathrm{Raman}}$. We use Eq. (2.11) and (2.12) to convert the peak positions into biaxial strains $\epsilon_{\|}$. For analyzing the PL data, we assume that both the (D°,X) transition at 5 K and the free exciton transition at 300 K follow the shift ΔE_A [Eq. (2.11)].

The in-plane strains $\epsilon_{\|}$ of the whole set of samples are summarized in Table 4.3. Considering the uncertainty of the material parameters entering this determination, the

---

[‖] Details of the set-ups used for PL and Raman investigations are given in the next Chapter.

[**] The experimental set-ups for PL and Raman studies are presented in detail in the next Chapter

Table 4.2: Representative experimental data for GaN / SiC and GaN / AlN / SiC samples probing their strain state: angular position $\theta_{(0002)}$ of the GaN(0002) reflection in x-ray ω-2θ scans, spectral position E_{5K} of the (D°,X) PL transition at 5 K, spectral position E_{300K} of the free exciton PL transition at 300 K, spectral position E_2 of the E_2 phonon at 300 K. Reference values of unstrained material (GaN / GaN) are given for comparison. The ranges given are due to different samples.

	GaN / SiC	GaN / GaN	GaN / AlN / SiC
$\theta_{(0002)}$ (°)	17.292 ± 0.003	17.279 [52]	17.269 ± 0.002
E_{5K} (eV)	3.458 ± 0.006	3.470 [81]	3.480 ± 0.004
E_{300K} (eV)	3.405 ± 0.003	3.413 [81]	3.422 ± 0.006
E_2 (cm^{-1})	564.9 ± 0.9	566.2 [16]	568.9 ± 1.1

agreement of the strains deduced from different methods is quite satisfactory. This suggests that the strain is in fact homogeneous. The linewidths in x-ray $\omega - 2\theta$ scans (around 30 arcsec for all samples), being basically sensitive to inhomogeneous strain only, confirm this conclusion as they are comparable to values reported for unstrained GaN layers.

(iii) Origin of different strain states If lattice mismatch strain is fully relieved during growth, the amount of tensile strain induced by postgrowth cooling is about $\Delta T \times \Delta\alpha = +0.16\%$ according to our growth temperature and the thermal expansion coefficients. The GaN / SiC layers exhibit this strain and are therefore fully relaxed before cooling. The GaN / AlN layers, however, are still under compressive strain of roughly -0.15%, which means that even after 1 μm growth about one tenth of the 3.4% lattice mismatch is not relieved.

For clarifying the reason for this finding, we study the nucleation and growth of the GaN layer *in-situ* by RHEED (Fig. 4.6). Deposition of GaN directly on SiC results in three-dimensional growth as evident from the transmission diffraction pattern in (a) where the GaN layer is already fully relaxed. This result is not unexpected because of the large lattice mismatch (-3.4%) between GaN and SiC. However, the situation is different for the case of AlN nucleation layers. In agreement with reported values [82] of critical thicknesses of the -1% mismatched AlN / SiC interface, a 5 nm AlN grows coherently on SiC as evident by the coincidence of the AlN streaks with those of SiC. The streaky RHEED pattern furthermore reveals that the AlN surface is quite flat. Note, however, that the lattice mismatch between GaN and this strained AlN layer is

Table 4.3: In-plane strains $\epsilon_{\|}$ (percent) of GaN / SiC and GaN / AlN / SiC obtained by PL, Raman, and XRD. Note that positive and negatives values correspond to tensile and compressive strains, respectively.

	GaN / SiC	GaN / AlN / SiC
PL_{5K}	$+0.10 \pm 0.04$	-0.08 ± 0.03
PL_{300K}	$+0.07 \pm 0.03$	-0.07 ± 0.06
Raman	$+0.10 \pm 0.06$	-0.20 ± 0.08
XRD	$+0.14 \pm 0.03$	-0.11 ± 0.02

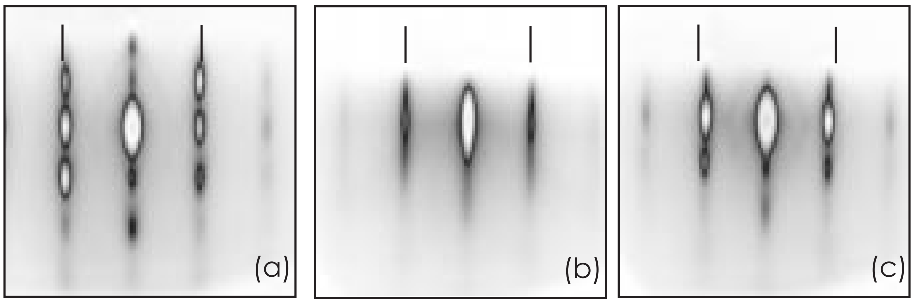

Figure 4.6: RHEED patterns along the $[11\bar{2}0]$ azimuth of (a) 5 nm GaN on SiC, (b) 5 nm GaN on 5 nm AlN / SiC, and (c) 40 nm GaN on 5 nm AlN / SiC. Lines indicate the positions of the diffraction spots of the SiC substrate.

the same as that between GaN and SiC. Nevertheless, GaN exhibits two-dimensional growth on the AlN layer as seen in Fig. 4.6(b) and roughens only after 40 nm of deposition as displayed in Fig. 4.6(c). This observation is supported by HREM images of the GaN / AlN / SiC heterointerfaces [Fig. 4.7(a)], where the smooth GaN / AlN interface can indeed be seen.

These results demonstrate that the growth mode of GaN is, in the present case, determined by its wetting rather than by the mismatch. The poor wetting of GaN directly on SiC [83] leads to pure three-dimensional nucleation favoring the formation of dislocations at the island edges [Fig. 4.7(b)]. In contrast, wetting is much improved for deposition on AlN, resulting in an initial two-dimensional growth with gradual strain relief [Fig. 4.7(c)]. The formation of strain relieving misfit dislocations then requires the system to overcome significant kinetic and energetic barriers for loop generation and dislocation glide, respectively. The driving force to do so, however, decreases when relaxation proceeds, and a residual compressive strain will thus continue to exist even to a very large thickness.

Despite the rather different growth modi during nucleation, the quality of both sets of samples, in contrast to results in the literature [83,84], is essentially identical. Independent of nucleation, the GaN(0002) XRC linewidth is around 600 arcsec and the width of the 300 K PL spectra is around 40 meV. As this XRC linewidth is still larger than the

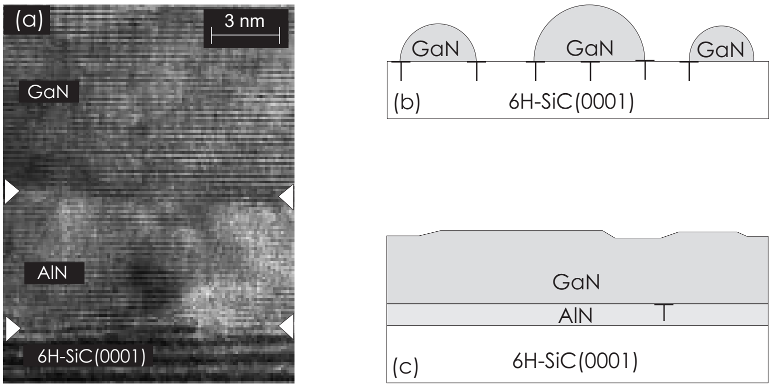

Figure 4.7: (a) HREM image of a GaN / AlN / SiC layer revealing an abrupt GaN / AlN interface. A schematic of the GaN / SiC and GaN / AlN / SiC growth is presented in (b) and (c). Note that the strain is fully relieved for GaN / SiC, whereas it is only partially relaxed for GaN / AlN / SiC.

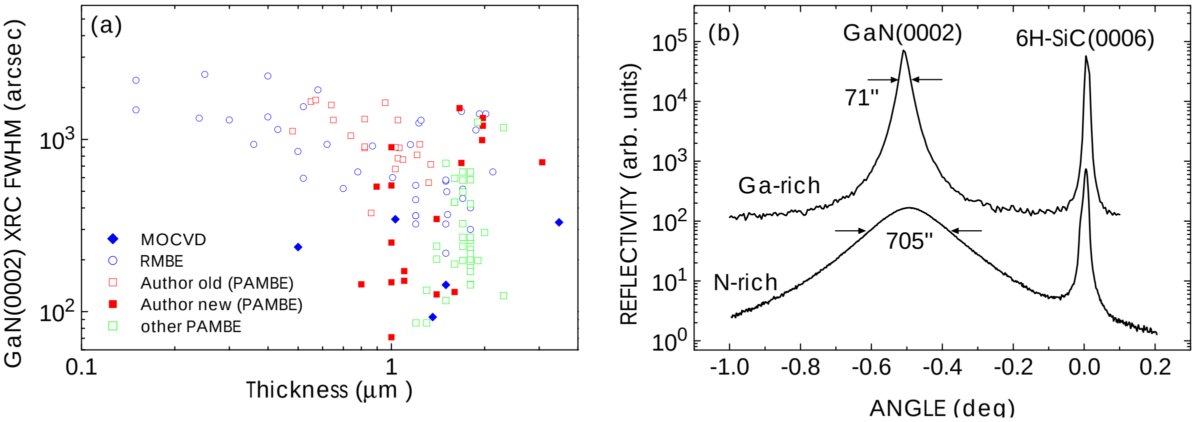

Figure 4.8: (a) XRC linewidths of samples grown by PAMBE, RMBE and MOVPE. Note that the linewidths for samples grown under optimized conditions are essentially identical for all three growth techniques. In (b), a direct comparison between N-rich and Ga-rich conditions demonstrates that Ga-rich conditions greatly improve the structural quality.

best values in the literature it is clear that nucleation is not yet optimized.

4.6 Optimization of nucleation

GaN(0001)/SiC(0001) Nucleation is carried out at different temperatures, surface stoichiometries and also using AlN and GaN as nucleation layer. The nucleation layers are overgrown with 1–2 μm GaN under identical conditions (see the next section) and the GaN(0002) XRC widths were compiled in a database. For comparison, this database also contains values of samples grown by reactive molecular-beam epitaxy (RMBE) at the Paul-Drude-Institute and metal-organic vapor-phase epitaxy (MOVPE) samples from different German research centers (IAF Freiburg and Universität Stuttgart). The results of this systematic study are shown in Fig. 4.8(a).

In the first period of optimization, the authors' samples ['Author old (PAMBE)'] were grown with an Oxford plasma source under various conditions but the XRC linewidth was on average around 500–1000 arcsec. Later on, a second MBE system was equipped with the Oxford source ['other PAMBE'] and the authors' samples ['Author new (PAMBE)'] were grown from then on with the EPI plasma cell (see the beginning of this Chapter). Further optimization of nucleation resulted in a substantial improvement as linewidths below 200 arcsec are achieved now *reproducibly*. In the course of optimization, identical conditions were established in both PAMBE systems. The sound agreement of XRD linewidths obtained by both of these PAMBE machines means that the obtained conditions do indeed reflect a general trend and are not restricted to a specific system. Furthermore, it is found that the achieved values are comparable to RMBE and state-of-the-art MOVPE layers [Fig. 4.8(a)].

The samples yielding the lowest XRC linewidths below 200 arcsec [Fig. 4.8(b)] are all grown with Ga-rich GaN nucleation layers at around 700°C. In contrast, N-rich nucleations [Fig. 4.8(b)] resulted in poor structural quality with linewidths around 1000 arcsec. Bearing in mind that the screw dislocation density is roughly inversely proportional to the square of the XRC linewidth a reduction in screw dislocation density by two orders of magnitude is thus achieved. This finding is in accordance with recent work. [61]

Since GaN(0001) is a polar surface, one has to examine if the nucleation leads to the Ga-face GaN(0001) or to the N-face GaN($000\overline{1}$). The surfaces associated with these two polarities differ in their surface reconstructions [85] and their stability during growth, as the N-face is less stable than the Ga-face resulting in rough surfaces of N-face grown samples. [86] Device structures, such as heterojunction field-effect transistors, even rely on the polarity as the inverted electrical polarization charges for opposite surface polarities require inverted layer sequences in order to generate a two-dimensional electron gas. A reliable polarity determination [86] is possible by wet chemical etching where the samples are put in 1.8 M NaOH solution at 50°C for 10 min. Scanning electron microscopy prior and after the etching did not reveal any change in morphology meaning that all samples, independent of nucleation, exhibit the Ga-face polarity.

GaN($1\overline{1}00$)/γ-LiAlO$_2$(100) In the beginning of this work, it was observed that GaN(0001) is formed on γ-LiAlO$_2$(100) wafers having rough substrate surfaces, like that in Fig. 4.3(b), regardless of nucleation conditions. These layers are accompanied by large mosaicities and macroscopic tilts of around 1° and 1.5°, respectively. However, the situation is different for substrates with a smoother surface [Fig. 4.3(d)]. Nucleation temperatures around 700°C still lead to GaN(0001) but the use of rather low temperatures around 570°C and metal-stable conditions resulted in the formation of GaN($1\overline{1}00$) with only little tilt and better crystal quality (linewidths around 1000 arcsec). In RHEED, the nucleation layer is three-dimensional, but clearly single-crystal GaN($1\overline{1}00$), with no detectable fraction of GaN(0001).

There is a significant difference in long-term stability between GaN($1\overline{1}00$) and GaN(0001) layers grown of γ-LiAlO$_2$(100). A strong tendency of C-plane oriented films grown on γ-LiAlO$_2$(100) wafers (induced by inferior morphological quality of the substrate) is observed to crack and to peel off the substrate due to strain induced by sample cooling after growth. In contrast, the M-plane oriented samples presented here did not degrade. This finding leads to the conclusion that the adhesion of M-plane samples is superior to that of their C-plane counterparts supporting again that M-plane is the favored orientation of LiAlO$_2$(100).

Two points have to be mentioned in this context. (i) Occasionally, GaN(0001) inclusions are detected by XRD and (ii) the linewidth of 1000 arcsec of the XRCs is still larger than that compared to the samples grown on SiC(0001) where values around 150 arcsec are routinely achieved. Both observations are most probably a result of the remaining surface roughness, the difficulties in substrate cleaning and the damage layer due to mechanical polishing. At present, the γ-LiAlO$_2$(100) substrates have a morphology comparable to as-received SiC(0001) wafers. Additionally, the substrate surface of γ-LiAlO$_2$(100) exhibits more contaminants than the SiC(0001) surface. We thus have to compare the present GaN($1\overline{1}00$)/LAO(100) with the non-optimized GaN(0001)/SiC(0001) samples. Here, the structural quality is nearly identical. One can thus expect that γ-LiAlO$_2$(100) substrates of similar quality to the optimized SiC(0001) wafers will also lead to GaN($1\overline{1}00$) layers with comparable structural quality as GaN(0001) grown on optimized SiC(0001).

4.7 Detection and adjustment of surface stoichiometry during growth

The growth behavior of crystals is, in general, determined by both bulk thermodynamics and surface kinetics. The correct choice of growth temperature and surface stoichiometry is very important for growth of high-quality crystals. However, for nonequilibrium conditions such as established during MBE, surface kinetics play the dominant role in growth. The reason for this fact is that the surface constitutes a two-dimensional phase in its own and has properties much distinct from the underlying bulk phase.

GaN(0001) The GaN(0001) surface behaves rather different than the traditional III-V semiconductor surfaces. In the case of the traditional III-V semiconductor surfaces such as, e. g., GaAs(001) growth of high quality material is possible over a wide range of surface stoichiometries, provided the V/III flux ratio is greater than unity. However, it has been demonstrated that the GaN(0001) surface is always Ga stabilized with no N atoms in or on top of the surface layer. [87] The only exception is the N (2×2) adatom structure which is found to be stable under very N-rich conditions. Total-energy density-functional theory calculations predict that Ga will be orders of magnitude more mobile than N adatoms at typical growth temperatures. [88] Furthermore, the presence of excess N on the surface, which can be formed under N-rich conditions, increases the migration barrier for Ga adatoms from 0.4 eV to 1.8 eV. This phenomenon reduces Ga adatom diffusion significantly as compared to a Ga-rich surface which exhibits very weak metallic Ga-Ga bonds (bear in mind that Ga has a melting point of 30°C). These theoretical results have also been confirmed by experiments, [89] evidencing that growth should proceed under Ga-stable conditions. This surface stoichiometry leads to highly mobile Ga adatoms and a two-dimensional growth front, whereas N-stable conditions result in poor Ga adatom diffusion and a rough surface with possible stacking faults. [88]

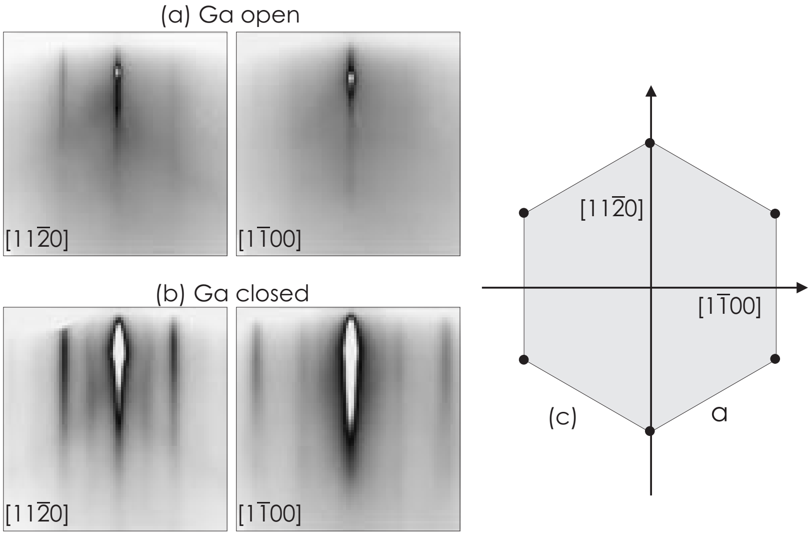

Figure 4.9: RHEED patterns for PAMBE growth of GaN(0001) during growth (a) and after closing the Ga shutter (b). Note the two-fold reconstruction in (b). The different azimuths are indicated in (c).

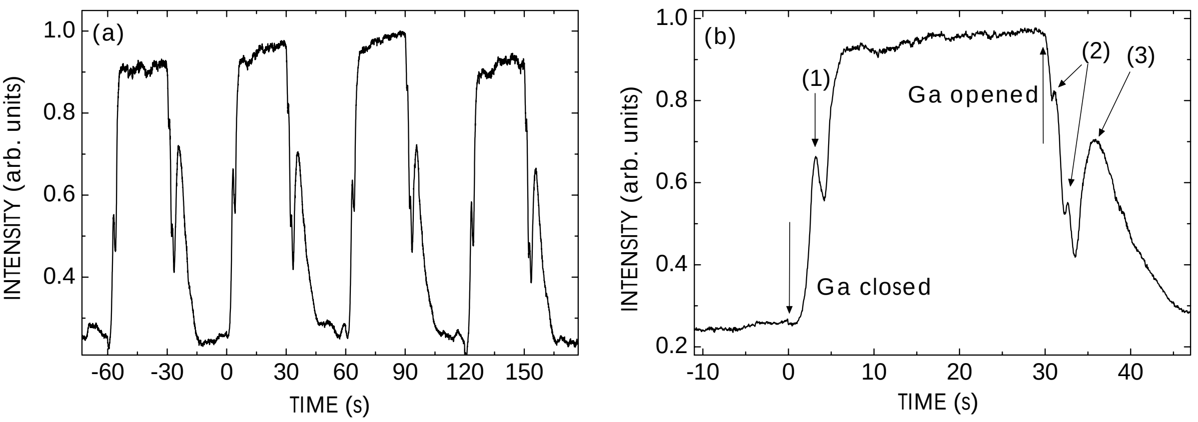

Figure 4.10: Variation of the specular spot intensity upon closing and opening the Ga shutter. The Ga shutter is periodically opened and closed for 30 s. Note the high reproducibility in (a). A magnified portion of one period in (b) reveals the presence of three distinct features labelled (1), (2) and (3).

However, great care is needed when growing under Ga-stable conditions in order to avoid the formation of Ga droplets on the sample surface. These droplets originate from too large Ga fluxes such that not all excess Ga is either desorbed or incorporated. Subsequent growth of GaN in the vicinity of these Ga droplets leaves behind undesirable crater-like irregularities on lateral length scales of several micrometers.

The optimum Ga-stable surface stoichiometry is often adjusted empirically on the basis of results from *ex-situ* measurements. [90, 91] However, this procedure is as cumbersome as it is unreliable, since stoichiometry is coupled to growth temperature. Decreasing the growth temperature, for example, reduces Ga desorption, and may result in Ga-rich growth and vice versa. Furthermore, the long-term loss in efficiency of plasma sources leads to changes in the active nitrogen flux even from one sample to the next.

Here, it is demonstrated that an *in-situ* determination of the surface stoichiometry is possible by monitoring the growth front by RHEED (Fig. 4.9). During growth, the (1×1) pattern is observed [Fig. 4.9(a)] with elongated streaks indicating a two-dimensional growth front that is covered with a Ga bilayer. [85] Upon closing the Ga shutter the intensity of the (1×1) pattern gains considerably due to both consumption of excess Ga under an active nitrogen flux and desorption of excess Ga. Finally, a transition to the N-rich (2×2) reconstruction [87] takes place [Fig. 4.9(b)]. The time period from closing the Ga shutter to observe the (2×2) pattern is a direct measure for the Ga coverage on the growth front. In our experience, recovery times below 5 s reflect N-stable growth, while recovery times exceeding 30 s will result in the formation of Ga-droplets. Experimental and theoretical investigations by Smith *et al.* [85] and Zywietz *et al.* [88] indicate that the (1×1) reconstruction on GaN(0001) under Ga-stable conditions results from a discommensurate adlayer of Ga on the surface of the film. This Ga adlayer significantly enhances Ga surface diffusion, as Ga adatoms have rather weak bonds to the metallic adlayer. Such an adlayer must be in equilibrium with the supplied, incorporated and desorbed Ga fluxes since we did not observe Ga droplets even after extended growth times when growing in the regime described above.

The intensity of the specular reflection as a function of time (Fig. 4.10) rises and falls upon closing and opening the Ga shutter, respectively. Additionally, oscillatory features labelled (1), (2) and (3) are seen in a very reproducible manner. Usually, oscillations of the specular spot are used to determine the deposition rate *in-situ* in the case of a sufficiently smooth growth front and island-nucleation. [92] For this purpose, growth is interrupted to further smoothen the growth front. Upon initiating the growth again, the intensity of the specular spot oscillates, where each period corresponds to the deposition of a complete monolayer.

Here, the growth rate is determined from *ex-situ* measurements of the film thickness by spectroscopic ellipsometry (see the next Chapter). In the present case, it has been found that the sample was grown at a rate of 500 nm / h corresponding to 2 s deposition time for a single monolayer. This rate agrees well with the period of the feature (2). The origin of the features (1) and (3) may be understood in the context of the presence of excess Ga on the surface during growth. Upon closing the Ga shutter, this excess Ga is consumed by the active nitrogen flux to form a single GaN monolayer resulting in an oscillatory modulation of the specular spot intensity. In contrast, opening of the Ga shutter will build up a floating layer of excess Ga on the growth front. Once a complete and fully connected Ga adlayer is formed, the RHEED intensity will gain considerably as seen by the presence of (3). Such Ga induced oscillations have recently also been observed for the deposition on 6H-SiC(0001) in the absence of an active nitrogen flux. [93] The time delay of feature (3) with respect to the Ga shutter opening is thus a direct measure of the time to build up the first complete adlayer of excess Ga, in this case around 7 s. It is important to bear in mind that this period (7 s) is not directly related to the general formation rate of excess Ga layers. The second Ga adlayer can only be stabilized by weak, metallic Ga-Ga bonds. Hence, the desorption rate of Ga atoms in this adlayer is substantially enhanced resulting in the observed equilibrium of delivered Ga flux, incorporated Ga and desorbed Ga.

GaN($1\bar{1}00$) For growth of GaN($1\bar{1}00$), there are no calculations regarding the optimum surface stoichiometry. This lack of activity is probably due to the lack of layers grown along this orientation. As a starting point, the optimum stoichiometries of the GaN(0001) growth were simply transferred to the GaN($1\bar{1}00$) plane. After nucleation at 570°C, the substrate temperature is raised to 700°C and growth is continued under Ga-stable conditions. The surface stoichiometry is estimated from the recovery time of the RHEED intensity after closing the Ga shutter since a surface reconstruction transition is not observed in agreement with theory. [28] The surface smoothens under Ga-stable conditions as evidenced by the transition from a spotty to a streaky (1×1) RHEED pattern. Figure 4.11 shows the RHEED patterns after growth of 1 μm GaN along four different azimuths. The azimuthal angles and the diffraction plane spacings deduced from the streak separations are given in the figure caption. Both the angles and the spacings agree with those for the four major azimuths of the GaN($1\bar{1}00$) surface, namely, the [$11\bar{2}0$], [$22\bar{4}3$], [$11\bar{2}3$] and [0001] directions [Fig. 4.11(e)].

4.8 Optimization of growth temperature

GaN(0001) After having ensured that samples are grown under optimized surface stoichiometry we now examine the substrate temperature. For hexagonal GaN, the lower limit is set by the transition to polycrystalline material (around 500°C). In order to en-

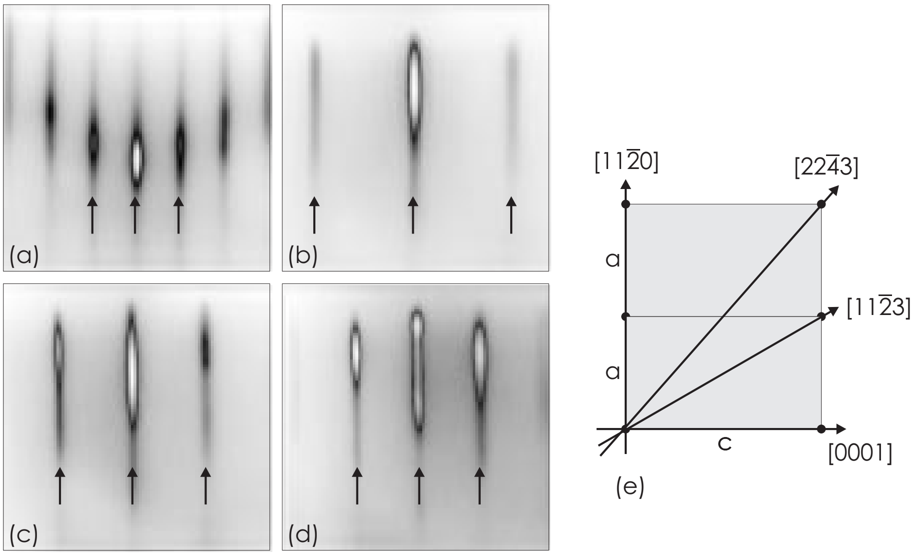

Figure 4.11: RHEED patterns of a 1 μm thick GaN($1\bar{1}00$) film recorded along azimuths of (a) 0°, (b) 38°, (c) 58° and (d) 90°. The arrows denote bulk streaks of zeroth and first order which corresponds to estimated lattice rod spacings of (a) 5.18 Å, (b) 2.01 Å, (c) 2.70 Å and (d) 3.15 Å. (e) shows a schematic of the ($1\bar{1}00$) plane with its in-plane lattice constants *a* and *c*. Calculating angles and spacings allows us to assign (a), (b), (c) and (d) to the $[11\bar{2}0]$, $[22\bar{4}3]$, $[11\bar{2}3]$ and [0001] directions.

hance adatom diffusion, a high temperature is desired, but thermal decomposition of the crystal represents the upper limit (around 800°C in the MBE environment). In order to enhance the migration length of adatoms and to minimize the density of point defects and unintentional doping, the best material should be obtained for growth at around half of the melting point (around 2500°C). This finding suggests growth well above the upper limit of 800°C for thermal decomposition. However, samples grown in a temperature range between 750 and 800°C exhibit the characteristic plateau-valley morphology [Fig. 4.12(a)] often observed for MBE-grown GaN samples [91,94]. In the RHEED pattern, this morphology is accompanied by steep facet chevrons which elongate during further growth towards the adjacent bulk reflections.

At first glance, one might explain this experimental finding with poor adatom diffusion suppressing island coalescence, tempting the grower to raise the substrate temperature. Recently, it was reported that the valleys found in AFM are terminated by

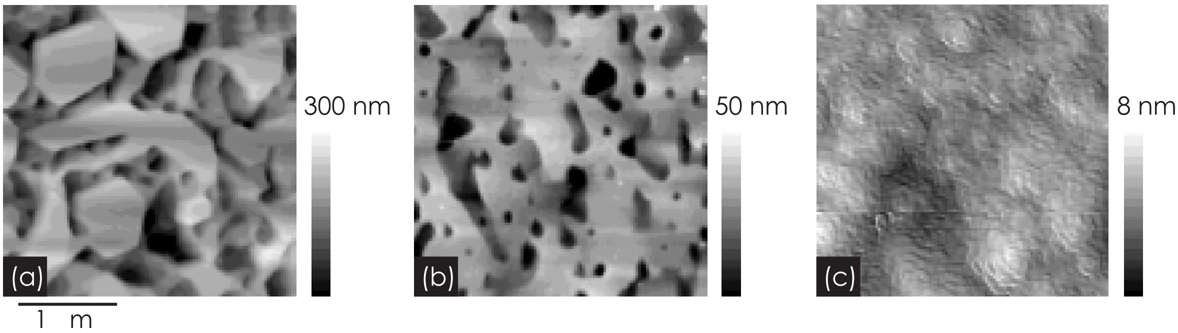

Figure 4.12: Surfaces of 2 μm thick GaN films grown at (a) 750°C, (b) 720°C and (c) 700°C as observed by AFM. Note the drastic improvement in morphology with decreasing substrate temperature.

dislocations. [91] The dissociation of GaN in the vicinity of these defects is expected to be higher than in the less disordered regions. At sufficiently high growth temperatures, evaporation will be significant and the surface will experience preferential thermal etching at defect sites resulting in the formation of grooves. [95] Indeed, a reduction in growth temperature to around 720°C leads to a clear improvement in morphology [Fig. 4.12(b)]. Finally, samples grown at 700°C exhibit an excellent surface morphology with clearly observable atomic steps [Fig. 4.12(c)] and terrace widths of the order of 100 nm. The root-mean-square roughness of these surfaces amounts to values as low as 1 nm over an area of $3 \times 3\ \mu\text{m}^2$.

GaN($1\bar{1}00$) The substrate temperature during GaN($1\bar{1}00$) growth is set to the same value (700°C) as that of GaN(0001). The RHEED pattern did not evidence any formation of facets at this temperature. Also, the surface morphology of samples grown at this temperature was not thermally etched at defect sites.

Summarizing, in this Chapter the reproducible growth of GaN in two different orientations, GaN(0001) and GaN($1\bar{1}00$), has been established. A detailed study of the impact of the different crystal orientations on various crystal properties is given in the next Chapter for representative samples.

5 Characterization of GaN(0001) and GaN(1$\bar{1}$00)

In this Chapter, we investigate structural, vibrational, optical and electrical properties of samples grown under the optimized conditions described in the last chapter. Representative examples for GaN(0001) and GaN(1$\bar{1}$00) are shown side-by-side for comparison.

5.1 Atomic force microscopy

The characteristic surface morphologies of GaN(0001)/SiC(0001) and GaN(1$\bar{1}$00)/γ-LiAlO$_2$(100) samples are presented in Fig. 5.1. In both orientations, the peak-to-valley roughness is below 10 nm with large terraces. This evidences that these buffer layers are suitable for subsequent growth of heterostructures with a minimized interface roughness. The two morphologies reflect the difference in arrangements of the surface bonds of the C-plane and the M-plane. For the GaN(0001) layer in (a) the terrace structure is isotropic whereas the GaN(1$\bar{1}$00) surface in (b) is rather anisotropic.

The GaN(0001) surface [Fig. 5.1(a)] is dominated by the presence of approximately 100 nm wide terraces separated by monoatomic steps. The overall root-mean-square roughness of such a surface amounts to values below 1 nm and is thus superior to that usually obtained by PAMBE. The GaN(0001) surfaces achieved here compare well with surfaces of films grown by MOVPE [96, 97] and the best surfaces reported for samples grown by RMBE [98] and PAMBE [61].

The most striking property of the GaN(1$\bar{1}$00) surface [Fig. 5.1(b)] is the anisotropic 'slate-like' morphology with extremely flat (1 nm peak-to-valley roughness over 1 μm) and elongated features running along [11$\bar{2}$0] separated by 2–3 nm high multisteps every 200 nm along the perpendicular [0001] direction. As the substrates used here are on-axis within 0.2° we can rule out the possibility of vicinal substrates leading to step–bunching. Vicinality would also lead to a significant difference in the number of upward and downward steps along [11$\bar{2}$0] which is clearly not the case here. More likely

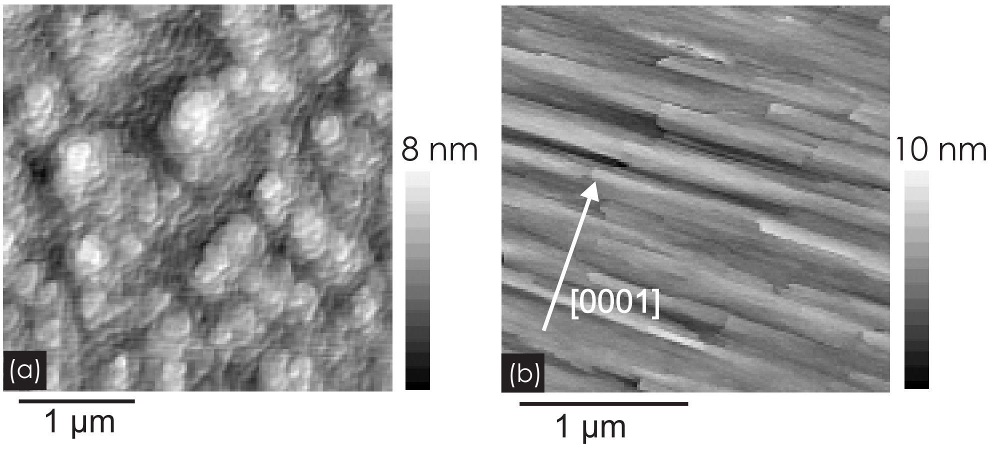

Figure 5.1: AFM images of 1.5 μm thick (a) GaN(0001) and (b) GaN(1$\bar{1}$00) layers, respectively. Note the existence of approximately 100 nm wide terraces in (a) and the anisotropy in (b) leading to a 'slate-like' morphology.

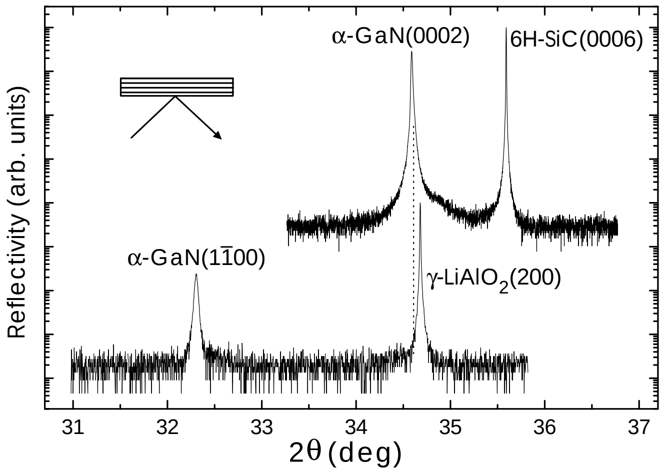

Figure 5.2: Symmetrical high-resolution θ-2θ scan around the γ-LiAlO$_2$(200) reflection together with a scan from a GaN(0001)/6H-SiC(0001) sample. Note the absence of the GaN(0002) signal for the sample grown on γ-LiAlO$_2$(100).

is that this surface is a consequence of growth kinetics. Distinct migration length of adatoms and different step structures exist along [11$\bar{2}$0] and [0001] similar to the case of high–index GaAs surfaces such as GaAs(331) where step arrays are oriented along [1$\bar{1}$0]. [99] However, even in the case of singular surfaces such as GaAs(001) the observed step configurations along the perpendicular [110] and [1$\bar{1}$0] directions are different. [100]

5.2 X-ray diffraction

In Fig. 5.2 high-resolution $\omega - 2\theta$ scans around the symmetric γ-LiAlO$_2$(200) and 6H-SiC(0006) reflections are shown for GaN(0001) and GaN(1$\bar{1}$00) films, respectively. The peaks at 17.28° and 16.15° correspond to the GaN(0002) and GaN(1$\bar{1}$00) reflections for the samples grown on SiC(0001) and γ-LiAlO$_2$(100), respectively. In both cases, only a single epilayer peak is detected evidencing the high phase purity of GaN films grown on these substrates. In particular, for the films grown on γ-LiAlO$_2$(100) no signal is observed in the vicinity of the GaN(0002) reflection, demonstrating that the fraction of GaN(0001), if any, is indeed very small.

The peak positions are consistent with the thermal mismatch of epilayer and substrate. A compression of 0.1% parallel to the growth direction is observed for GaN(0001)/SiC(0001) whereas a dilation of 0.3% is detected for GaN(1$\bar{1}$00)/γ-LiAlO$_2$(100). The linewidths of 25 and 40 arcsec are close to the experimental limit of the theoretical values (17 arcsec), i. e. the amount of inhomogeneous strain parallel to the growth direction is very small.

Wurtzite GaN(0001) exhibits mainly dislocation lines parallel to the [0001] direction. The Burgers vectors **b** are $1/3\langle 11\bar{2}0\rangle$, $\mathbf{b} = [0001]$ and $\mathbf{b} = \langle 10\bar{1}1\rangle$ for edge, screw and mixed-type dislocations, respectively. This specific dislocation geometry leads to a distortion of only specific crystal planes. Pure screw type dislocations lead to a tilt of the crystal and are thus readily detected in symmetric scans. Pure edge type dislocation lead to a twist around [0001] and thus do not distort on-axis planes so that symmetric

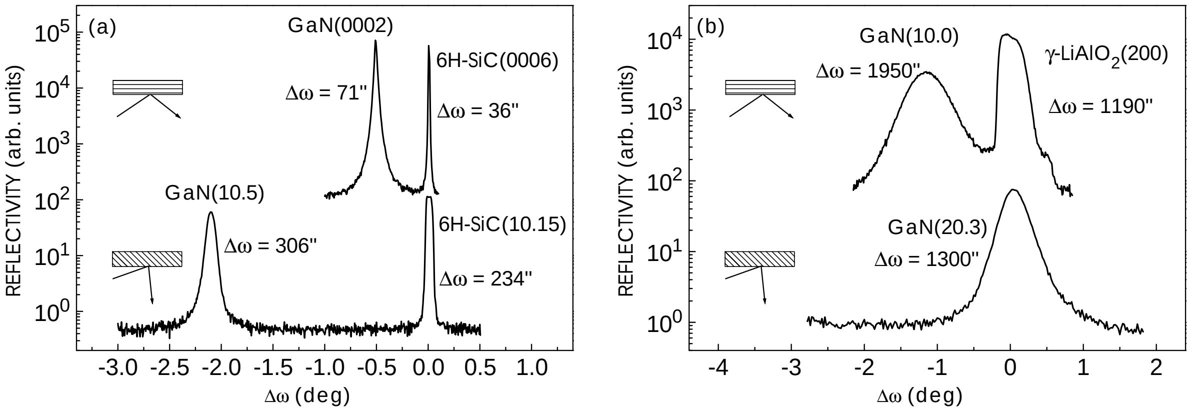

Figure 5.3: X-ray rocking curves of a 1.5 μm thick GaN(0001) film grown on (a) 6H-SiC(0001) and (b) γ-LiAlO$_2$(100). For both orientations, the top and bottom profiles are taken in a symmetrical and asymmetrical (glancing incidence) geometry. Note the absence of substrate reflections in the vicinity of the GaN(20$\bar{2}$3) reflection in (b).

scans are not sensitive to this dislocation type. In contrast, off-axis planes are distorted by all the above dislocation types and thus asymmetric scans are required to detect pure edge type dislocations. [45, 101]

XRCs from one azimuth Symmetric and asymmetric (glancing incidence) XRCs are measured for both GaN(0001) and GaN(1$\bar{1}$00) films (Fig. 5.3). For each sample, both scans are taken along the same azimuth, namely [1$\bar{1}$00] for GaN(0001) and [0001] for GaN(1$\bar{1}$00). The peak positions yield the lattice constants a and c whereas the widths of the reflections reflect the misorientations of the corresponding crystal planes due to the presence of specific dislocation types and thus act as a measure of defect densities.

As expected, we observe for the GaN(0001) film that the asymmetric linewidth is *larger* than the symmetric one as the latter is only sensitive to screw type dislocations. In contrast, the opposite behavior is observed for the GaN(1$\bar{1}$00) film where the asymmetric linewidth is *smaller* than the symmetric one.

We now examine the XRC results for each orientation in more detail. Linewidths below 100 arcsec and below 300 arcsec are obtained for the GaN(0001) film in the symmetric (0002) and asymmetric (10$\bar{1}$5) geometry, respectively. In comparison with the literature, these linewidths correspond to screw dislocations densities below 10^7 cm^{-2} and edge type dislocation densities below 10^9 cm^{-2}, respectively. [61] The widths of both the symmetric (1$\bar{1}$00) and the asymmetric (2$\bar{2}$03) XRCs from GaN(1$\bar{1}$00) films [Fig. 5.3(b)] are considerably larger than those of GaN(0001) films. A closer inspection of the x-ray profiles reveals substantially broadened substrate peaks. The rectangular shape of these peaks evidences wafer curvature which is most probably due to the thermal mismatch stress during post-growth cooling (see below). In order to account for this finding we therefore estimate the actual width of the epilayer peaks by subtracting the substrate peak width. Nevertheless, it is evident that the GaN(1$\bar{1}$00) film exhibits a larger linewidth and thus a larger density of defects. It is likely to assume that the inferior substrate quality of γ-LiAlO$_2$(100) with respect to SiC(0001) is responsible for this finding.

XRCs from different azimuths Hellman *et al.* [70] have observed a macroscopic tilt of GaN(0001)/GaN(1$\bar{1}$00) in agreement with our result in the last chapter. Therefore,

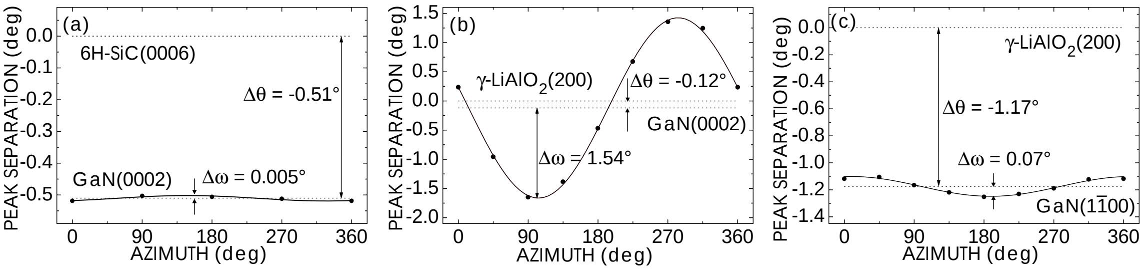

Figure 5.4: Angular separations of the epilayer and substrate peaks in XRCs as a function of azimuthal angle for (a) GaN(0001)/SiC(0001), (b) GaN(0001)/γ-LiAlO$_2$(100) and (c) GaN(1$\bar{1}$00)/γ-LiAlO$_2$(100). The data are fit with a simple sinusoidal expression yielding the Bragg angle separation $\Delta\theta$ and the macroscopic tilt $\Delta\omega$.

we investigate if GaN(1$\bar{1}$00) grown on γ-LiAlO$_2$(100) also exhibit such a tilt. XRCs are taken from different azimuths such that any macroscopic tilt would manifest itself as a periodic modulation of the angular separation of epilayer and substrate peak.

In Fig. 5.4 the results for (a) GaN(0001)/SiC(0001), (b) GaN(0001)/γ-LiAlO$_2$(100) and (c) GaN(1$\bar{1}$00)/LAO(100) are presented. From fits with a sinusoidal function we get both the average peak separation $\Delta\theta$ of the Bragg angles and the macroscopic tilt $\Delta\omega$ which is the oscillation amplitude. The values for $\Delta\Theta$ are in good agreement with the Bragg angles of 17.79°, 17.32°, 17.28° and 16.20° of the SiC(0006), γ-LiAlO$_2$(200), GaN(0002) and GaN(1$\bar{1}$00) planes, respectively. The slight deviations from the theoretical values are due to a compressive thermal mismatch for GaN layers grown on γ-LiAlO$_2$(100) and a tensile one on SiC(0001).

We now consider $\Delta\omega$. For GaN(0001)/SiC(0001) and GaN(1$\bar{1}$00)/γ-LiAlO$_2$(100) we observe an almost constant separation demonstrating negligible tilts. The measured tilts of 0.005° and 0.07° result from the residual substrate miscut of up to 0.2°. This fact would lead to anisotropic dislocation generation rates and thus a tilt of the epilayer. GaN(0001)/γ-LiAlO$_2$(100) exhibits a macroscopic tilt of around 1.5° in good quantitative agreement with the results of Hellman *et al.* [70]. However, there is no *a priori* reason for such a large tilt. Hellman *et al.* [70] proposed that the interface energy is reduced via the tilt because of the ionic nature of the interface bonds. The tilt calculated by these authors (0.55°) is within the range of the values determined in the present work, but certainly more experimental effort is required to resolve this issue.

Furthermore, two interesting observations are made when taking x-ray rocking curves of GaN(1$\bar{1}$00)/γ-LiAlO$_2$(100) samples from different azimuths. First, the width $\Delta\omega_{\text{sub}}$ of the substrate peak increases from 0.1° to 0.3° when the x-ray beam is oriented along the GaN[11$\bar{2}$0] and GaN[0001] directions, respectively. This broadening originates in strain–induced wafer bending. The radii r of curvature along these crystallographic directions can be estimated from $l = r \times \Delta\omega_{\text{sub}}$ where $l \approx 0.5$ cm is the size of the x-ray beam spot on the sample. From r we calculate the in-plane stresses [102] of the epilayer and arrive at values of 1.2 GPa and 0.4 GPa along [0001] and [11$\bar{2}$0]. These values are in fair agreement with the stress values obtained from the stress-strain tensor, taking the out-of-plane strain deduced from the high resolution x-ray diffraction scan and assuming that the in-plane strain of the layer is solely due to the thermal mismatch to the substrate. Second, also the peak widths $\Delta\omega_{\text{epi}}$ of the epilayer peak depend strongly on azimuth. After correction for substrate curvature, we obtain $\Delta\omega_{\text{epi}}$=0.22° parallel

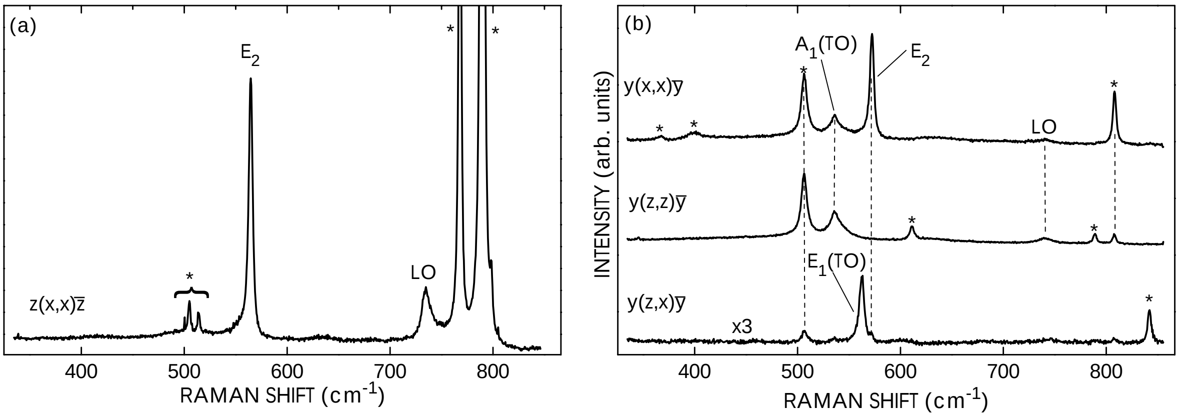

Figure 5.5: Raman spectra of 1.5 μm thick GaN(0001)/6H-SiC(0001) and GaN($1\bar{1}00$)/γ-LiAlO$_2$(100) films. Asterisks refer to peaks originating from the substrate. 'x', 'y' and 'z' correspond to the [$11\bar{2}0$], [$1\bar{1}00$] and [0001] directions, respectively. Note the vanishing intensity of the E$_2$ phonon mode in the second geometry in (b).

to GaN[0001] and $\Delta\omega_{\mathrm{epi}}$=0.85° parallel to GaN[$11\bar{2}0$]. This anisotropy in mosaicity evidences an anisotropic defect structure.

5.3 Raman scattering

The vibrational properties of GaN(0001) and GaN($1\bar{1}00$) at room temperature are examined by Raman scattering using the 514.5 nm line of an Ar$^+$ ion laser in the backscattering geometry

Fig. 5.5 shows Raman spectra of GaN(0001) and GaN($1\bar{1}00$) epilayers. The GaN(0001) sample in (a) is examined such that polarizer and analyzer are parallel. We observe the same spectrum, which is dominated by the E$_2$ phonon mode, in all in-plane orientations since the sample is isotropic within the growth plane. The position of the E$_2$ mode at 566 cm^{-1} corresponds to a tensile biaxial strain of 0.1% within the growth plane according to Eq. (2.12).

The GaN($1\bar{1}00$) plane is anisotropic and therefore three different in-plane geometries are employed [Fig. 5.5(b)]. In the first two scans, polarizer and analyzer are parallel but the directions of both are rotated by 90° around the surface normal. In the third scan, polarizer and analyzer are normal to each other. There are no published Raman data on γ-LiAlO$_2$, so first the surface and the edges of a bare γ-LiAlO$_2$(100) substrate are scanned. This procedure allows us to identify the γ-LiAlO$_2$(010) face which is equivalent to the known γ-LiAlO$_2$(100) substrate surface. Thus, an in-plane orientation of overgrown substrates is obtained. Next, the Raman peaks originating from the GaN($1\bar{1}00$) epilayer are investigated and compared with the GaN(0001) data.

The in-plane orientation of the *c*-axis in GaN($1\bar{1}00$) is seen from the top two scans in Fig. 5.5(b). In the top scan the E$_2$ mode is present while it is absent in the second scan. Thus, the *c*-axis is perpendicular to polarizer and analyzer in the top scan. This finding also indicates the phase purity of our samples, as GaN(0001) contributions would lead to a non-vanishing E$_2$ signal in both geometries. Our relative phonon line intensities in all three scans are consistent with the selection rules for the ($1\bar{1}00$) plane.

They are in fact almost identical to those obtained by Azuhata *et al.* who examined the GaN($1\bar{1}00$) cleavage plane of a 100 μm thick GaN(0001) epitaxial film. [103] The excellent agreement between their data and our data is further evidence for the phase purity of the samples. The position of the E_2 phonon line at 572.5 cm^{-1} is a direct measure of the strain in the layers. As an estimate, we obtain a compressive hydrostatic strain of -0.3% according to Eq. (2.12). This strain state is at least partially due to the thermal mismatch of GaN($1\bar{1}00$) and γ-$LiAlO_2$(100), which is compressive along both in-plane directions [010] and [001] of γ-$LiAlO_2$(100).

Additionally, the Raman experiments evidence the in-plane orientation of the epilayer with respect to the underlying substrate. It has been found that the two optical axes γ-$LiAlO_2$[001] and GaN[0001] are normal to each other. As we also know that the *c*-axis of GaN lies in the interface, we deduce that GaN[$11\bar{2}0$] is normal to γ-$LiAlO_2$[010]. Thus, we obtain exactly the orientational relationship given in Fig. 4.1(b).

5.4 Ellipsometry and Photoluminescence

The combination of spectroscopic ellipsometry (SE) and photoluminescence (PL) allows the investigations of three optical properties: reflection (SE), absorption (SE) and emission (PL). These properties are coupled and it is thus instructive to examine the results in a single section.

Wurtzite GaN has a direct band gap of 3.46 eV at room temperature and 3.51 eV at liquid helium temperature. [81] However, the strain state shifts the band gap according to Eq. (2.11) such that a blue-shift or a red-shift is observed for compressive or tensile strain, respectively. The effective masses for electrons and heavy holes are 0.2 m_0 and around 1 m_0, respectively. [104] These masses lead to a binding energy of 25 meV for the free A exciton. However, this value is only approximate due to the scatter in effective heavy holes masses reported. [53] Activation energies for donors and acceptors are around 30 meV and 150 meV in the hydrogen model since the relative dielectric constant amounts to 9.77 directly at the GaN band gap. [105] At room temperature, these energies lead to a large fraction (about 50%) of ionized donors and a relatively low fraction (about 1%) of ionized acceptors.

Set-ups for spectroscopic ellipsometry and photoluminescence For SE, a Hg lamp is used with an incident angle of 70° normal to the sample surface. Measurements are carried out at room temperature. For PL, the samples are excited by the 325 nm line of a 50 mW He-Cd laser and the luminescence is dispersed by a grating with 600 lines / mm and detected by a liquid nitrogen cooled CCD camera. The data are carefully corrected for the spectral dependence of the set-up. The excitation density is adjusted by neutral density filters and measured using a calibrated powermeter. If not otherwise stated, the excitation intensity is 0.1 W cm^{-2}. The sample is mounted on the cold finger of a cryostat whose temperature can be varied in the range from 5 to 500 K. Great care is taken in order to provide reproducible measurement conditions for comparison of different measurements. This issue is addressed using a reference sample with is mounted side-by-side with the other samples.

Spectroscopic ellipsometry at 300 K SE measures the complex index of refraction $\tilde{n} = n + i\kappa$. It offers a number of advantages which makes it ideal as a routine char-

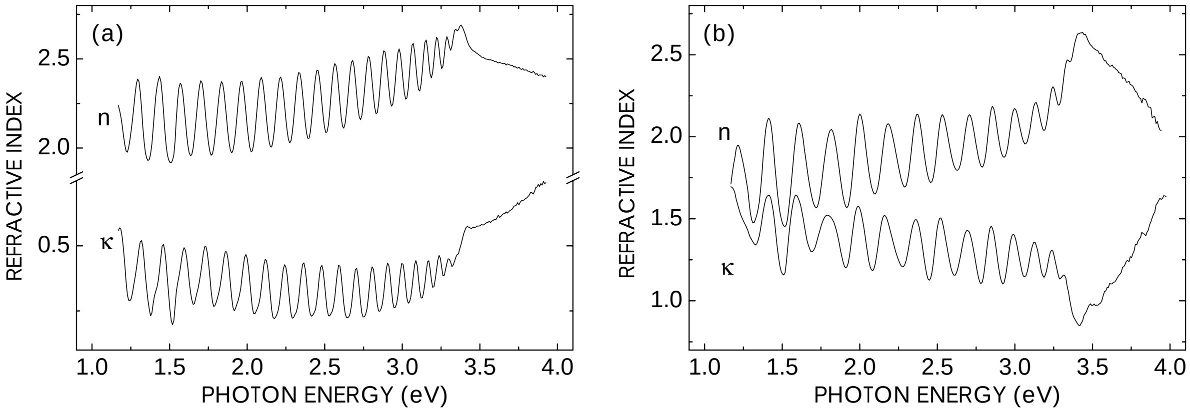

Figure 5.6: Complex pseudo-refractive index $\tilde{n} = n + i\kappa$ for (a) GaN(0001)/SiC(0001) and (b) GaN(1$\bar{1}$00)/γ-LiAlO$_2$(100) as determined by SE.

acterization. It is a non-destructive and fast thickness measurement technique, gives information on the morphological and optical quality and can be used to extract chemical compositions.

Figure 5.6 shows n and κ for GaN(0001) and GaN(1$\bar{1}$00) samples. For photon energies below the band gap of GaN the epilayer is transparent. The measurement thus yields a pseudo-refractive index which is modulated by interference fringes due to the finite thickness t of the epilayer forming a cavity between air and substrate. The spectral positions E_m of constructive interferences

$$2t\sqrt{n^2 - \sin^2 \varphi} = (m + 1/2)\frac{hc}{E_m} \tag{5.1}$$

depend only on the angle of incidence φ and the order m of the interference. Since the absolute orders m of the interferences are unknown we first solve for $t = t(m, E_m)$. This expression relates the spectral positions E_m of the constructive interferences with their absolute order and the sample thickness t. The correct choice of the lowest-energy interference will minimize the scatter in t which is thus obtained using a simple least-square fitting routine. For the data in Fig. 5.6 thicknesses of (2449±46) nm and (1513±41) nm are determined for (a) and (b), respectively.

Furthermore, interference fringes directly offer a measure of the morphological quality of the sample. A smooth surface leads to well-resolved fringes whereas they are damped by surface roughness. Higher order interferences disappear first as they rely on the constructive interference of shorter wavelengths than the lower order interferences.

One can clearly see that the imaginary part κ, describing absorption, does have different absolute values for GaN(0001) and GaN(1$\bar{1}$00). We have to note that below the band gap of the epilayer the measurement basically reflects the absorption of the substrate or even the sample holder. This fact dominantly affects κ as it describes the absorption of the total epilayer/substrate/holder stack in this spectral range.

Chemical and optical information is gained close to and above the band gap. The energy position provides information on the composition. Disorder and impurities result in an Urbach tail in absorption and thus significant deviations of κ from zero below the

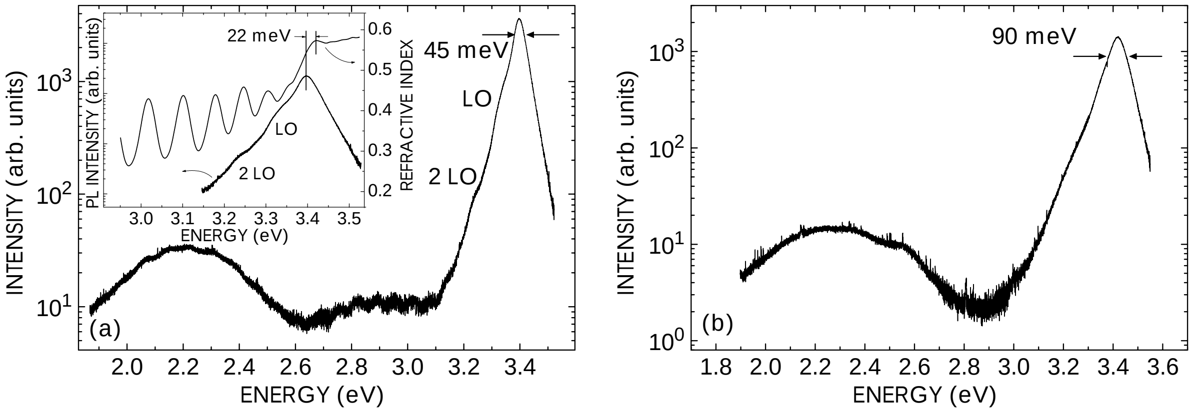

Figure 5.7: PL spectra at 300 K of (a) GaN(0001)/6H-SiC(0001) and (b) GaN($1\bar{1}00$)/γ-LiAlO $_2$(100) epilayers at excitation densities of 0.1 W cm^{-2}. Note the red-shift of 22 meV of the emission (PL) relative to absorption (SE) in the inset.

band gap. Above the band gap, absorption due to free carrier and the exciton continuum sets in. Directly at the band gap, absorption is enhanced by the excitonic resonance. The broadening of this excitonic resonance is determined by disorder present in the samples. The GaN(0001) sample exhibits this excitonic absorption feature at 3.42 eV and is thus of higher optical quality than the GaN($1\bar{1}00$) sample. Bearing in mind the exciton binding energy of 25 meV, the band gap is red-shifted by 15 meV which originates from the 0.15% tensile strain induced by the thermal mismatch to the SiC substrate [Eq. (2.11)].

PL at 300 K Spectra of GaN(0001) and GaN($1\bar{1}00$) samples at room temperatures are given in Fig. 5.7. For the GaN(0001) sample in (a) emission is observed at 3.40 eV (45 meV width) whereas the GaN($1\bar{1}00$) sample emits at 3.42 eV (90 meV width). The difference of 20 meV in transition energies is related to the different strain states in these samples. The GaN layers are under different strain states due to the different thermal expansion coefficients of the SiC(0001) and γ-LiAlO$_2$(100) substrates. In fact, the strains as determined from the PL peak positions [Eq. (2.11)] are in excellent agreement with the strains determined by XRD and Raman experiments.

For the GaN(0001) sample, the emission is excitonic. The inset in Fig. 5.7(a) shows both the PL and the imaginary part κ of the refractive index. The emission peak is red-shifted by 22 meV with respect to excitonic resonance in κ. The latter is proportional to the absorption coefficient $\alpha = E\kappa/(\hbar c)$ with the photon energy E. The red-shift is in excellent agreement with the van Roosbroeck-Shockley equation

$$R_{sp}(\hbar\omega) = \frac{8\pi n^2}{h^3 c^2} \frac{(\hbar\omega)^2}{\exp\left(\frac{\hbar\omega - \Delta E_F}{kT}\right) - 1} \alpha(\hbar\omega) \tag{5.2}$$

which relates the absorption $\alpha(\hbar\omega)$ to the spontaneous emission $R_{sp}(\hbar\omega)$ for photon energies $E = \hbar\omega$. The emission is the product of the Lorentzian shaped absorption with the Boltzmann tail of the Fermi distribution. This yields an emission peak which is red-shifted by about kT (25 meV at 300 K) with respect to the absorption peak.

A similar peak occurs for the LO-phonon replica [denoted by 'LO' in Fig. 5.7(a)] at the lower energy side of the PL emission. The observed separation of 60 meV is in

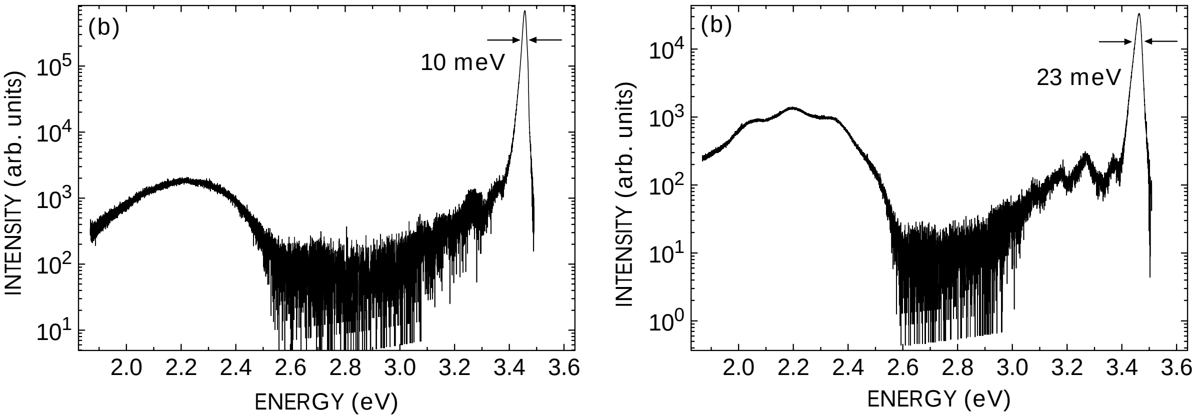

Figure 5.8: PL spectra at 5 K of (a) GaN(0001) / 6H-SiC(0001) and (b) GaN($1\bar{1}00$) / γ-LiAlO $_2$(100) epilayers at excitation densities of 0.1 W cm^{-2}.

agreement with Eq. (5.2) when using an LO-phonon energy of 92 meV.

The broad band emission around 2.2 eV is almost always observed in GaN and is called the ’yellow luminescence’ (YL) as it results in a yellowish visual impression. This emission is defect related as it is easily saturated with increasing excitation density. The origin of the YL is still controversially discussed in the literature. At present, it is believed that the involved transition involves a shallow donor and a Ga vacancy. [106] This belief is reasonable for two reasons. First, as-grown GaN always has a n-type background concentrations due to impurities such as Si and O which act as shallow donors. Second, the Ga vacancy is reported to be the most favorable intrinsic point defect in n-type GaN. [107] It is observed that the material at dislocations correspond to regions with enhanced YL. [108] While dislocations are reported to be electrically inactive, [109] the local strain field near a dislocation attracts intrinsic and extrinsic point defects (Cotrell atmosphere) [110] which are responsible for the enhanced YL.

PL at 5 K Spectra of GaN(0001) and GaN($1\bar{1}00$) samples at 5 K are shown in Fig. 5.8. The GaN(0001) sample emits at 3.455 eV (10 meV width) whereas the GaN($1\bar{1}00$) sample peaks at 3.47 eV (23 meV width). The blue-shift of 50 meV with respect to the 300 K measurements agrees well with the change in band gap between these temperatures. However, the emission does no longer stem from free excitons. Instead, excitons are bound to impurities, most likely to a neutral donor because of the n-type background carrier concentration. According to Haynes rule the exciton binding energies are around 10 to 20% of the impurity binding energy which is approximately 30 meV for hydrogen-like donors. This implies a exciton binding energy around 5 meV which is large enough for localization at 5 K.

Apart from the defect related YL, a weak donor-acceptor pair recombination is detected around 200 meV below the GaN band gap in agreement with the sum of donor and acceptor binding energies (see above).

Quantum efficiency and comparison with other growth methods The integrated spectral intensities of GaN(0001) and GaN($1\bar{1}00$) are about equal demonstrating that the quantum efficiency of these samples are very similar, despite the rather different defect densities and types present as determined from XRCs. The different defect densities, however, result in substantially broader emission from the GaN($1\bar{1}00$) samples.

The set-up used here cannot measure the photoluminescence intensity in absolute units. Thus, we can only compare quantum efficiencies of the samples grown by PAMBE presented here with the samples investigated in the same set-up under the same conditions. These samples are the GaN films already used in the database for GaN(0001) nucleation optimization. It is found that the quantum efficiencies of the best samples are comparable although they are grown by different growth techniques. However, the linewidths of the samples grown with PAMBE are still larger than those of MOVPE grown samples which exhibit values around 35 meV and 5 meV at 300 K and 5 K, respectively. The low-temperature linewidth is very sensitive to disorder present in the GaN layer. Consequently, we conclude that the degree of disorder is larger in MBE grown samples than in their MOVPE counterparts. This finding is probably due to the lower total density of point defects in the high-temperature MOVPE grown GaN films.

One may expect that lowering the substrate temperature from 750°C to 700°C to achieve smoother growth fronts has a detrimental effect on the photoluminescence properties of the samples as the density of point defects may increase. However, we did not observe significantly smaller photoluminescence intensities or larger linewidths during structural optimization of the buffer layer.

5.5 Capacitance-voltage profiling and Hall measurements

Control of the carrier concentration is vital for many semiconductor devices. A (light-emitting) diode requires a well-defined pn-junction for operation whereas a field-effect transistor cannot operate in the presence of parasitic parallel channels.

The background carrier concentration is measured both by capacitance-voltage (CV) profiling and Hall-effect measurements. In the case of CV profiling, a dc voltage is applied to the sample via a Hg probe thus altering the surface depletion depth. The local carrier concentration at the depletion depth is determined by adding a small ac voltage to the dc voltage. Hence, a depth profile of the carrier concentration is obtained. For typical carrier concentrations of $n=10^{17}$ cm^{-3} the depletion depth is around 100 nm. Hence, CV profiling is sensitive to the local carrier concentration close to the sample surface. In contrast, Hall-measurements yield the total free carrier concentration *averaged* over the total sample thickness. Thus, the use of semi-insulating substrates is necessary in order avoid parasitic conductance in the substrate. Here, the van-der-Pauw geometry is employed with In as ohmic contacts.

Poor agreement of CV and Hall measurements is found. While the CV measurements yield carrier concentrations down to the low 10^{16} cm^{-3} range, the Hall measurements return carrier concentrations around 10^{18} cm^{-3} and mobilities of 90 $\mathrm{cm}^2/\mathrm{Vs}$ almost independent of growth conditions. This discrepancy is explained by secondary ion mass spectrometry (SIMS).[*] Figure 5.9(a) shows the Si depth profile for a GaN layer grown on SiC. The Si concentration only gradually decreases from the SiC substrate

---

[*] In SIMS, the sample is bombarded in vacuum by a beam of primary ions having typical energies around 10 keV. As a result, particles are sputtered from the sample surface, some of which are in the form of secondary ions. By monitoring the intensity as a function of time a depth profile of individual atomic species is obtained.

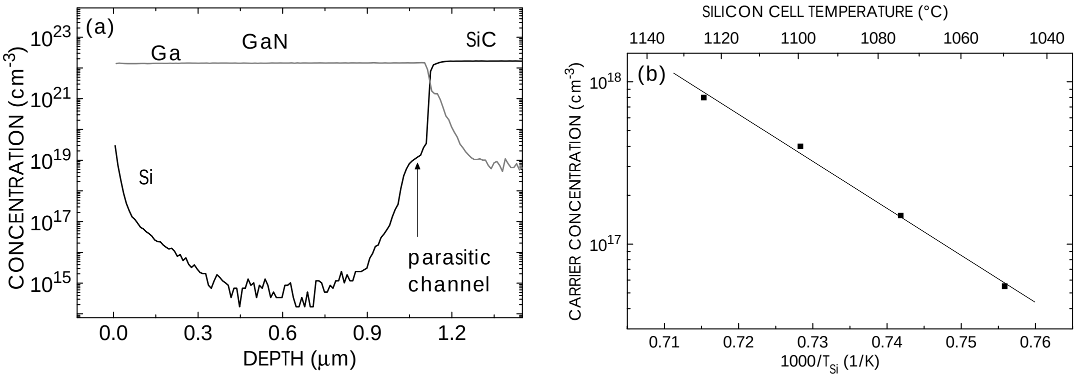

Figure 5.9: (a) SIMS depth profile of the Si and Ga concentration of a 1.1 μm thick GaN(0001) epilayer grown on SiC. Note the significant increase of the Si concentration to around 10^{19} cm^{-3} close to the GaN / SiC interface. The spurious increase in Si close to the sample surface results from surface contamination. (b) Arrhenius plot of the carrier concentration from CV profiling of 1 μm thick GaN(0001) films vs Si cell temperature. The solid line corresponds to a fit with a Boltzmann function (E=2.5 eV).

into the GaN epilayer. This excess Si originates from the fractional monolayer of Si which exists on the substrate surface before growth. [73] Si acts as a shallow donor in GaN, hence, a heavily ($\approx 10^{18}$ cm^{-3}) n-type doped layer is formed close to the substrate interface. The Hall measurement integrates over the total sample thickness. The measured mobility thus corresponds mainly to this highly doped layer. [111] In contrast, CV profiling is insensitive to this layer and is therefore used here to determine the actual carrier concentration.

These results have two important consequences. First, the n-type doping level can be controlled over a wide range of values which is important for the successful realization of the n-type region of a diode. Second, a low n-type background is required in order to enable generation of free holes. Acceptors in GaN such as Be and Mg suffer from the large activation energy around 150 meV and the difficulties in incorporating them into the GaN matrix. Here, the background carrier concentration of nominally undoped GaN is sufficiently low for the successful p-type doping which is required for realization of bipolar devices like light-emitting diodes.

The results of this and the previous Chapter constitute a firm base for the reproducible growth of GaN buffer layers. In the following Chapters, heterostructures grown on these buffer layers are investigated. We will start with GaN / (Al,Ga)N MQWs as these structures are free of compositional fluctuations.

6 GaN/(Al,Ga)N multiple quantum wells and the role of crystal orientation on emission

This Chapter treats GaN/(Al,Ga)N multiple quantum wells (MQWs) grown on GaN(0001) and GaN($1\bar{1}00$) buffer layers. First, we investigate growth and structural properties of (Al,Ga)N epilayers and of GaN/(Al,Ga)N heterostructures. Second, the impact of different crystal orientations on radiative recombination in GaN/(Al,Ga)N MQWs is demonstrated for the first time. Experimental evidence is given that M-plane oriented wells are free of internal electrostatic fields. Third, the in-plane polarization of the emission from these structures is studied. The results are in excellent qualitative and quantitative agreement with theoretical predictions.

6.1 Growth and structural investigation of GaN/(Al,Ga)N heterostructures

In this section, we examine both thick (Al,Ga)N layers and GaN/(Al,Ga)N MQWs. It will be shown that the (Al,Ga)N solid phase composition directly follows the gas phase composition. Then, it is demonstrated that the structural parameters of GaN/(Al,Ga)N MQWs are accurately determined using XRD.

Solid phase versus gas phase We investigate the dependence of the Al content of the (Al,Ga)N solid phase on the Al content in the gas phase. For this purpose, four 500 nm thick (Al,Ga)N layers are deposited directly on SiC(0001). Except for the Al flux, the samples are synthesized under identical conditions at a substrate temperature of 700°C. The Al content x_s in the (Al,Ga)N solid phase is determined by XRD analogous to the procedure given in chapter 3. The Al content $x_g = \Phi_{Al}/(\Phi_{Al} + \Phi_{Ga})$ in the gas phase is given by the individual beam fluxes Φ_{Ga} and Φ_{Al} of Ga and Al, respectively. These fluxes are determined from RHEED intensity oscillations of GaAs and AlAs grown on GaAs(001) substrates employing the same effusion cells in the same MBE system.

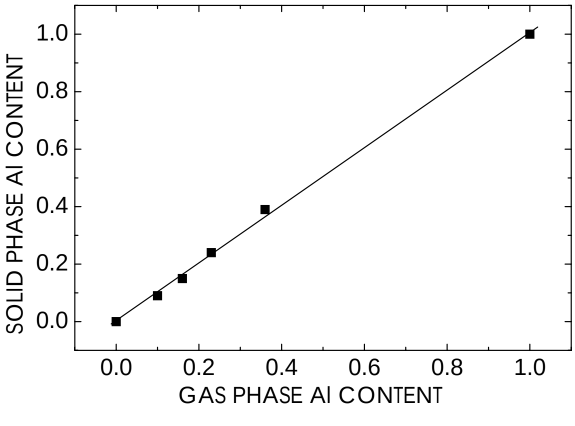

Figure 6.1: Al content of 500 nm thick (Al,Ga)N layers versus the Al content of the gas phase. The former is measured by XRCs, the latter is determined RHEED intensity oscillations of GaAs and AlAs. The solid line represents equal solid and gas phase Al contents.

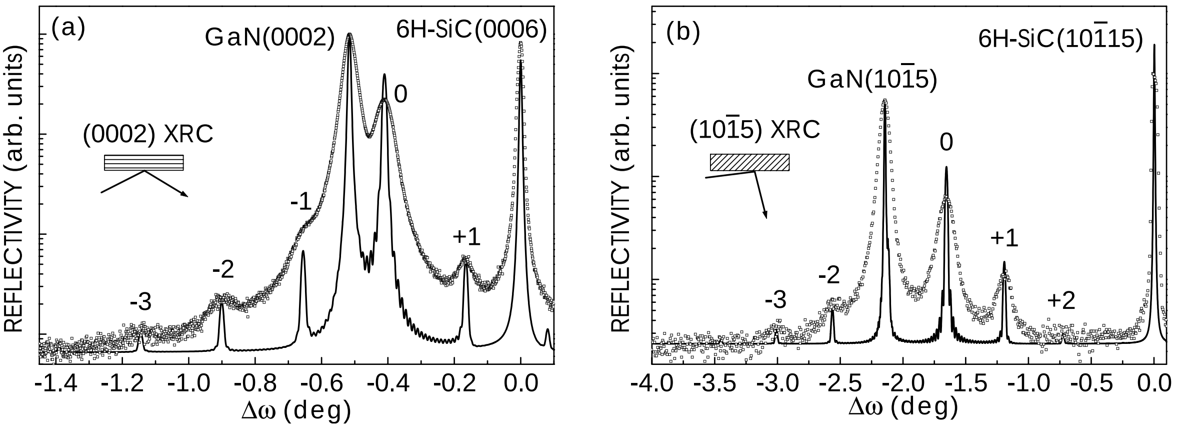

Figure 6.2: Experimental (circles) and simulated (solid line) XRCs across (a) the symmetrical (0002) and (b) the asymmetrical (10$\bar{1}$5) reflection with glancing incidence of a 20 period GaN / (Al,Ga)N MQW grown on GaN(0001) / SiC(0001). Satellites of $\pm n^{\mathrm{th}}$ order are denoted '$\pm n$'.

Figure 6.1 shows the Al content of the (Al,Ga)N solid phase for these four samples as a function of the corresponding gas phase Al content. The graph also contains the boundary conditions ($x_g = 0$, $x_s = 0$) and ($x_g = 1$, $x_s = 1$). A linear relation of solid and gas phase Al content with a slope of unity is obtained. This finding evidences that the solid phase composition of (Al,Ga)N layers grown at 700°C is equal to the corresponding gas phase composition. Hence, segregation of either Ga or Al, if any, is negligible. However, at significantly higher substrate temperatures, Ga desorption occurs, leading to a higher Al content in the solid phase than in the gas phase.

GaN/(Al,Ga)N MQWs The growth direction has a substantial impact on the formation of electrostatic fields in wurtzite nitride heterostructures [Chapter 2]. In particular, C-plane quantum wells are subject to large fields whereas M-plane quantum wells are predicted to be free of these fields. GaN / (Al,Ga)N MQW represent an ideally suited model system to study internal electrostatic fields as reported by several authors. [17–20] However, all of these reports are exclusively based on variations in thicknesses and / or composition of C-plane MQWs. The availability of GaN(1$\bar{1}$00) adds a new degree of freedom which we exploit here by comparing identically designed GaN / (Al,Ga)N MQWs in both the C-plane and the M-plane orientation.

The samples are grown under metal-stable conditions at a substrate temperature of 700°C for maintaining a smooth growth front. In the next paragraphs, it will be outlined how the individual thicknesses and compositions of MQWs are extracted from x-ray rocking curves (XRCs). Symmetric and asymmetric scans are performed. The latter is carried out in glancing incidence and steep exit since the superlattice peaks have a larger angular spacing for glancing incidence [47] and are thus more accurately resolved. The algorithm for extracting structural parameters is analogous for C-plane and M-plane wells and will therefore be discussed only for the former orientation.

Figure 6.2 displays scans around the symmetric (0002) reflection and the asymmetric (10$\bar{1}$5) reflection of a (0001) oriented sample together with simulations based on dynamical diffraction theory. Satellite peaks up to third order are visible in both geometries. The peak widths of GaN(0001) buffer and satellite peaks are comparable demonstrating the absence of additional dislocations in the MQW. This finding indicates a coherently grown superlattice.

Direct kinematical analysis Determination of the period P of the MQW is, in principle, identical to the determination of lattice constants. Both the MQW and the crystal exhibit a periodic structure along the growth direction. An exact analytic expression for P can only be given for symmetric reflections. In this geometry, P is calculated from the absolute angular positions θ_n of satellites of n^th order by

$$P = \frac{\lambda}{2\left(\sin\theta_{\mathrm{n}+1} - \sin\theta_\mathrm{n}\right)} \tag{6.1}$$

where λ is the x-ray wavelength. This expression follows directly from Bragg's law and is used throughout in the present work.

The average in-plane and out-of-plane lattice constants $\overline{a}$, and, respectively $\overline{c}$ of the MQW stack are calculated from the positions of the zeroth order satellite peaks. This procedure is analogous to the algorithm for a single layer which is discussed in chapter 3. The lattice constants a_GaN and c_GaN of the GaN buffer are determined in the same way. In the present case, we find $a_\mathrm{GaN} = \overline{a}$. This finding evidences a coherently grown MQW. Finally, we determine the average Al content $\overline{x}$ of the superlattice similarly to the case of epilayer as discussed in Chapter 3.

It is important to note that up to this point no assumptions about the actual composition depth profile are made. It is generally supposed that abrupt metallurgical interfaces are formed at the intented positions (i. e., segregation is absent). Below it will be demonstrated that this supposition is well-justified for GaN / (Al,Ga)N MQWs. The Al content x of the barriers and the individual thicknesses d_GaN of wells and d_AlGaN of barriers are calculated from the deposition times t_AlGaN for (Al,Ga)N and t_GaN for GaN. Starting point are the equations

$$x = \frac{\Gamma_\mathrm{GaN}}{\alpha\Gamma_\mathrm{GaN} + \Gamma_\mathrm{AlN}}, \qquad \overline{x} = \frac{x\, d_\mathrm{AlGaN}}{P}, \qquad P = t_\mathrm{AlGaN}\left(\Gamma_\mathrm{GaN} + \Gamma_\mathrm{AlN}\right) + t_\mathrm{GaN}\,\Gamma_\mathrm{GaN} \tag{6.2}$$

with the growth rates Γ_AlN and Γ_GaN (in units of length per time) for pure AlN and GaN, respectively. α denotes the ratio $V_\mathrm{ALN}/V_\mathrm{GaN}$ of the unit cell volumes of GaN and AlN. Using these expressions one can solve for the Al content x of the (Al,Ga)N barriers:

$$x = \overline{x}\left[1 + \gamma\frac{1-x}{1-x(1-\alpha)}\right] \tag{6.3}$$

$$\Rightarrow \quad x = \left(\frac{\overline{x}}{2} - \frac{1+\gamma\overline{x}}{2(\alpha-1)}\right)\left[1 - \sqrt{1 + \frac{4\overline{x}(1+\gamma)(\alpha-1)}{[1+\overline{x}\gamma+\overline{x}(1-\alpha)]^2}}\right] \tag{6.4}$$

where $\gamma = t_\mathrm{GaN}/t_\mathrm{AlGaN}$. Usually, the deviation of α from unity is neglected resulting in the expression

$$x = \overline{x}\frac{1+\gamma}{1+\gamma\overline{x}} \tag{6.5}$$

The error of this approximation is below one percent in most circumstances such as, e.g., GaN / (Al,Ga)N MQWs. The individual thicknesses of barriers and wells readily follow from the expressions

$$d_\mathrm{AlGaN} = \frac{\overline{x}}{x}P \quad d_\mathrm{GaN} = \left(1 - \frac{\overline{x}}{x}\right)P \tag{6.6}$$

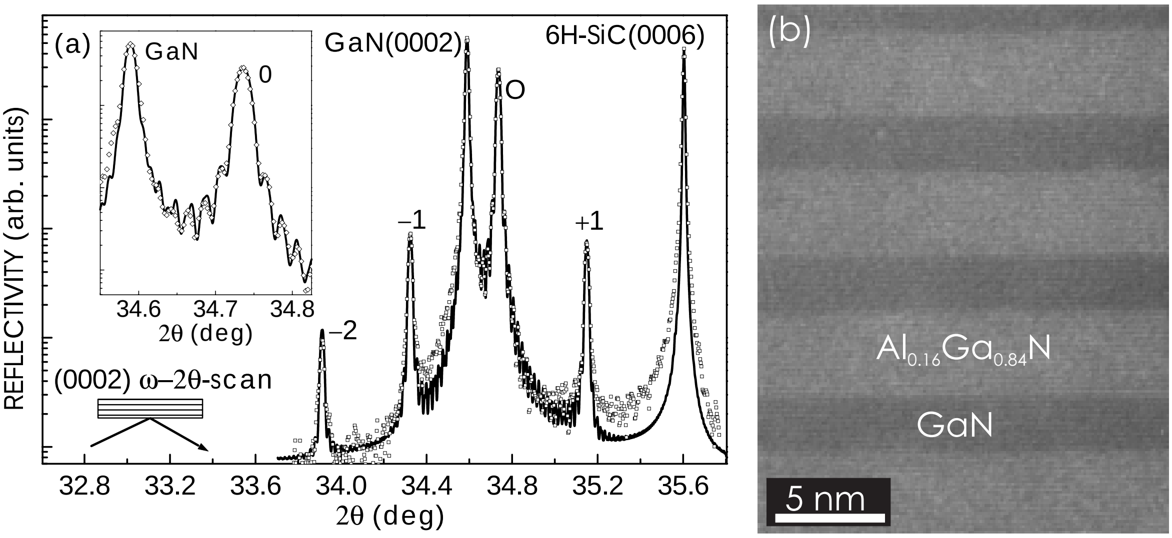

Figure 6.3: Investigations of the interface quality of GaN / (Al,Ga)N superlattices. (a) High resolution θ-2θ XRD scans in conjunction with dynamical simulation (open squares: experiment, solid line: dynamical simulation). Satellites of $\pm n^{\text{th}}$ order are denoted '$\pm n$'. The inset shows a magnified portion around the zeroth order satellite peak. (b) HREM image along the [11$\bar{2}$0] azimuth.

for the thickness of the (Al,Ga)N barriers. In principle, one should also incorporate the dependence of α on the Al content x in these equations. Then, however, analytical expressions do not exist any more such that a numerical analysis has to be performed. A more elegant method is provided by an indirect analysis of the peak positions via dynamical simulation of the diffraction profiles.

In the present case, we obtain thicknesses of 4.25 nm and 15.25 nm for well and barrier, respectively. The Al content of the barrier is found to be 14.5%. This set of parameters is also used for the dynamic simulation in Fig. 6.2. Good agreement of the peak positions of data and simulation is found for both geometries.

Up to this point, only XRCs have been employed for structural investigation. However, additional high-resolution θ-2θ scans should be performed for the following reasons. First, the accurate determination of layers thicknesses from XRCs, as done above, suffers from the considerable broadening of all reflections. Second, it has to be noted in this context that the satellite *peak positions* only reflect $\overline{x}$ and P. Any set of parameters (x, d_{GaN}, d_{AlGaN}) yielding the same set ($\overline{x}$, P) will result in perfect agreement of simulated and measured peak positions. In contrast, only a unique set (x, d_{GaN}, d_{AlGaN}) will also lead to agreement of the high-resolution θ-2θ scan *peak intensities*. Third, the interfacial quality of the structure remains undetected in XRCs, as any broadening induced by interface roughness is small compared to the mosaicity of the structure. We thus resort to high resolution θ-2θ scans for examining the geometric perfection of these periodic structures.

Figure 6.3(a) displays a high-resolution $\theta - 2\theta$ scan around the symmetric GaN(0002) reflection of a different GaN / (Al,Ga)N sample. The kinematical analysis of XRCs of this structure reveals a coherently grown superlattice ($a_{\text{GaN}} = \overline{a}$) with well and barrier thicknesses of 7.02 nm and 14.83 nm, respectively, and an Al content of 12.1%.

We now compare experimental and simulated peak intensities. The broadening of the GaN(0002) epilayer peak in $q_{\|}$ direction (typically around 150 arcsec) is larger than that of the substrate (around 30 arcsec) due to the presence of screw type dislocations (see the last Chapter). However, the simulation assumes that the crystal is free of imperfections. Thus, we have to normalize the simulation to the GaN(0002) reflection if we want to compare experimental and theoretical peak intensities of the superlattice. We find excellent agreement of the experimental and simulated peak widths and intensities. This finding evidences an accurate determination of the structural MQW parameters. In particular, segregation of Al or Ga, if any, is indeed negligible in these structures.

The inset in (a) shows a magnified portion of the profile around the zeroth order satellite peak. Clear interference fringes are seen in the experiment with only little damping compared to the ideal case represented by the simulation. This observation demonstrates the very high crystal perfection along the growth direction with sharp and abrupt interfaces and homogeneous barrier material.

Cross-sectional HREM We now investigate the configuration of the MQW interfaces in real space on an atomic scale. Cross-sectional high-resolution transmission electron microscopy (HREM) is ideally suited for such an experiment as it exhibits a spatial resolution better than typical atomic separations. Furthermore, HREM delivers local information and is thus complementary to x-ray diffraction which integrates over a large spatial scale.

Smooth and well-defined GaN / (Al,Ga)N interfaces are seen in the cross-sectional HREM image [Fig. 6.3(b)]. Furthermore, no disorder can be detected in the (Al,Ga)N barriers. These microscopic results are in perfect agreement with the conclusions drawn from macroscopic x-ray diffraction and confirm to the high structural perfection of these samples.

6.2 Role of crystal orientation on emission from GaN/(Al,Ga)N MQWs

In this section, we investigate the recombination from identically designed C-plane and M-plane quantum wells.

Band diagrams of identically designed C-plane and M-plane MQWs GaN / (Al,Ga)N MQWs having 15 periods are grown coherently on GaN(0001) and GaN($1\bar{1}00$) buffer layers. The samples are grown under nominally identical growth conditions. The MQWs consist of 5 nm wide GaN wells embedded in 10 nm wide $Al_{0.1}Ga_{0.9}N$ barriers as confirmed by high-resolution XRD.

Band diagrams of these samples at 5 K are calculated by self-consistent simultaneous solutions of the Poisson and Schrödinger equations in the effective mass approximation. Recent sources taken for the materials parameters of GaN and $Al_{0.1}Ga_{0.9}N$ (Tab. 6.1) are used in these calculations for a reliable comparison of experiment and simulation. The effective masses of $Al_{0.1}Ga_{0.9}N$ are linearly interpolated between GaN and AlN. The band gap of $Al_{0.1}Ga_{0.9}N$ takes into account both the tensile strain and a bowing parameter of 1 eV. [105] The GaN / AlN conduction band offset at the GaN / AlN is known to depend on the actual strain state of GaN and AlN. [26] For AlN coherently grown on relaxed GaN, a conduction band offset of 70% of the total band gap difference of GaN and AlN is reported [26, 112, 113] which is used here. The background doping

Table 6.1: Material parameters of GaN and AlN used for the self-consistent Poisson-Schrödinger calculations. ε_r denotes the relative dielectric constant. For (Al,Ga)N the linearly interpolated values of GaN and AlN are taken.

	m_e/m_0	m_h/m_0	ε_r	E_g (eV)
GaN	0.19	1	9.77	3.51
$Al_{0.1}Ga_{0.9}N$	0.20	1	9.65	3.66

level is set to 10^{17} cm^{-3} in both samples. The band diagrams are presented in Fig. 6.4. The C-plane wells [Fig. 6.4(a)] exhibit strong electrostatic fields of around 1 MV/cm resulting in a red-shift of 140 meV with respect to the field-free M-plane sample [Fig. 6.4(b)]. Furthermore, the electron-hole wavefunction overlap in the C-plane wells is strongly reduced compared to the M-plane wells.

Transition energies and decay times The structures under investigation are studied by cathodoluminescence (CL) and time-resolved PL (TRPL) in order to determine the transition energies and the decay times experimentally. All measurements are carried out at 5 K.

CL is carried out with an Oxford Mono CL 2. A high lateral resolution is achieved in the spot excitation mode (fixed position of the electron beam) which reduces the broadening on transitions due to lateral inhomogeneity of the wells. The kinetic energy of the exciting electron beam is kept at comparably low values of 5 keV in order to further minimize the excited sample volume to lateral dimensions below 100 nm. The electron current is 1 nA. The luminescence is collected by a lens, dispersed by a monochromator and collected by a nitrogen-cooled photomultiplier or a cooled CCD. The spectral resolution is better than 0.5 nm.

TRPL is performed using a frequency-tripled Ti:sapphire laser with an excitation energy of 4.89 eV, a pulse fluence of 1 nJ/cm^2 and a repetition rate of 76 MHz. The pulse width is around 400 fs. The luminescence is collected by a lens, dispersed by a 22 cm monochromator (600 lines/mm grating) and focussed onto the photocathode of a streak camera tube which is operated in synchroscan operation. The streak images

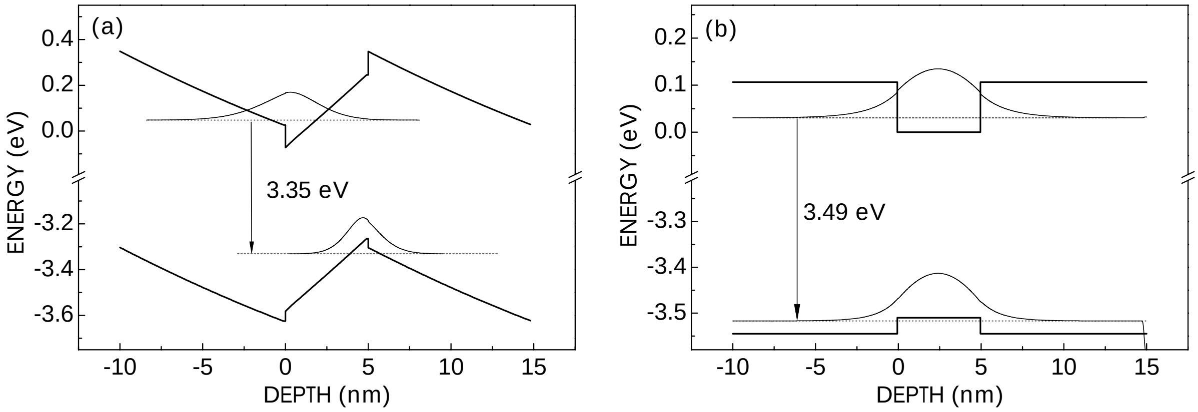

Figure 6.4: Calculated band profiles of (5 nm GaN)/(10 nm $Al_{0.1}Ga_{0.9}N$) MQWs grown along (a) [0001] and (b) [$1\bar{1}00$]. These profiles are obtained by self-consistent effective mass Schrödinger-Poisson calculations. The transition energies given take into account both strain and Coulomb interactions.

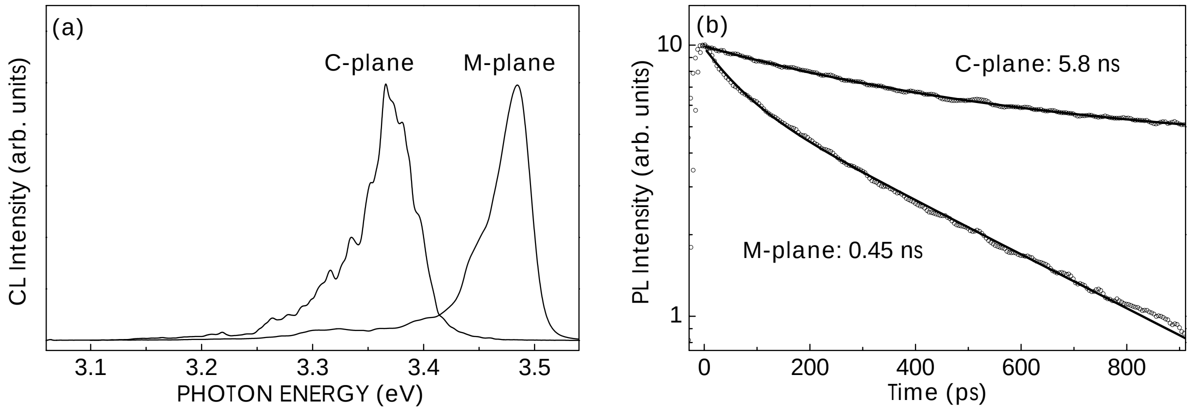

Figure 6.5: Impact of electrical polarization on the emission energy and decay time of (5 nm GaN)/(10 nm $Al_{0.1}Ga_{0.9}N$) MQWs. CL (a) and TRPL data (b) demonstrate a red-shift of the emission energy and prolonged decay times of C-plane wells with respect to M-plane wells.

are recorded by a cooled CCD array. The time-resolution of the set-up is better than 5 ps.

The results of these measurements are shown in Fig. 6.5. The transition energy for the C-plane oriented wells is around 3.36 eV whereas the wells grown on M-plane GaN emit at 3.48 eV [Fig. 6.5(a)]. The width of the CL bands of about 50 meV is likely to originate from well-width fluctuations and the presence of localized states induced by interface roughness. The spectra are modified by thickness interference fringes.

Taking into account the different thermal stresses after cooling (calibrated by the 300 K PL peak position of GaN buffer layers) we find that the C-plane wells emit 90 meV below the GaN(0001)/SiC(0001) band gap, while the M-plane wells emit 10 meV above the GaN($1\bar{1}00$)/γ-$LiAlO_2$(100) band gap. Both energies are in very satisfactory agreement with the self-consistent Schrödinger-Poisson calculations of Fig. 6.4. In particular, while the transition energy of the M-plane wells results solely from quantum confinement (flat-band conditions), we have to take into account the strong electrostatic fields present for the C-plane wells.

The impact of electric fields on the electron-hole wavefunction overlap is directly visible from the TRPL measurements at 5 K [Fig. 6.5(b)]. The striking difference between the decay times for M-plane (450 ps) and C-plane (5.8 ns) wells is a direct manifestation of the presence of electric fields in the C-plane wells. At this low temperature, we can safely assume that the measured decay time corresponds to the radiative lifetime. Depending on the (still poorly known) material parameters, we arrive at 10–100 times longer radiative lifetimes for the C-plane wells, which is in fair agreement with the experiment.

Lateral fields in M-plane wells It is important to discuss the impact of interface roughness [see the GaN($1\bar{1}00$) surface morphology in Fig. 5.1(b)] on the formation of lateral electrostatic fields in these M-plane oriented wells. At each step the polarization [0001] changes according to the in-plane direction of the step edge leading to maximized sheet charges (with density identical to the interface charges of [0001] oriented wells) for steps running normal to [0001] and no sheet charges for steps running parallel to [0001]. These sheet charges lead to lateral electrostatic fields. One can estimate the magnitude of these lateral fields by a simple geometric argument. The separation of steps normal to [0001] is more than one order of magnitude larger than the well width. In this case, the lateral field strength is determined by the sheet charge density at the step averaged over the well thickness. This averaged sheet charge density is under usual circumstances more than one order of magnitude smaller than the interface charge density in [0001] oriented well. The same argument applies to the lateral fields which can thus be safely neglected when compared to the vertical ones.

Quantum efficiencies at room temperature It has been shown above that at 5 K the radiative decay time of C-plane wells is larger than the radiative decay time of identically designed M-plane wells. At elevated temperatures, additional competing non-radiative recombination channels exist. These non-radiative recombination channels strongly affect the quantum efficiency. For a given non-radiative decay time, the quantum efficiency is approximately inversely proportional to the radiative decay time. This expectation is indeed observed in the present study. While strong emission is detected for the M-plane wells even at 300 K, the PL signal from the C-plane wells is extremely weak at this temperature. This finding is in perfect agreement with the report of Deguchi *et al.* using commercial LEDs produced by Nichia. [114]

In-plane polarization of spontaneous emission A strong polarization of the optical transitions is expected in M-plane oriented structures from the known valence band structure of wurtzite GaN. [115, 116] Bulk GaN has been reported to obey the theoretical predictions of an in-plane PL polarization of the M-plane. [117] For GaN(0001) films it is—in principle—possible to study the polarization anisotropy of the GaN($1\bar{1}00$) plane by investigating the edges of thick samples. This procedure requires considerably thick samples and thus fails for investigations of typical MQW structures where a reduction in polarization has been predicted by the finite thickness of the wells. [116] An ideal solution is therefore the use of M-plane MQW where the polarization anisotropy is easily accessible in back-scattering geometry.

PL measurements are carried out at 5 K under continuous wave excitation by the 334 nm (3.71 eV) line of an Ar^+ ion laser with an excitation density on the order of 10 W/cm^2. The PL polarization is analyzed using a UV polarization foil in front of a 2 m high-resolution spectrometer. The detecting system consists of a photomultiplier combined with a single photon counting unit. The experimental data are carefully corrected for the polarization dependence of the setup. The PL spectra are measured in back-scattering geometry, varying the analyzer angle ϕ from 0° to 180°. In the case of the M-plane sample, an angle of 90° is defined to be perpendicular to the [0001] axis.

Figure 6.6 displays the polarization-dependent low temperature PL spectra and the polarization degree of the samples. In both cases, we observe a single PL band in the spectral range recorded. The transition energy for the C-plane sample (a) is 3.40 eV whereas the M-plane sample (b) emits at 3.45 eV. While the transition energy of the M-plane sample is consistent with that expected for localized excitons in a wide GaN QW, the red-shifted emission of the C-plane sample is a consequence of the presence of strong electrostatic fields. [17] The larger width of the PL bands (about 80 meV) with respect to the CL spectra (see above) is most probably due to the larger spatial dimensions (around 100 μm) of the polarization dependent PL measurements. For the M-plane MQW, the extrema of the interference fringes are located at slightly different energy positions for different polarization angles, resulting from the different

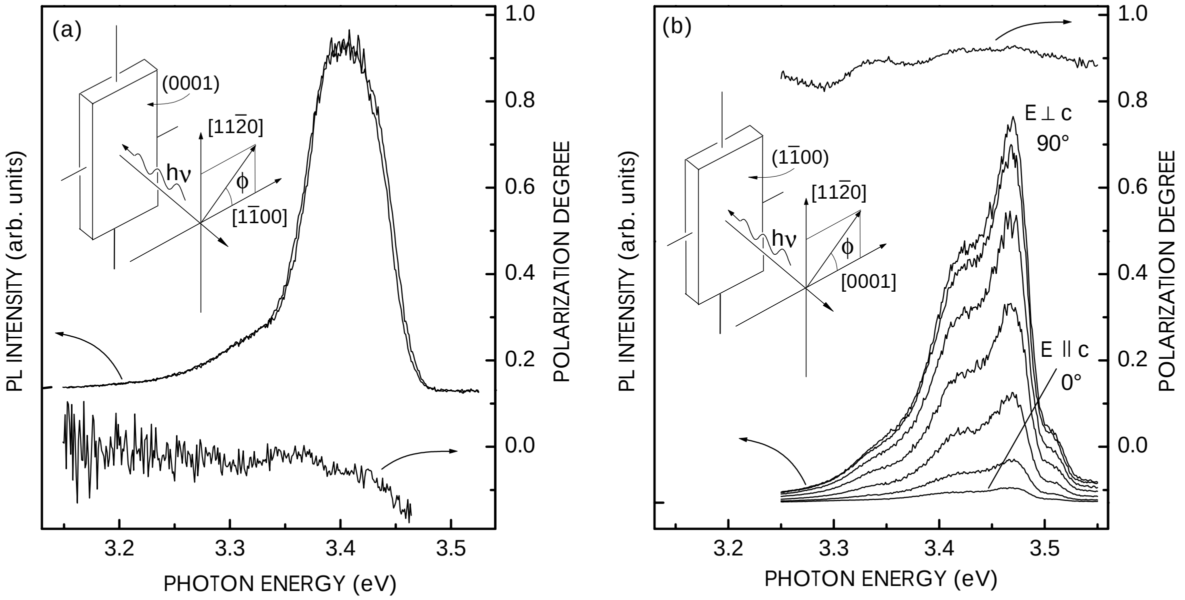

Figure 6.6: Polarization-dependent PL spectra and polarization degree of (a) [0001] and (b) [1$\bar{1}$00] MQWs at 5 K. The individual measurements of the [1$\bar{1}$00] sample are taken in steps of $\Delta\phi$=15°. The PL of the [0001] sample is umpolarized within the measurement accuracy. Thus, only two spectra, ϕ=0° and ϕ=90°, are shown in (a). The insets display a schematic sketch of the measurement geometry and sample orientation.

refractive indices for light polarized parallel and perpendicular to the [0001] axis. This interpretation is confirmed by reflectance spectroscopy (not shown here).

Care has been taken in these high-resolution measurements to avoid scattered laser light distorting the high-energy part of the spectra and thus influencing the polarization dependence. Obviously, the emission of the C-plane sample is unpolarized within the measurement accuracy of ±2%. In contrast, the emission of the M-plane sample is strongly polarized perpendicular to the *c*-axis. The polarization degree ρ, defined by

$$\rho = \frac{I_\perp - I_\parallel}{I_\perp + I_\parallel}, \tag{6.7}$$

is essentially independent of energy and amounts to about 90%. $I_\perp$ and $I_\parallel$ are the PL intensities polarized perpendicular and parallel to the c-axis, respectively. The weak modulation of the polarization degree is caused by the thickness interference fringes, mentioned above. For both samples, we do not detect any significant spectral shift of the PL when tuning the polarization angle.

To study the dependence of the emission intensity on polarization angle for the M-plane sample in more detail we plot the spectrally integrated PL intensity (Fig. 6.7), averaging over the interference effects. The $\sin(\phi)^2$-fit (solid line) agrees excellently with the experimental data (squares). This finding confirms the exact orientation of the [0001] axis in the growth plane.

The polarization of the spontaneous emission is determined by the interband dipole matrix elements, which in turn follow the selection rules arising from the valence band structure of wurtzite GaN. For the optical recombination of excitons, the discussion can be restricted to the Γ-point $(k = 0)$. Here, the A-exciton states (heavy hole) with a

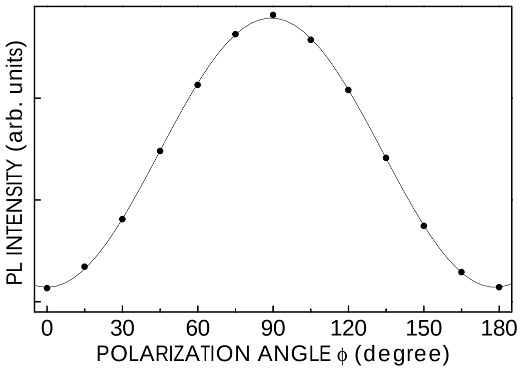

Figure 6.7: Spectrally integrated 5 K PL intensity of the $[1\bar{1}00]$ GaN/(Al,Ga)N MQW as a function of polarization angle ϕ. The $\sin(\phi)^2$-fit (solid line) agrees very well with the experimental data (squares). An angle of 90° describes the case of light polarized perpendicular to [0001].

projection $j_z = \pm\frac{3}{2}$ of the total angular momentum on the [0001] axis consist only of p_x and p_y orbitals and are totally σ polarized $(E \perp c)$ (x and y are chosen again along the $[11\bar{2}0]$ and $[1\bar{1}00]$ directions). For B- and C-excitons σ polarized transitions are comparable in intensity as transitions with π polarization $(E \parallel c)$ since the corresponding states are composed of all three p components.

For unstrained bulk GaN, the ground state is the A-exciton and a polarization degree of zero and of unity is expected detecting along and normal to the c-axis, respectively. As a characteristic feature of M-plane quantum wells, the confinement takes place perpendicular to the quantization axis of j_z (that is along y direction), leading to a weak mutual mixing of the different p-orbitals even at vanishing in-plane wave vector $(k_x, k_z) = 0$. Thus, a π polarized contribution is expected for the A-exciton in a M-plane quantum well. A quantitative analysis can be derived from the confinement-induced expectation value of the respective wave vector k_y. For the present well width and barrier heights, we estimate a value of 0.4 nm^{-1}, for which band structure calculations predict a 10% p_z orbital contribution to the A states. [116] This value is in excellent agreement with the polarization degree of 0.9 as observed in our experiments.

In principle, an additional weakening of the polarization selection rules can be expected from exciton localization as well as residual strain due to different thermal expansion of the GaN layers and the substrate. However, the localization in the well plane takes place on a characteristic length scale of about the exciton Bohr radius, where the broadening of the in-plane k-vector is too small to explain the observed deviation of ρ from unity. The same conclusion can be drawn for the strain effects comparing the experimentally estimated residual thermal strain with calculations. [118]

We emphasize, that the total width of the PL band is much larger than the valence band splitting. Since we did not observe any spectral shift in the PL spectra between $(E \perp c)$ and $(E \parallel c)$, we have to attribute the emission to a band of localized states, each of which only occupied with A-excitons. This implies a very fast thermalization compared to the exciton life time. Any occupation of B- and C-states leads to components $(E \parallel c)$ at higher PL energies as indeed observed on bulk GaN at elevated sample temperature. [117]

7 Synthesis of (In,Ga)N/GaN multiple quantum wells

In this Chapter, the growth of (In,Ga)N / GaN MQW structures is investigated. Massive In segregation is evidenced by RHEED, XRD, SIMS and PL and very good agreement of all of these techniques is achieved by careful data analysis. In particular, it is demonstrated that segregation critically influences the PL transition energy.

7.1 Critical issues for (In,Ga)N growth

In the last Chapter, the synthesis of GaN / (Al,Ga)N heterostructures has been studied. The most important results of these investigations are briefly outlined here. At 700°C, the (Al,Ga)N solid phase composition equals the gas phase composition, i.e., segregation of Ga or Al is negligible. Heterostructures with homogeneous (Al,Ga)N barriers as well as smooth and abrupt interfaces have been achieved. The structural parameters are accurately determined by a direct kinematical analysis of XRD profiles. Hence, growth and structural characterization of arbitrarily designed GaN / (Al,Ga)N heterostructures imposes no significant difficulties in agreement with the literature. [20, 119, 120]

In contrast, the grower has to pay attention to several phenomena for deposition of thick (In,Ga)N layers or (In,Ga)N / GaN MQWs. The most significant difficulties reported are summarized in the following. First, the formation enthalpies for InN and GaN are very different resulting in strong In surface segregation at the growth front. [121] The very few reports [121, 122] on the actual segregation mechanism of (In,Ga)N are restricted to the conclusion that the solid phase composition of (In,Ga)N may not follow the gas phase composition linearly. Second, the vapor pressure of InN is rather large compared to the vapor pressure of GaN resulting in low incorporation rates of In in the (In,Ga)N alloy. [123] Third, a miscibility gap is predicted on theoretical grounds for (In,Ga)N leading to spinodal decomposition. [124]

The generally accepted strategy to circumvent these issues is the use of relatively low growth temperatures (compared to GaN growth) and high V / III flux ratios (significantly greater than unity). [121, 122, 125] Both measures are reported to result in an improved In incorporation rate as both evaporation and segregation of In are substantially suppressed. The use of large V / III flux ratios for the growth of (In,Ga)N wells implies even larger V / III flux ratios during the GaN barrier growth. This surface stoichiometry is contradictory to the advised Ga-stable growth of GaN as discussed in Chapter 4. N-rich surface stoichiometries lead to a roughening of the GaN growth front.

The aim of this Chapter is therefore twofold. First, the impact of different surface stoichiometries on the synthesis of (In,Ga)N / GaN is investigated. Second, the actual segregation mechanism is examined.

In the present study, the (In,Ga)N / GaN MQWs are deposited at a substrate temperature of 580°C, a plasma power of up to 250 W and a N_2 flow of 0.7 sccm. Since the underlying GaN buffer is grown at a temperature of 700°C, a plasma power of 200 W and an N_2 flow of 0.15 sccm, a growth interruption is required for parameter adjustment. This interruption takes 10–20 min because the plasma source parameters must

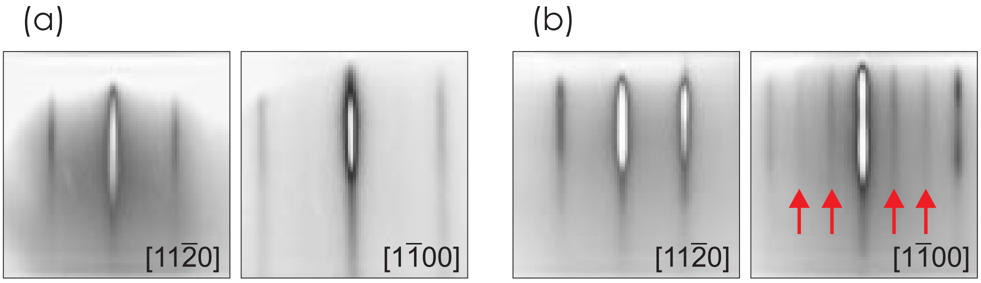

Figure 7.1: RHEED patterns of the growth front for (In,Ga)N / GaN deposition: (a) During (In,Ga)N deposition, a dim (1×1) pattern is observed. (b) During barrier deposition, the (1×1) pattern gradually transfers into a bright (1×3) reconstructed pattern.

be changed slowly in order to guarantee a stable plasma discharge. The interruption has an important consequence. It is demonstrated in Appendix A that the first well on the GaN buffer has a considerably larger transition energy than the other wells. The result is a high energy peak or shoulder of the main PL peak.

It is reasonable to relate the larger transition energy of the first well to free carrier screening of the electrostatic field due to a higher doping level. This higher doping level may be explained as follows. During growth interruption, the substrate surface is exposed to a significant gas flow from the plasma source even for closed nitrogen shutter. Consequently, also impurities of the N_2 source gas, such as O, accumulate at the substrate surface. During normal growth, these impurities lead to an n-type background concentration around 10^{17} cm^{-3} as determined by CV measurements. However, the accumulation of impurities leads to a considerably higher doping level of the first (In,Ga)N well which is directly grown after the interruption.

7.2 RHEED observations

In this section, the synthesis of (In,Ga)N / GaN MQWs is studied *in-situ* by RHEED. The observations are crucial for the remaining sections of this chapter. A careful investigation of the growth front enables a rapid evaluation of the deviation of the actual growth parameters from the ideal ones. We will start with a general discussion of the results and then study in detail two specific samples.

General observations During growth of an (In,Ga)N / GaN MQW a characteristic sequence of RHEED patterns is detected (Fig. 7.1). It will be shown in this Chapter that this sequence can be used to monitor In segregation *in-situ*. This observation paves the way towards rapid *in-situ* observation and optimization of growth.

A (1×1) pattern is observed during (In,Ga)N well deposition [Fig. 7.1(a)]. The intensity of the whole pattern rapidly decreases during this phase. After closing the In shutter, the overall RHEED intensity first remains constant but then increases until the transition to a threefold reconstruction pattern along the [1$\bar{1}$00] azimuth is observed [Fig. 7.1(b)] at a particular instant, denoted delay time τ_{RHEED}. Then, growth proceeds on this (1×3) reconstructed surface until the In shutter is opened again for the next (In,Ga)N well.

The decrease of the RHEED intensity is probably due to a build-up of a floating layer

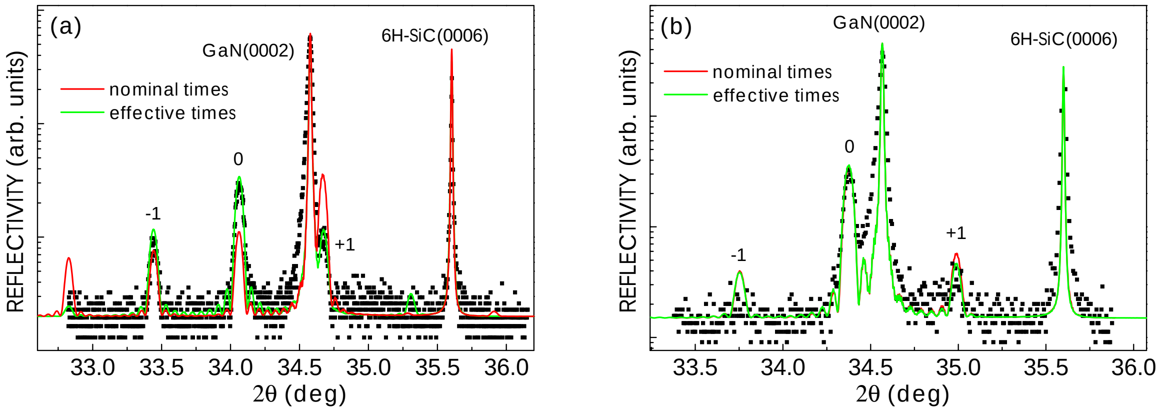

Figure 7.2: High-resolution XRD θ-2θ scans around the symmetric GaN(0002) reflection of (In,Ga)N / GaN MQWs. The wells are grown under (a) metal-stable and (b) N-stable flux conditions. The solid lines represent simulations based on dynamical diffraction theory. Satellite peaks of $\pm n^{\text{th}}$ order are labelled '$\pm n$'.

of In during well deposition via In surface segregation. After closing the In shutter, this layer of excess In is consumed by further growth despite the fact that only Ga and N fluxes are present. Consequently, the overall RHEED intensity increases again. The threefold reconstruction pattern then corresponds to a particular surface coverage of In, probably a third of a monolayer. However, for clarifying these assumptions we have to investigate the growth process in more detail.

Specific observations As mentioned above, it is known that larger V / III flux ratios suppress In segregation. In fact, we notice that larger V / III flux ratios result in systematically shorter delay times τ_{RHEED} and vice versa. For further studying this finding, we investigate two samples which are grown under identical conditions except for the In flux. These samples are grown on 1 μm thick GaN(0001) buffer layers with smooth buffer layer surfaces. The number of periods is 10 with nominal well and barrier deposition times of 8 s and 50 s, respectively. The individual In, Ga and N fluxes are chosen as follows. The GaN barriers are grown under N-stable conditions whereas the (In,Ga)N wells are deposited under either metal-stable or N-stable conditions. In detail, the In flux of the metal-stable grown wells is around 2.5 times the In flux of the nitrogen-stable grown wells.

During growth of these MQW samples, clear differences are observed in RHEED. For the metal-stable grown wells, the growth front remains two-dimensional and the delay time amounts to 30 s. In contrast, for N-stable grown wells the surface roughens in the course of the growth and the delay time is only 10 s.

7.3 Detection of In segregation by SIMS and XRD

The structural parameters of these two samples are investigated by high-resolution x-ray diffraction employing ω-2θ scans around the symmetric GaN(0002) reflection (Fig. 7.2). For both samples, satellite peaks up to first order are detected. The satellite positions allow for accurate determination of the MQW periods and average In contents analogous to the procedure described in the previous Chapter. Here, we find average

Table 7.1: Structural parameters of (In,Ga)N / GaN MQWs as determined by a kinematical analysis of high-resolution symmetrical XRD scans across the GaN(0002) reflection. 'Nominal times' correspond to the deposition times of 8 s and 50 s for well and barrier, respectively. The 'effective times' take into account segregation and are defined in the text.

times	metal-stable grown wells			N-stable grown wells		
	x (%)	d_{InGaN} (nm)	d_{GaN} (nm)	x (%)	d_{InGaN} (nm)	d_{GaN} (nm)
nominal	44	2.9	12.3	20	2.5	12.3
effective	15	8.6	6.6	10	4.9	9.9

In contents of 8.4% (3.4%) and periods of 15.2 nm (14.8 nm) for the metal-stable (N-stable) grown wells. The average In contents determined are in good agreement with the different In fluxes. The period of the sample with metal-stable grown wells is larger due to the larger amount of incorporated In. We have to remember in this context that the satellite peak positions do not give any clue as to the actual composition profile, i.e., the individual thicknesses and compositions of well and barrier. As already done in the last Chapter we perform a direct kinematical analysis of the diffraction profile and assume that Eqs. (6.2) are valid here as well. Table 7.1 lists these structural parameters which are denoted by 'nominal times'.

Failure of conventional kinematical analysis These parameters are then used as input for dynamical x-ray simulations. The profiles obtained are shown in Fig. 7.2 and labelled 'nominal times'. While experimental data and simulation are in fair agreement for the N-stable grown wells [Fig. 7.2(b)] a poor match of data and simulation is found for the metal-stable grown wells [Fig. 7.2(a)]. The experimental intensity is larger than the simulated intensity for the '+1' satellite while the opposite is true for the '-1' and '0' satellites. Hence, the direct kinematical analysis fails to return the correct structural parameters in this case.

The reason for this failure is In segregation. This effect leads to a deviation of the actual composition profile from the intended one. In particular, well widths and In content are larger and smaller than expected, respectively. In principle, the composition profile can have arbitrary shape depending on the actual segregation mechanism.

SIMS depth profiles A direct method for examining the composition profile is given by secondary ion mass spectrometry (SIMS). This technique yields the composition versus sputtered depth and is therefore able to accurately determine depth profiles of heterostructures. Great care is needed in order to obtain a sufficiently high depth resolution since the composition is averaged over the area of the sputtered crater. Here, the samples are examined using MCs^{+} ions having a kinetic energy of 5.5 keV. The ion beam current of 10 nA is focussed on a circle having a diameter of 500 μm. The depth resolution is about 5 nm / decade close to the sample surface but deteriorates with increasing depth due to crater roughness. The obtained depth profiles are shown in Fig. 7.3. The interface quality can at least qualitatively be estimated from the change of the In signal from well to barrier. Abrupt and sharp interfaces within the SIMS depth resolution are observed for the metal-stable grown wells with damping towards larger depths due to SIMS crater roughness. In contrast, for the N-stable grown sample, only the wells close to the GaN buffer layer are clearly resolved whereas towards the sample surface the In signal is strongly damped by interface roughness.

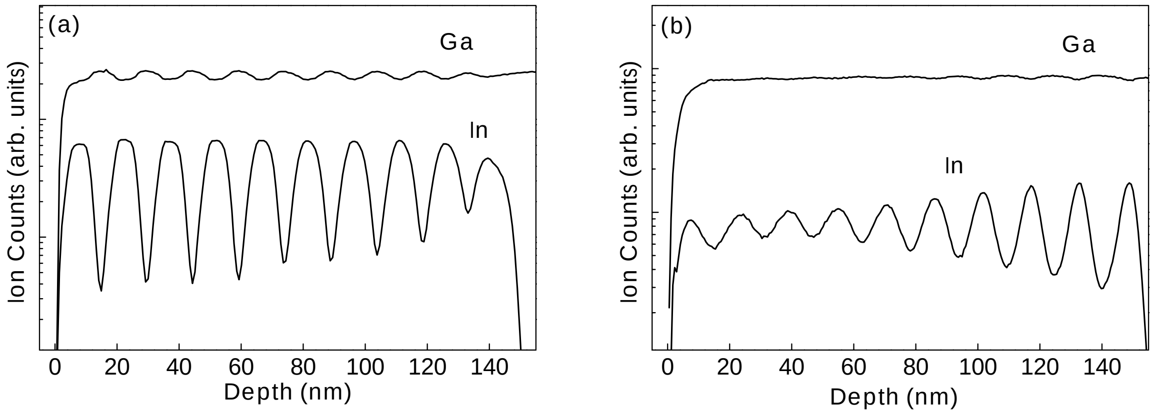

Figure 7.3: SIMS depth profiles of the (In,Ga)N / GaN MQW structures under investigation. Note the symmetrically shaped metal-stable grown (In,Ga)N wells in (a) with abrupt interfaces. In (b), interface roughness results in smeared out depth profiles of the N-stable grown wells.

The well width in SIMS is defined by the 1 / e width of the In signal. Here, we obtain 8.5 nm for the metal-stable grown wells. Massive In segregation is thus evidenced beyond any doubt. For the N-stable grown wells we can only estimate the well width to be around 4–5 nm, as an unambiguous width determination is not possible because the signal amplitude is too small for the top wells due to interface roughness. Furthermore, the wells close to the GaN buffer are also smeared out due to SIMS crater roughness. However, note that even this rough estimate of 4–5 nm agrees well with the structural parameters employing effective deposition times.

Segregation mechanism The composition profile of a single period is investigated in order to study the actual segregation mechanism. Usually, segregation is a first order process such that a constant fraction of the excess atomic species is incorporated as known for, e.g., In in (In,Ga)Sb. [126] This first order segregation mechanism results in an asymmetrically shaped composition profile with exponential leading and trailing edges. For the metal-stable grown wells the shape of the In profile is symmetric with an almost constant In content and leading and trailing edges of 5 nm / decade and 4 nm / decade, respectively. This finding is most clearly seen for the well closest to the surface as the SIMS crater roughness is lowest for this particular well. Such symmetric ’top-hat’ profiles with edges corresponding to the SIMS depth resolution evidence an In incorporation rate at the solubility limit—here around 15%—leading to constant In contents over the entire well width. This incorporation mechanism is analogous to segregation of Si in GaAs where also symmetric ’top-hat’ profiles were observed. [127] In the present case, incorporation of In does *not* depend on the actual amount of floating In on the sample surface but is thus a zeroth order process.

Effective deposition times The above SIMS results suggest a modification of the evaluation procedure of XRD profiles. This modification is based on the observation that the actual In profile still has a rectangular shape despite segregation. Hence, a modification of the deposition times is suited for describing the observed segregation process. The excess In acts as a reservoir during growth. Above it was proposed that the appearance of the threefold reconstruction corresponds to the moment at which all excess In is consumed. Hence, the deposition times are corrected taking into account In segregation via τ_{RHEED}. The effective deposition time $t_{\mathrm{eff,InGaN}}$ for the well is the sum of

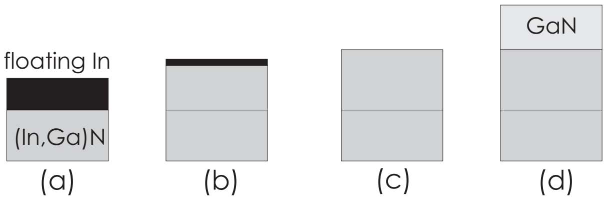

Figure 7.4: Model for the growth of (In,Ga)N / GaN MQWs. Deposition of one period is schematically depicted where the In shutter is open during (a) but closed during (b)-(d). The growth stages (a), (b), (c) and (d) are discussed in the text.

the nominal well deposition time t_{InGaN} and the delay time τ_{RHEED}. Analogously, the effective deposition time $t_{\mathrm{eff,GaN}}$ of the barrier is the difference of the nominal barrier deposition time t_{GaN} and the delay time τ_{RHEED}.

$$t_{\mathrm{eff,InGaN}} = t_{\mathrm{InGaN}} + \tau_{\mathrm{RHEED}} \qquad t_{\mathrm{eff,GaN}} = t_{\mathrm{GaN}} - \tau_{\mathrm{RHEED}} \tag{7.1}$$

Structural parameters based on a kinematical analysis utilizing these effective times are also given in Tab. 7.1. Strikingly, the well width is three times larger than that derived from nominal deposition times. Dynamical simulations employing these effective parameters are in excellent agreement with the experimental data (Fig. 7.2) after only minor adjustment of the effective times. This finding supports the use of effective deposition times for the kinematical analysis instead of the nominal times. The actual width of the metal-stable grown wells amounts to 8.5 nm instead of the nominal value of 2.9 nm. Consequently, the actual In content is not 44% but only 15%. In the case of the N-stable grown wells, the impact of segregation is smaller. Even the nominal deposition times result in structural parameters which lead to a fair agreement of simulation and measured data. Note that these results are in excellent agreement with the SIMS results.

The linewidth of the satellites contains information on the homogeneity of the sample. Therefore, we compare the experimental with the simulated linewidths for examining the crystal quality of the grown samples. The zeroth order satellite essentially reflects the homogeneity in composition. Here, we find sound agreement of data and simulation for both samples. In contrast, significant differences are observed for the first order satellites which basically detect the interface quality. The metal-stable grown wells exhibit linewidths in agreement with the simulation. Therefore, abrupt and sharp interfaces are present in this sample. However, the N-stable grown wells exhibit a significant broadening of the first order satellites with respect to the simulation reflecting rough interfaces. Both results are in agreement with the RHEED observations.

Model for (In,Ga)N/GaN MQW growth The RHEED, XRD and SIMS results can be consistently described by the model shown in Fig. 7.4. This model furthermore paves the way for growing MQWs with smooth interfaces and tailored wells widths. During nominal well deposition [Fig. 7.4(a)] not all incoming In is incorporated, and a floating layer of excess In is built up at the growth front by surface segregation. The surface is unreconstructed and a dim (1 × 1) RHEED pattern is observed. After closing the In shutter [Fig. 7.4(b)], the excess In is consumed, hence, the growing material is (In,Ga)N. Incorporation of In proceeds at the solubility limit leading to a homogeneous composition of the (In,Ga)N well. The RHEED pattern gains in intensity but the pattern is still (1 × 1). When all the excess In except a third of a monolayer is consumed [Fig. 7.4(c)], a

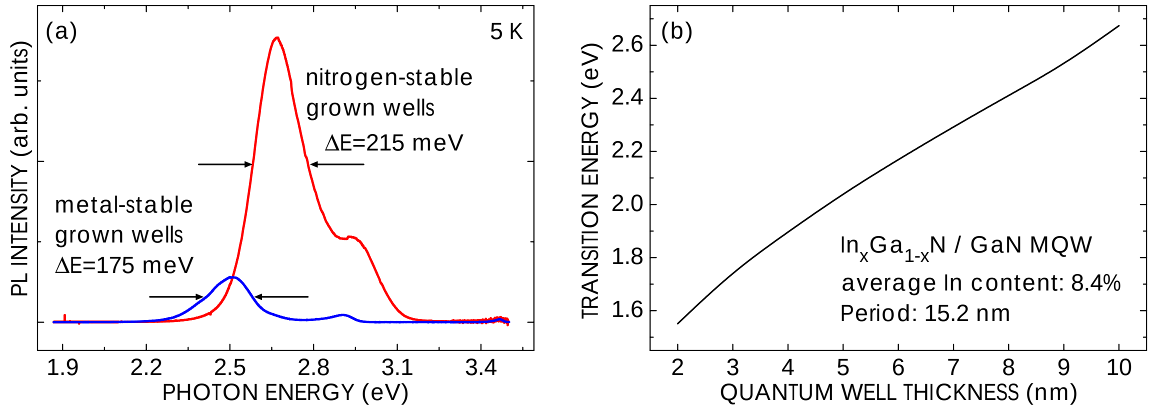

Figure 7.5: (a) PL spectra at 5 K of the two MQW samples under investigation. Note the significantly reduced quantum efficiency and linewidth of the metal-stable grown wells with respect to the N-stable grown wells. The shoulders at 3.0 eV originate from the well closest to the GaN buffer [Appendix A]. In (b), the calculated transition energy of metal-stable grown wells for different widths but identical average In content and period is presented.

threefold reconstruction appears along the $[1\bar{1}00]$ azimuth. During the following GaN barrier deposition [Fig. 7.4(d)], the growth front is under N-stable conditions until the In shutter is opened again for the next well. If this period is too long, then the surface roughens due to the N-stable GaN growth.

This model suggests lower and upper limits for the nominal barrier deposition time t_{GaN}. If t_{GaN} is too small, i.e., $t_{\mathrm{GaN}} < \tau_{\mathrm{RHEED}}$, then the excess In is not fully consumed and no GaN barrier is grown. On the other hand, if t_{GaN} is too long then the surface roughens. The optimum t_{GaN} will be in-between these two limits.

7.4 Impact of In segregation on photoluminescence

PL spectra at 5 K are shown in Fig. 7.5(a). Clear differences for the metal-stable and the N-stable grown wells are observed. The ratio of the PL intensity of the N-stable and the metal-stable grown wells is around 7. This finding is due to the larger spatial separation of electron and hole wavefunctions in the wider metal-stable grown wells resulting in an increase in radiative lifetime and consequently a reduction in quantum efficiency. At room temperature, this effect is even more pronounced since no signal from the metal-stable grown wells is detected. Furthermore, the low temperature PL linewidth is 175 meV for the smooth metal-stable grown wells, whereas a width of 215 meV is found for the rough N-stable grown wells. This result reflects an interface roughness broadening of the PL transitions for the N-stable grown wells, which have rather rough interfaces compared to the metal-stable grown wells.

Experimental versus theoretical transition energies We compare experimental and theoretical peak positions based on self-consistent Schrödinger-Poisson calculations in analogy to the last Chapter. Table 7.2 lists experimental and theoretical PL transition energies at 5 K.

For (In,Ga)N it is generally accepted that compositional fluctuations of the (In,Ga)N alloy result in carrier localization. Therefore, any comparison of experimental data with

Table 7.2: Experimental and theoretical PL transition energies (all values in eV) of the two (In,Ga)N / GaN MQW structures under investigation. Theoretical values are listed for the structural parameters deduced from both nominal and effective deposition times. A bowing parameter of 1.0 eV is used for the (In,Ga)N band gap.

	metal-stable grown wells	N-stable grown wells
experimental	2.50	2.66
nominal	1.69	2.79
effective	2.45	2.91

simulations relies on the knowledge of these localization depths. Of course, localization also takes place at morphological features and carriers are localized at well width fluctuations. The N-stable grown wells exhibit rather rough interfaces. This finding explains why the experimental transition energy (2.66 eV) in Tab. 7.2 for this sample is well below the calculated one (2.91 eV). One can investigate the well width fluctuations required for such a localization. Under the assumption of a homogeneous In content of 10% (Tab. 7.1) we obtain well width fluctuations around ±2 nm. In order to minimize the impact of well width fluctuations, we will concentrate in the following on the smooth, metal-stable grown wells. In the next Chapter, it will be demonstrated that the localization depths in metal-stable grown wells are well below 50 meV. Therefore, the direct comparison of transition energies is possible for these samples.

It is often claimed that the theoretical polarization fields are too large for (In,Ga)N. [128, 129] This statement is based on the apparent failure of the polarization fields calculated by Bernadini *et al.* [25] to predict transition energies which agree with the experimental data. In fact, many authors quote that they obtain better agreement if they use only half of the theoretical polarization fields. [128]

In fact, the nominal deposition times lead to grossly (more than 0.7 eV!) underestimated transition energies. Instead, if we use only half of the theoretical polarization charges we obtain a calculated energy of 2.46 eV in agreement with the experiment. At the same time, the values of Bernadini *et al.* are reported to be correct for GaN [20, 112] and (Al,Ga)N. [19, 20, 29, 119] Our insight into the impact of In segregation on the struc-

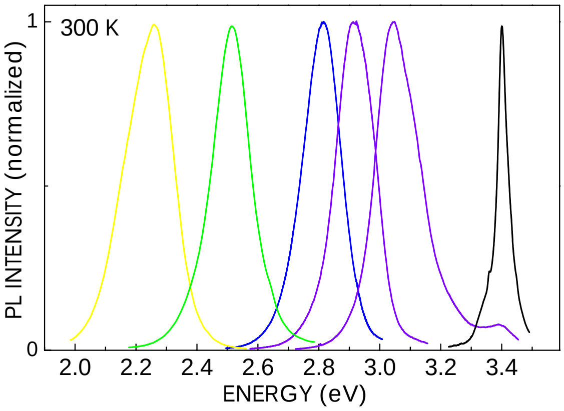

Figure 7.6: PL spectra at 300 K of (In,Ga)N / GaN MQWs. The growth parameters were systematically modified to obtain emission from the violet to the yellow spectral range with small linewidths and high 300 K quantum efficiency.

tural parameters of the sample unravels this apparent contradiction. Using the effective deposition times, the energy experimentally obtained is in excellent agreement with the calculated one [Tab. 7.2].

In Fig. 7.5(b) the dependence of the transition energy on the well width is depicted for fixed average In content and fixed period. The transition energy strongly depends on the actual well width and is thus a very sensitive indicator for In segregation. Hence, an accurate determination of structural parameters is necessary for a correct comparison of experiment and simulation.

Finally, a strategy for quantum wells having a high quantum efficiency and sharp emission is derived from the above results. Metal-stable growth conditions during well deposition yield abrupt interfaces leading to narrow linewidths. Control of the well thickness is achieved by taking into account In segregation. If this strategy is followed then the growth of (In,Ga)N / GaN MQWs exhibiting both narrow linewidths and high quantum efficiency at room temperature imposes no difficulties as seen from Fig. 7.6. The entire spectral range from ultraviolet to yellow has been covered by systematic adjustment of the growth parameters. Moreover, the linewidth of the transitions is almost constant for the different samples. This finding evidences the reproducible achievement of smooth interfaces in this rather complex materials system.

After having established the reproducible growth of (In,Ga)N / GaN MQWs with abrupt interfaces, we perform a detailed study of the actual emission mechanisms in these structures in the next Chapter.

8 Electrostatic fields and compositional fluctuations in (In,Ga)N/GaN multiple quantum wells

In this Chapter, we investigate the spontaneous recombination in (In,Ga)N / GaN MQWs. First, the influence of the internal electrostatic fields is examined as a function of the well width. Then, we study the temperature and energy dependence of the emission from thin wells in order to clarify the impact of compositional fluctuations on recombination. It will be shown that for a thorough understanding of spontaneous emission from these structures both electrostatic fields and compositional fluctuations have to be taken into account.

8.1 Different emission mechanisms

Despite the successful demonstration of (In,Ga)N / GaN MQW light emitting diodes (LEDs) and injection laser diodes (LDs) there still is a lack of agreement about the actual recombination mechanisms in these structures. The experimental results [130–134] are controversially discussed in terms of two different phenomena, namely, internal electrostatic fields and compositional fluctuations. In the following, it will first be discussed why these compositional fluctuations lead to experimental observations which may not be distinguished from those originating from internal electrostatic fields. Then, experiments are devised which allow to distinguish between these two phenomena.

Impact of compositional fluctuations on recombination Under thermal equilibrium, a miscibility gap is predicted on theoretical grounds for (In,Ga)N leading to spinodal decomposition (bulk segregation). [124] The usual deposition temperatures for both MBE and MOCVD grown (In,Ga)N are far too low for achieving thermal equilibrium. However, fluctuations of the In content are reported and attributed to instabilities of the growth front leading to compositional inhomogeneities and In clustering. [135,136] Excitons can be localized at regions having a higher In content than the surrounding material leading to two important consequences for recombination which depend on the actual localization depth. The larger this depth, the more the transition energy is red-shifted and the transition rate is reduced with respect to the free exciton. [137] In the experiment, these findings coincide with the consequences of internal electrostatic fields as outlined in Chapter 2 and experimentally verified in Chapter 6.

Therefore, it is impossible to separate electrostatic fields and compositional fluctuations by a single photoluminescence (PL) experiment. Also, absorption measurements fail to distinguish between these two phenomena since the oscillator strength is substantially reduced in both cases. Transitions with higher energy have a larger oscillator strength and thus a Stokes-like shift between emission and absorption is often reported. [138] Indeed, this shift is called apparent Stokes shift to acknowledge the fact that the ground state with its extremely low oscillator strength is simply unobservable in absorption.

A distinction between fields and fluctuations is possible by variations of parameters to which only either of these two is sensitive. Here, we will tune an internal parameter (well width) and an external parameter (PL measurement temperature) to access

Table 8.1: Structural parameters of the two (In,Ga)N / GaN MQWs as determined by x-ray diffraction. x, d_{InGaN} and d_{GaN} denote the In content in the well, the well thickness and the barrier thickness, respectively.

Sample	x	d_{InGaN} (nm)	d_{GaN} (nm)
W1	0.17	3.1	12.1
W2	0.16	5.9	8.8

electrostatic fields and compositional fluctuations, respectively.

(In,Ga)N wells grown under nominally identical conditions have very similar degrees of compositional inhomogeneity. Hence, the impact of electrostatic fields may be investigated by varying only the individual thicknesses of well and barrier but keeping the In content in the well constant. The resulting changes in emission energy and decay time may then be assigned to electrostatic fields with confidence. However, the examination of samples having different well widths relies on reproducibility of the growth procedure. Different phenomena such as In segregation, desorption and clustering are all thermally activated processes and thus critically depend on the deposition temperature. Instabilities of the latter may lead to substantial fluctuations of transition energies. For example, the transition energy is reported to shift as much as 250 meV by variations of only 10 K of the substrate temperature. [125] Here, the reproducibility is investigated by re-growth of a sample which emits at 2.83 eV at 5 K. (The original structure, labelled W1, is discussed in the next Section) The structural and optical properties of the re-grown sample are in sound agreement with the original structure. The 5 K peak position is shifted by less than 50 meV evidencing a sufficiently low error margin for comparison of different samples.

Direct access to compositional fluctuations is possible by investigation of the dimensionality of the system at different temperatures. At very low temperatures, excitons are localized and occupy zero-dimensional states. With increasing temperature, excitons are thermally activated and start to occupy extended, two-dimensional states of the quantum wells. A quantity reflecting the dimensionality of the system is the radiative decay time τ_{r} which is proportional to $T^{s/2}$ for a system having s dimensions.

8.2 Electrostatic fields

Samples under study Two samples (labelled W1 and W2) are investigated which consist of 10-period (In,Ga)N / GaN MQWs grown on 1 μm thick GaN(0001) buffer layers. In these samples, the layer thicknesses are varied utilizing different well deposition times but otherwise nominally identical growth conditions. Caution was used to achieve smooth interfaces in order to minimize the localization of carriers at well width fluctuations (see Chapter 7). Such well width fluctuations would lead to a significant red-shift as demonstrated in Chapter 7. The interfaces of the samples under investigation in this chapter are indeed smooth, as evidenced by a streaky RHEED pattern during growth.

The structural parameters of the two MQWs are examined in analogy to the procedure presented in Chapter 7, i. e., segregation of In is taken into account. The obtained structural parameters are listed in Tab. 8.1.

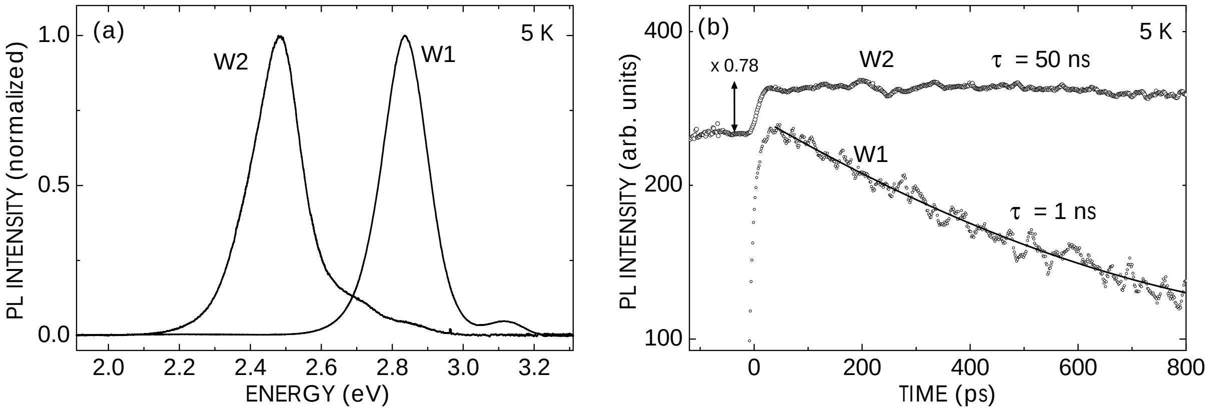

Figure 8.1: Recombination properties of (In,Ga)N / GaN MQWs at 5 K studied by (a) cw-PL and (b) TRPL. Note the red-shift in transition energy and the prolonged decay time of sample W2 with respect to sample W1. The decay time of sample W2 is estimated from the PL intensity ratio of 0.78 directly after and before the 13 ns separated excitation pulses.

The two samples have nearly identical MQW periods (15 nm) and In contents (0.16) in the well. These samples are thus ideally suited for a direct investigation of electrostatic fields as only the well width varies. It should be noted in this context that a direct kinematical analysis of the XRD profiles (neglecting In segregation) yields twice the In content and only half the well width with respect to the values in Tab. 8.1.

Experimental results The recombination properties of these samples are studied by continuous-wave PL and time-resolved PL at 5 K (Fig. 8.1). For experimental details see Chapters 5 and 6. The transition energy of sample W1 with the 3.1 nm wide wells is at 2.83 eV while sample W2 with its 5.9 nm wide wells is red-shifted to 2.48 eV. Moreover, the PL decay times are remarkably different. Sample W1 exhibits an almost monoexponential decay with a characteristic time constant around τ_{W1}=1 ns. In contrast, sample W2 exhibits a significantly prolonged decay time τ_{W2}. In fact, one can only estimate τ_{W2}=50 ns from the PL intensity ratio directly after and before the 13 ns separated excitation pulses under the assumption of a monoexpontential decay.

Discussion For a direct comparison of experimental results with theoretically expected transition energies the band profiles of these samples are calculated on the basis of the structural parameters in Tab. 8.1. These band profiles (Fig. 8.2) are dominated by the presence of strong electrostatic fields in these structures. The estimated transition energies are in very good agreement with the data in Fig. 8.1 as the calculated transition energies are 2.82 eV and 2.51 eV for sample W1 and W2, respectively. Moreover, the ratio of the radiative decay times can be estimated from the electron and hole wavefunction overlap. Theoretically, we expect $\tau_{W2} / \tau_{W1} \approx 110$ which is in fair agreement with the experimental value of 50 taking into account the uncertainty in τ_{W2}. These findings clearly demonstrate that electrostatic fields play an important role and must not be neglected for (In,Ga)N / GaN MQWs grown along the [0001] axis.

It is interesting to calculate the transition energies based on the structural parameters obtained by neglecting In segregation (see above). These values results in transition energies of 2.89 eV and 2.38 eV which are significantly different from the experimental data. In this case, one might conclude that the electrostatic fields calculated from the polarization fields of Bernadini *et al.* [25] are too large. Indeed, a reduction of the

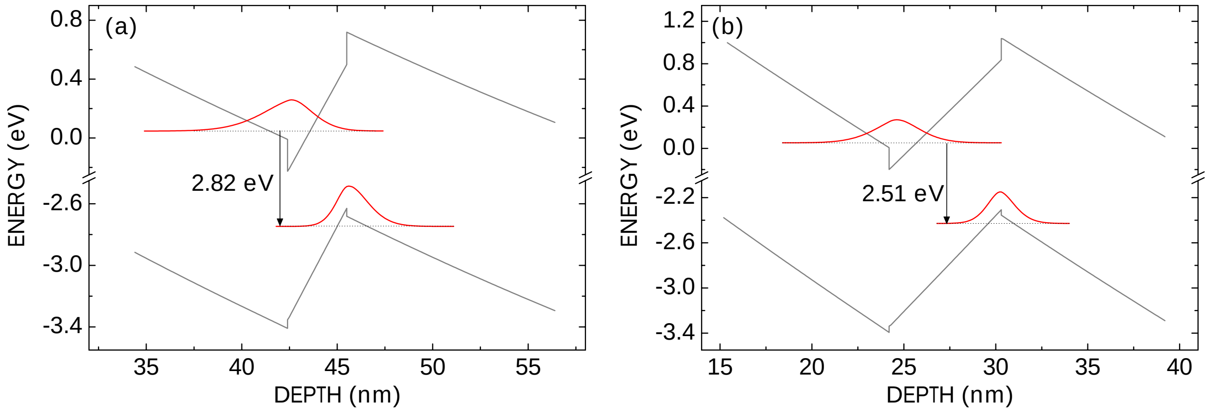

Figure 8.2: Band profiles of (In,Ga)N / GaN MQW under study for (a) sample W1 and (b) sample W2. The transition energies are given in the Figure.

electrostatic fields by a factor of 2 leads to a better agreement such that the difference in transition energies is close to the experimentally observed value of 0.35 eV. This phenomenon is in perfect accordance with the results of the last chapter. Incorrect structural determination of (In,Ga)N / GaN MQWs will lead to the (wrong) conclusion that the electrostatic fields are smaller than theoretically expected. In contrast, careful structural characterization leads to excellent agreement of calculation and experiment.

8.3 Energy and temperature dependence of the radiative decay time

Strong internal electric fields are thus always present in our structures. However, a sample with thin wells is ideally suited to investigate effects which are related to compositional fluctuations. Therefore, we focus on sample W1 with its 3 nm thin wells.

Energy dependence of radiative decay time We first examine the dependence of the PL decay time τ_{PL} on emission energy [Fig. 8.3(a)]. While the decay time is about 250 ps in the vicinity of the weak high-energy peak, τ_{PL} increases to approximately 1 ns as the emission energy approaches the main low-energy peak. The high-energy side of the main PL band shifts to the red in the course of time [Fig. 8.3(b)], causing an overall spectral narrowing of this band. Immediately after the excitation the linewidth is about 200 meV but then decreases to about 140 meV. These findings are consistent with a progressive relaxation of carriers into the states associated with the main emission band.

Measurement of the radiative decay time We now investigate the temperature dependence of the radiative decay time τ_{r}. Ideally, this value can be extracted from the combined measurement of the PL decay time $\tau(T) = (1/\tau_{\mathrm{r}} + 1/\tau_{\mathrm{nr}})^{-1}$ and the steady-state PL intensity $I_{\mathrm{PL}}(T) = \eta_{\mathrm{PL}}(T) I_{\mathrm{PL}}(0)$, with the quantum efficiency $\eta_{\mathrm{PL}}(T) = \tau_{\mathrm{PL}}/\tau_{\mathrm{r}}$. Note that the dynamics of the transients may not be sufficient to accurately determine the PL decay time up to room temperature. Furthermore, we face bi- or multi-exponential decays for higher temperatures which are characteristic of capture processes. Therefore, the question arises which value to take for τ_{PL}.

We circumvent these ambiguities here by noting that the radiative decay time τ_{r} is proportional to the inverse of the spectrally integrated TRPL peak intensity divided

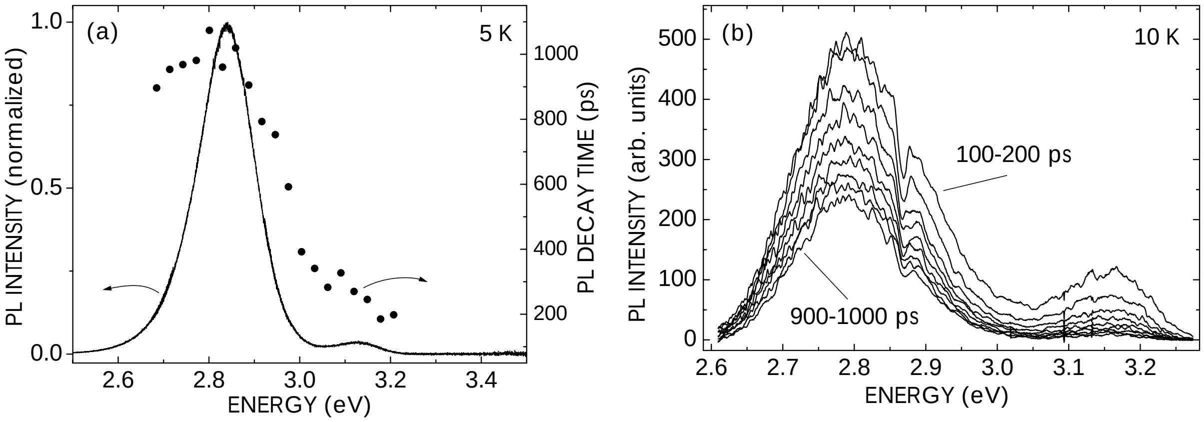

Figure 8.3: TRPL decay of sample W1: (a) spectral dependence of the PL decay time, (b) transient spectra separated by 100 ps. The dip of the PL spectra at 2.85 eV is spurious.

by the incident fluence. This result can be derived as follows. Consider an excitation pulse $G(t)$ which generates excess carriers of density n_{GaN} in the GaN barriers. These carriers will relax to the (In,Ga)N wells with a relaxation time τ_{rel} establishing a density $n_{(\mathrm{In,Ga})\mathrm{N}}$ in the well. The temporal evolution of these excess carrier densities is governed by the rate-equations

$$\frac{d}{dt} n_{\mathrm{GaN}} = G(t) - \frac{n_{\mathrm{GaN}}}{\tau_{\mathrm{rel}}} \tag{8.1}$$

$$\frac{d}{dt} n_{(\mathrm{In,Ga})\mathrm{N}} = + \frac{n_{\mathrm{GaN}}}{\tau_{\mathrm{rel}}} - \frac{n_{(\mathrm{In,Ga})\mathrm{N}}}{\tau_{\mathrm{r}}} - \frac{n_{(\mathrm{In,Ga})\mathrm{N}}}{\tau_{\mathrm{nr}}} \tag{8.2}$$

For a Gaussian shaped excitation pulse $G(t)$ with a pulse width Δt, these coupled equations can be solved analytically under the boundary condition of zero excess carriers prior to the excitation pulse. Moreover, if both Δt and τ_{rel} are small compared to any recombination process in the sample, then it can be shown that the peak PL intensity of the transient is proportional to τ_{r}^{-1}. In the present case, both conditions are fulfilled. The pulse width is around 400 fs whereas the PL rise time sets an upper limit of 10 ps for the relaxation time τ_{rel}.

Since we do not measure the PL intensity in absolute units, this procedure requires assigning a value for τ_{r} at some temperature. We choose the value of τ_{PL}, at 5 K as here the decay is monoexponential apart from a very short initial capture process.

Rate-equation model The corresponding values for $\tau_{\mathrm{r}}(T)$ are shown in Fig. 8.4 together with a fit based on a rate-equation model to the data (the model is a modification of an approach originally developed for thick GaN layers [139]). This model is based on the assumption that radiative recombination is possible from either extended states in an ideal quantum well (2D states with occupation density n_{x}) or localized states (0D states with occupation density n_{b}). Transfer between these two kinds of states is incorporated by coupling terms. The temporal evolution of the corresponding occupation densities is described for the present case of excitonic recombination in the small-signal limit (note the very low excitation fluence of 1 nJ/cm^2) by the rate-equations

$$dn_{\mathrm{x}}/dt = -\gamma_{\mathrm{x}} n_{\mathrm{x}} - b_{\mathrm{r}} n_{\mathrm{x}} N_{\mathrm{F}} + b_{\mathrm{e}} n_{\mathrm{b}} \tag{8.3}$$

$$dn_{\mathrm{b}}/dt = -\gamma_{\mathrm{b}} n_{\mathrm{b}} + b_{\mathrm{r}} n_{\mathrm{x}} N_{\mathrm{F}} - b_{\mathrm{e}} n_{\mathrm{b}} \tag{8.4}$$

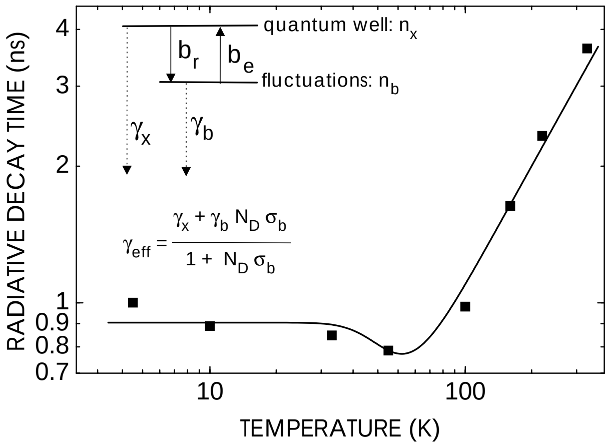

Figure 8.4: Measured (symbols) and fit (line) radiative lifetimes vs temperature of the main peak of sample W1.

where γ_x and γ_b are radiative recombination coefficients. The two other terms describe the capture (b_r) and emission (b_e) of localized excitons. N_F denotes the density of unoccupied localized states with a total density of $N_L = N_F + n_b$ of localized states available.

First, we consider the equilibrium occupation densities n_b^0 and n_x^0 of n_b and n_x, respectively. The present situation constitutes a classical two-level systems with states $|F\rangle$ and $|b\rangle$. The former corresponds to an empty localized state with a density N_F^0 while the latter refers to an occupied localized state with a density n_b^0. Note that the occupied state has a lower energy than the empty state.

In equilibrium, we have

$$N_F^0 = n_b^0 \exp(-E_{loc}/kT), \quad n_x^0 = N_x \exp(-E_x/kT) \tag{8.5}$$

with the localization energy E_{loc}, the total density of extended states N_x and the exciton binding energy E_x (26 meV).

Using the detailed balance expression $b_r n_x^0 N_F^0 = b_e n_b^0$, we obtain the cross section

$$\sigma_b = \frac{b_r}{b_e} = \frac{1}{N_x} \exp\left(\frac{E_b}{kT}\right) \tag{8.6}$$

for capture of an exciton by a localized state with the localization binding energy $E_b = E_x - E_{loc}$. Note this definition of E_b is analogous to the binding energy of an exciton localized at a dopant.

Second, we consider the dynamic behavior of the system. Here, we assume that capture and emission processes are very fast compared to radiative transitions even after excitation ($b_e, b_r \gg \gamma_x, \gamma_b$). Hence, $b_b n_x N_F \approx b_e n_b$. One obtains an expression which relates the density n_b of occupied localized states with the density n_x of occupied extended states:

$$n_b = \frac{n_x \sigma_b N_D}{1 + \sigma_b n_x} \tag{8.7}$$

Third, we add Eqs. (8.3) and (8.4) and use expression (8.7) to obtain

$$\frac{dn_\mathrm{x}}{dt} = \frac{-\gamma_\mathrm{x} n_\mathrm{x} - \frac{\gamma_\mathrm{b}\sigma_\mathrm{b} N_\mathrm{L} n_\mathrm{x}}{1+\sigma_\mathrm{b} n_\mathrm{x}}}{1 + \frac{N_\mathrm{D}\sigma_\mathrm{b}}{(1+\sigma_\mathrm{b} n_\mathrm{x})^2}} \approx -\left[\frac{\gamma_\mathrm{x} + \gamma_\mathrm{b}\sigma_\mathrm{b} N_\mathrm{L}}{1 + N_\mathrm{L}\sigma_\mathrm{b}}\right] n_\mathrm{x} = -\gamma_\mathrm{eff} n_\mathrm{x} \tag{8.8}$$

where the small-signal limit $n_\mathrm{x}\sigma_\mathrm{b} \ll 1$ has been used, as the maximum excess carrier density in our experiments is around 10^{15} cm^{-3}.

Fit to the data The effective transition rate $\gamma_\mathrm{eff}=\tau_\mathrm{eff}^{-1}$ describes the common radiative transition rate of the whole system. It is easily seen that this expression mediates between the limiting cases of $\gamma_\mathrm{eff} \to \gamma_\mathrm{b}$ for $T \to 0$ and $\gamma_\mathrm{eff} \to \gamma_\mathrm{x}$ for $T \to \infty$ as well as of $\gamma_\mathrm{eff} \to \gamma_\mathrm{x}$ for $N_\mathrm{L} \to 0$ and $\gamma_\mathrm{eff} \to \gamma_\mathrm{b}$ for $N_\mathrm{L} \to \infty$. Furthermore, for $E_\mathrm{b} \to \infty$ and $E_\mathrm{b} \to 0$, the value of γ_eff approaches γ_b and γ_x, respectively. The decay rate γ_x of a free exciton is given by a_x/T, and γ_b is independent of temperature. The very satisfactory fit to the data (Fig. 8.4) yields $E_\mathrm{b} = 22$ meV, $N_\mathrm{L} = 3 \times 10^{10}$ cm^{-2}, $\gamma_\mathrm{b} = 1.1$ ns^{-1} and $a_\mathrm{x} = 88$ ns^{-1} K. This localization depth is considerably smaller than the usually reported values (more than 100 meV) [140] It is clear from our model that such a deep localization would lead to a constant radiative decay time at least up to room temperature.

The results of the previous two sections lead to the following conclusion. In the case of thin quantum wells with high In content, localization in potential fluctuations governs the recombination whereas electrostatic fields are dominant in the case of thick wells having a low In content. If quantum wells in-between these limiting cases are considered, one has to take into account the coexistence of both effects to consistently interpret the results.

9 Conclusion and Outlook

In this thesis, it has been shown that high-quality wurtzite nitride semiconductors can be synthesized with plasma-assisted molecular beam epitaxy. The *in-situ* evaluation and adjustment of the surface stoichiometry by reflection high-energy electron diffraction (RHEED) played a crucial role for the reproducible growth of these samples.

GaN films were deposited along the conventional polar [0001] direction on SiC(0001) substrate. A new degree of freedom for GaN epitaxy was demonstrated by the first wurtzite GaN synthesized along a non-polar direction, namely, $[1\bar{1}00]$ on γ-LiAlO$_2$(100) substrate. These films are single-phase within the detection limit of high-resolution x-ray diffraction and exhibit sufficiently smooth surface morphologies for subsequent growth of heterostructures. The structural quality of these samples was shown to be very sensitive to substrate preparation before growth. Smooth and clean SiC substrates resulted in excellent structural properties of GaN(0001) layers whereas GaN$(1\bar{1}00)$ films still suffer from the inferior morphological and chemical quality of γ-LiAlO$_2$(100) substrates.

Identically designed GaN / (Al,Ga)N multiple quantum wells (MQWs) deposited on these two types of GaN buffer layers reveal significant differences in recombination due to the different orientations of the nitride c-axis with respect to the growth direction. [0001] oriented GaN wells had an isotropic emission which is subject to strong internal electrostatic fields. In contrast, emission from $[1\bar{1}00]$ oriented GaN wells is consistent with the absence of electrostatic fields and is furthermore strongly polarized normal to the [0001] axis.

The growth of (In,Ga)N / GaN MQWs is dominated by In surface segregation yielding top-hat In profiles. The In segregation was shown to be a zeroth order process instead of the usually assumed first order process. Neglecting In segregation during metal-stable growth results in quantum wells with poor electron-hole wavefunction overlap since the well width is much larger than the intended one. Reduction of In segregation by N-stable conditions is possible but inevitably delivers rough interfaces. A strategy for obtaining (In,Ga)N / GaN MQWs with smooth interfaces and high quantum efficiency is devised.

The radiative recombination from (In,Ga)N / GaN MQWs is examined. It is demonstrated that both compositional fluctuations and electrostatic fields have to be taken into account for a thorough understanding of the emission from these structures. The temperature dependence of the radiative decay time is measured to probe the dimensionality of the system. For a quantitative understanding, a rate-equation model is utilized for analyzing the data. For low temperatures, recombination is governed by localized states whereas for high temperatures, extended states dominate. This analysis shows that the localization depth in these structures is below 25 meV.

One of the most important discoveries of this thesis is the successful growth of wurtzite GaN along the non-polar $[1\bar{1}00]$ direction. Future work on this fascinating finding should concentrate on the following three issues.

First, γ-LiAlO$_2$(100) substrates are still of inferior quality when compared to SiC(0001) wafers. Improvements of the γ-LiAlO$_2$(100) surface is expected to provide GaN$(1\bar{1}00)$ layers of similar quality as the GaN(0001) films. Therefore, a substrate cleaning procedure should be developed which is compatible with the strong chemical reactivity of γ-LiAlO$_2$(100). First results from sputtering experiments already indicate the feasibility of achieving a good morphological and chemical quality of γ-LiAlO$_2$(100) wafers.

Second, incorporation of In and dopants is known to strongly depend on the growth direction. For example, In has the lowest incorporation rate on GaAs(111) but the highest on GaAs(001). Si is an amphoteric dopant in GaAs and in fact is a donor on GaAs(001) but an acceptor on GaAs(11h)A with h$\leq$3. In the course of this thesis, preliminary results from p-type doping of GaN(0001) with Mg were obtained and functional homojunction diodes were fabricated. However, in agreement with very recent reports, [141, 142] polarity inversion from Ga-face to N-face was observed once a certain Mg concentration was exceeded (10^{19} cm^{-3}) on the Ga-face layer. This finding shows that p-type doping of GaN is still an important issue which needs to be investigated in detail. Furthermore, doping of layers grown along the non-polar [$1\bar{1}00$] orientation (where polarity inversion is impossible) is an entirely new research field which might well shed light on some of the as yet unclarified issues in this context. A comparative study of GaN(0001) and GaN($1\bar{1}00$) should be carried out in order to investigate In segregation and to explore the limits of p-type doping of GaN.

Third, a very promising concept for high brightness white LEDs can be realized with GaN($1\bar{1}00$) if p-type doping is successful. Present white LEDs consist of a blue LED pumping a yellow phosphor. These LEDs only approach the luminous efficiency of conventional light bulbs (12 lm / W). Moreover, the emission of these LEDs is not conceived as true white by the eye, since the inevitable scatter of the wavelength of the pump light results in, e.g., a bluish or yellowish color impression. An alternative and conceptually superior approach consists of an ultraviolet (UV) LED pumping a white phosphor. Here, the color impression can reproducibly be adjusted by choosing the appropriate phosphor. Currently, however, the power efficiency of UV LEDs (1–2%) is much inferior compared to blue LEDs (10–12%) due to the poor electron-hole wavefunction overlap in [0001] oriented GaN / (Al,Ga)N MQWs. The addition of In, as practiced in blue LEDs, increases the quantum efficiency via carrier localization but comes at the expense of an unreproducible red-shift in emission. This shift is reflected in a deviation from truly white emission as described above. An elegant solution to this problem is provided by [$1\bar{1}00$] oriented wells. These wells are free of internal electrostatic fields, thus enabling true UV emission with a high quantum efficiency at room temperature. Consequently, these devices combined with white phosphor would constitute an important step towards the lighting elements of the future.

A Origin of-high energy shoulders of (In,Ga)N/GaN MQW PL spectra

It was already briefly mentioned in Chapter 7 that the high-energy peak or shoulder of the main peak originates from the quantum well closest to the GaN buffer layer. Of course, one might also suspect that lateral inhomogeneities lead to the high-energy peak. Therefore, lateral and vertical variations of the emission of sample W1 (see Chapter 8) are investigated by cathodoluminescence (CL).

Spatial resolution in CL Lateral changes are detected by taking spot excitation spectra under identical excitation conditions but different positions on the sample surface. In contrast, vertical resolution is obtained by tuning the acceleration voltage of the electron beam. In both modes, the spatial resolution is limited by two factors, namely, the energy dissipation volume of the incident beam and, second, diffusion of excess carriers. For GaN, Monte-Carlo simulations for acceleration voltages up to 25 kV show that the dissipation volume corresponds to a half sphere whose center is at the sample surface. The radius R of this sphere can be estimated from the acceleration voltage. [143] Exemplary values of R are 2.8 and 0.1 μm for voltages of 25 and 3 kV, respectively. The diffusion length L inside the MQW stack strongly depends on direction. Vertical diffusion in the MQW is, if any, negligible. In contrast, lateral diffusion must not be neglected since L can be as large as one micrometer at low temperatures. [144] Hence, the vertical and lateral CL resolutions are limited by R and L, respectively.

In the following experiments, the electron beam current is fixed at 1 nA throughout the measurements which are carried out at 5 K. For the lateral scans, an acceleration voltage of 10 kV is employed yielding a spatial resolution better than 600 nm for fixed position. In contrast, the vertical scans are laterally averaged over an area of several μm^2. The acceleration voltage is tuned from 3 up to 25 kV leading to the range given above for R.

Lateral scans Spectra taken during the lateral scans are shown in Fig. A.1 for 35 positions along a 6.5 μm long line on the sample surface. The individual intensities of the spectra fluctuate due to inhomogeneities of the wells as usually observed for quan-

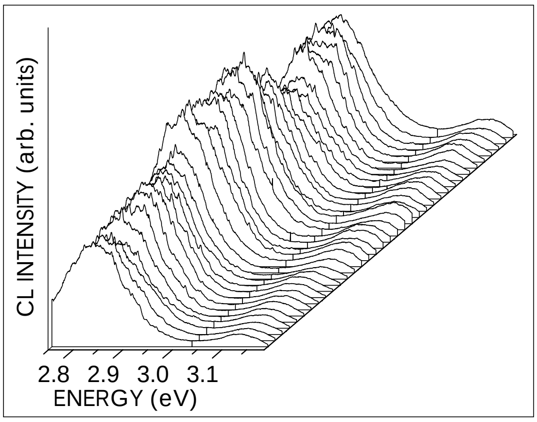

Figure A.1: CL spectra of sample W1 along a 6.5 μm long lateral line. Note the stable intensity ratio of the two peaks and the fine structure of the spectra.

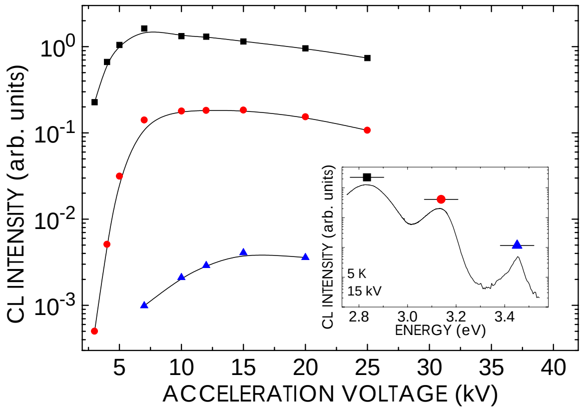

Figure A.2: Intensities of the main peak (squares), high-energy peak (circles) and the GaN buffer (triangles), note the different positions of the individual maxima and the steep increase of the higher energy peak intensity for 3–5 kV. The CL spectra of sample W1 for different acceleration voltages are shown in the inset.

tum wells. [145] The intensity ratio of the two peaks is very stable demonstrating that the existence of the higher energy peak is not related to a lateral inhomogeneity of the sample. One observes a fine structure of the spectrum, in particular for the main peak at 2.82 eV. This fine structure is likely to arise from recombination of localized carriers as well-known for other system such as GaAs/(Al,Ga)As quantum wells. [145] Note that this fine structure is not observed when the luminescence is averaged over larger areas.

Vertical scans Results from the vertical scans are shown in Fig. A.2. The intensities of the main, the higher energy as well as the GaN buffer peak are given for different acceleration voltages. The intensities of all three peaks first increase, reach a maximum and finally decrease again since for a voltage of 25 kV a large fraction of the dissipation volume already penetrates into the SiC substrate. It is important to note that the maxima have distinct values for the acceleration voltage: Approximately 7, 12.5 and 15 kV for the main, higher energy and GaN buffer peak. This result shows that the dif-

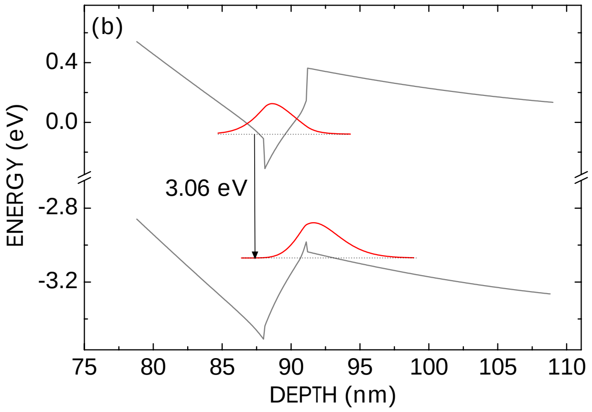

Figure A.3: Band profile for sample W1 of the well closest to the GaN buffer. A two monolayer thin doping spike with density 2.5×10^{19} cm^{-3} is introduced into the well at the well/buffer interface in order to account for the accumulation of impurities during the growth interruption. All other wells have a homogeneous doping level of 10^{17} cm^{-3}.

ferent peaks originate from transitions stemming from different depths of the sample. Moreover, the higher energy peak increases extremely steeply for voltages of 3–5 kV corresponding to dissipation sphere radii of 100–200 nm. This range is in sound agreement with the total thickness of the MQW of 150 nm. Therefore, it is justified to assign the high energy peak to the well closest to the GaN buffer layer.

The question arises why the first well has such a significantly different transition energy. This point can be clarified by taking into account the growth interruption of about 550 s between GaN buffer and MQW (see Section A) leading to a substantially higher doping level of the first well. We assume that all the excess dopants are equally distributed in the first two monolayers leading to a doping spike with a density of 2.5×10^{19} cm^{-3}.

The resulting band profile of this well is displayed in Fig. A.3. The electrostatic field in the well is smaller than for the other wells [Fig. 8.2(a)] due to screening. This fact leads to a blue-shift in emission and an increase of the electron-hole wavefunction overlap. The calculated transition energy of 3.06 eV is in agreement with the experimental value of 3.12 eV. Moreover, theoretically we estimate a ratio of 9 for the decay times. This value is in fair agreement with the observed value of 4 [1 ns / 250 ps, see Fig. 8.3(a)].

Bibliography

[1] M. Meyer, Compound Semiconductor **6**, (2000).

[2] A. Biermann, Lighting Futures **3**, (1998).

[3] W. C. Johnson, J. B. Parsons, and M. C. Crew, J. Phys. Chem. **36**, 2651 (1932).

[4] E. Tiede, M. Thimann, and K. Sensee, Chem. Berichte **61**, 1568 (1928).

[5] R. Juza and E. Hahn, Z. Anorg. Allgem. Chem. **234**, 282 (1938).

[6] H. P. Maruska and J. J. Tietjen, Appl. Phys. Lett. **15**, 327 (1969).

[7] J. I. Pankove, E. A. Miller, and J. E. Berkeyheiser, J. Luminescence **5**, 84 (1972).

[8] I. Akasaki, T. Kozowa, K. Hiramatsu, N. Sawak, K. Ikeda, and Y. Ishii, J. Luminescence **40/41**, 121 (1988).

[9] H. Amano, M. Kito, K. Hiramatsu, and I. Akasaki, Jpn. J. Appl. Phys. **28**, L2112 (1989).

[10] S. Nakamura and G. Fasol, *The Blue Laser Diode* (Springer-Verlag, Berlin, 1997).

[11] I. P. Smorchkova, C. R. Elsass, J. P. Ibbetson, R. Vetury, B. Heying, P. Fini, E. Haus, S. P. DenBaars, J. S. Speck, and U. K. Mishra, J. Appl. Phys. **86**, 4520 (1999).

[12] L. De Caro, C. Giannini, and L. Tapfer, Phys. Rev. B **56**, 9744 (1997).

[13] L. De Caro and L. Tapfer, J. Appl. Cryst. **31**, 831 (1998).

[14] S. Haussühl, *Kristallphysik* (Physik-Verlag, Weinheim, 1983).

[15] K. Kim, W. R. L. Lambrecht, and B. Segall, Phys. Rev. B **53**, 16310 (1996).

[16] C. Kisielowski, J. Krüger, S. Ruvimov, T. Suski, J. W. Ager, E. Jones, Z. Lilienthal-Weber, M. Rubin, E. R. Weber, and M. D. Bremser, Phys. Rev. B **54**, 17745 (1996).

[17] R. Langer, J. Simon, V. Oritz, N. T. Pelekanos, A. Barski, R. Andre, and M. Godlewski, Appl. Phys. Lett. **74**, 3827 (1999).

[18] P. Lefebvre, J. Allegre, B. Gil, H. Mathieu, N. Grandjean, M. Leroux, J. Massies, and P. Bigenwald, Phys. Rev. B **59**, 15363 (1999).

[19] R. Cingolani, A. Botchkarev, H. Tang, H. Morkoç, G. Traetta, G. Coli, M. Lomascolo, A. D. Carlo, F. Della Sala, and P. Lugli, Phys. Rev. B **61**, 2711 (2000).

[20] A. Thamm, O. Brandt, J. Ringling, A. Trampert, K. H. Ploog, O. Mayrock, H.-J. Wünsche, and F. Henneberger, Phys. Rev. B **61**, 16025 (2000).

[21] W. Ludwig, *Festkörperphysik* (Akademische Verlagsgesellschaft, Wiesbaden, 1978).

[22] A. F. Wright and J. S. Nelson, Phys. Rev. B **60**, 2159 (1994).

[23] G. Capellini, V. Fiorentini, K. Tenelsen, and F. Bechstedt, in *Gallium Nitride and Related Materials*, edited by R. D. Dupuis (Materials Research Society, Pittsburgh, 1996).

[24] F. Bechstedt, U. Grossner, and J. Furthmüller, Phys. Rev. B **62**, 8003 (2000).

[25] F. Bernadini, V. Fiorentini, and D. Vanderbilt, Phys. Rev. B **56**, R10024 (1997).

[26] F. Bernadini and V. Fiorentini, Phys. Rev. B **57**, R9427 (1998).

[27] V. Fiorentini and F. Berndini, Phys. Rev. B **60**, 8849 (1999).

[28] J. E. Northrup and J. Neugebauer, Phys. Rev. B **53**, R10477 (1996).

[29] S.-H. Park and S.-L. Chuang, Appl. Phys. Lett. **76**, 1981 (2000).

[30] M. Leroux, N. Grandjean, J. Massies, B. Gil, P. Lefebvre, and P. Bigenwald, Phys. Rev. B **60**, 1496 (1999).

[31] W. Shan, W. Walukiewicz, E. E. Haller, B. D. Little, J. J. Song, M. D. McCluskey, N. M. Johnson, Z. C. Feng, M. Schurman, and R. A. Stall, J. Appl. Phys. **84**, 4452 (1998).

[32] L. T. Romano, B. S. Krusor, M. D. McCluskey, D. P. Bour, and K. Nauka, Appl. Phys. Lett. **73**, 1757 (1998).

[33] W. Shan, B. D. Little, J. J. Song, Z. C. Feng, M. Schurman, and R. A. Stall, Appl. Phys. Lett. **69**, 3315 (1996).

[34] A. F. Wright and J. S. Nelson, Appl. Phys. Lett. **66**, 3051 (1995).

[35] L. Tapfer, Physica Scripta **T25**, 45 (1989).

[36] P. F. Fewster, Semicon. Sci. Technol. **8**, 1915 (1993).

[37] L. Tapfer, L. De Caro, C. Giannini, H.-P. Schönherr, and K. H. Ploog, Sol. State Commun. **98**, 599 (1996).

[38] L. De Caro, C. Giannini, and L. Tapfer, J. Appl. Phys. **79**, 4101 (1996).

[39] M. Schuster, P. O. Gervais, B. Jobst, W. Hösler, R. Averbeck, H. Riechert, A. Iberl, and R. Stömmer, J. Phys. D **32**, A56 (1999).

[40] L. Görgens, O. Ambacher, M. Stutzmann, C. Miskys, F. Scholz, and J. Off, Appl. Phys. Lett. **76**, 577 (2000).

[41] S. Gehrsitz, H. Sigg, N. Herres, K. Bachem, K. Köhler, and F. K. Reinhart, Phys. Rev. B **60**, 11601 (1999).

[42] R. Zaus, J. Appl. Cryst. **26**, 801 (1993).

[43] S. A. Stepanov, E. A. Kondrashkina, R. Köhler, D. V. Novikov, G. Materlik, and S. M. Durbin, Phys. Rev. B **57**, 4829 (1998).

[44] M. Grundmann and A. Krost, phys. stat. sol. (b) **218**, 417 (2000).

[45] B. Heying, X. H. Wu, S. Keller, Y. Li, D. Kapolnek, B. P. Keller, S. P. DenBaars, and J. S. Speck, Appl. Phys. Lett. **68**, 643 (1996).

[46] S. Stepanov and R. Köhler, J. Phys. D **27**, 1922 (1994).

[47] A. Krost, G. Bauer, and J. Woitok, in *Optical characterization of epitaxial semiconductor layers*, edited by G. Bauer and W. Richter (Springer-Verlag, Berlin, 1996).

[48] T. Baumbach, H.-G. Brühl, H. Rhan, and U. Pietsch, J. Appl. Cryst. **21**, 386 (1988).

[49] P. Y. Yu and M. Cardona, *Fundamentals of Semiconductors* (Springer-Verlag, Berlin-Heidelberg, 1996).

[50] W. L. Bond, Acta Crystallogr. **13**, 814 (1960).

[51] H. Romanus, G. Teichert, and L. Spiess, Mat. Sci. For. **264-268**, 437 (1998).

[52] S. Porowski, J. Cryst. Growth **189/190**, 153 (1998).

[53] H. Morkoç, *Nitride semiconductors and devices* (Springer-Verlag, Berlin-Heidelberg, 1999).

[54] M. Yamaguchi, T. Yagiand, T. Sota, T. Deguchi, K. Shimada, and S. Nakamura, J. Appl. Phys. **85**, 8502 (1999).

[55] W. G. Perry, T. Zheleva, M. D. Bremser, R. F. Davis, W. Shan, and J. J. Song, J. Electron. Mater. **26**, 224 (1997).

[56] C. Kirchner, V. Schwegler, F. Eberhard, M. Kamp, K. J. Ebeling, K. Kornitzer, T. Ebner, K. Thonke, R. Sauer, P. Prystawko, M. Leszczynski, I. Grzegory, and S. Porowski, Appl. Phys. Lett. **75**, 1098 (1999).

[57] P. Fini, L. Zhao, B. Moran, M. Hansen, H. Maechand, J. P. Ibbetson, S. P. DenBaars, U. K. Mishra, and J. S. Speck, Appl. Phys. Lett. **75**, 1706 (1999).

[58] S. Nakamura, in *Optical Properties of GaN and Related Materials*, edited by S. J. Pearton (Gordon & Breach, Amsterdam, 1998).

[59] M. A. Sánchez-García, E. Calleja, F. J. Sánchez, F. Calle, E. Monroy, D. Basak, E. Muñoz, C. Villar, A. Sanz-Herváz, M. Aguilar, J. J. Serrano, and M. Blanco, J. Electron. Mater. **27**, 276 (1998).

[60] S. Nakamura, T. Mukai, and M. Senoh, Appl. Phys. Lett. **64**, 1687 (1994).

[61] V. Ramachandran, R. M. Feenstra, W. L. Sarney, L. Salamanca-Riba, and D. W. Greve, J. Vac. Sci. Technol. A **18**, 1915 (2000).

[62] S. Bidnyk, B. D. Little, T. J. Schmidt, Y. H. Cho, J. Krasinski, J. J. Song, B. Goldenberg, W. Yang, W. G. Perry, M. D. Bremser, and R. F. Davis, J. Appl. Phys. **85**, 1792 (1999).

[63] O. Brandt, in *Group III Nitride Semiconductor Compounds: Physics and Applications*, edited by B. Gil (Oxford University Press, Oxford, 1998).

[64] T. Lei, K. F. Ludwig, and T. D. Moustakas, J. Appl. Phys. **74**, 4430 (1993).

[65] W. A. Melton and J. I. Pankove, J. Cryst. Growth **178**, 168 (1997).

[66] K. Iwata, H. Asahi, K. Asami, R. Kuroiwa, and S. Gonda, Jpn. J. Appl. Phys. **36**, L661 (1997).

[67] I. Schnitzer, E. Yablonovitch, C. Caneau, T. J. Gmitter, and A. Scherer, Appl. Phys. Lett. **63**, 2174 (1993).

[68] J. Fricke, B. Yang, O. Brandt, and K. H. Ploog, Appl. Phys. Lett. **74**, 3471 (1999).

[69] M. Marezio, Acta Cryst. **19**, 396 (1965).

[70] E. S. Hellman, Z. Lilienthal-Weber, and D. N. E. Buchanan, MRS Internet J. Nitride Semicond. Research **1**, 30 (1997).

[71] B. Yang, A. Trampert, B. Jenichen, O. Brandt, and K. H. Ploog, Appl. Phys. Lett. **73**, 3869 (1998).

[72] V. Ramachandran, M. F. Brady, A. R. Smith, R. M. Feenstra, and D. W. Greve, J. Electron. Mater. **27**, 308 (1998).

[73] C. D. Lee, V. Ramachandran, A. Sagar, R. M. Feenstra, D. W. Greve, W. L. Sarney, L. Salamanca-Riba, D. C. Look, S. Bai, W. J. Choyke, and R. P. Devaty (unpublished).

[74] S. W. King, R. J. Nemanich, and R. F. Davis, J. Electrochem. Soc. **146**, 1910 (1999).

[75] S. W. King, R. J. Nemanich, and R. F. Davis, J. Electrochem. Soc. **146**, 2648 (1999).

[76] R. Kaplan, Surf. Sci. **215**, 111 (1989).

[77] S. Strite, M. E. Lin, and H. Morkoç, Thin Solid Films **31**, 197 (1993).

[78] S. W. King, C. Ronning, R. F. Davis, R. S. Busby, and R. J. Nemamich, J. Appl. Phys. **84**, 6042 (1998).

[79] F. Owman and P. Mårtensson, J. Vac. Sci. Technol. B **14**, 933 (1996).

[80] N. V. Edwards, M. D. Bremser, R. F. Davis, A. D. Batchelor, S. D. Yoo, C. F. Karan, and D. E. Aspnes, Appl. Phys. Lett. **73**, 2808 (1998).

[81] B. Monemar, in *Gallium Nitride (GaN) I*, edited by J. I. Pankove and T. D. Moustakas (Academic Press, San Diego, 1998).

[82] A. D. Bykhovski, B. L. Gelmont, and M. S. Shur, J. Appl. Phys. **81**, 6332 (1997).

[83] R. F. Davis, T. W. Weeks, M. D. Bremser, S. Tanaka, R. S. Kern, Z. Sitar, K. S. Ailey, W. G. Perry, and C. Wang, Mat. Res. Soc. Proc. **287**, 3 (1995).

[84] S. Tanaka, S. Iwai, and Y. Aoyagi, J. Cryst. Growth **170**, 329 (1997).

[85] A. R. Smith, R. M. Feenstra, D. W. Grewe, M. S. Shin, M. Skowronski, J. Neugebauer, and J. E. Northrup, J. Vac. Sci. Technol. B **16**, 2242 (1998).

[86] E. S. Hellman, MRS Internet J. Nitride Semicond. Research **3**, 11 (1998).

[87] A. R. Smith, R. M. Feenstra, D. W. Grewe, J. Neugebauer, and J. E. Northrup, Phys. Rev. Lett. **79**, 3934 (1997).

[88] T. Zywietz, J. Neugebauer, and M. Scheffler, Appl. Phys. Lett. **73**, 487 (1998).

[89] E. J. Tarsa, B. Heying, X. H. Wu, P. Fini, S. P. DenBaars, and J. S. Speck, J. Appl. Phys. **82**, 5472 (1997).

[90] P. Hacke, G. Feuillet, H. Okumura, and S. Yoshida, Appl. Phys. Lett. **69**, 2507 (1996).

[91] B. Heying, R. Averbeck, L. F. Chen, E. Haus, H. Riechert, and J. S. Speck, J. Appl. Phys. **88**, 1855 (2000).

[92] J. H. Neave, B. A. Joyce, P. J. Dobson, and N. Norton, Appl. Phys. A **31**, 1 (1983).

[93] L. X. Zheng, M. H. Xie, and S. Y. Tong, Phys. Rev. B **61**, 4890 (2000).

[94] B. Daudin and F. Widmann, J. Cryst. Growth **182**, 1 (1997).

[95] S. Guha, N. A. Bojarczuk, and D. W. Kisker, Appl. Phys. Lett. **69**, 2879 (1996).

[96] D. Kapolnek, X. H. Wu, B. Heying, S. Keller, B. P. Keller, U. K. Mishra, S. P. DenBaars, and J. S. Speck, Appl. Phys. Lett. **67**, 1541 (1995).

[97] B. Heying, E. J. Tarsa, C. R. Elsass, P. Fini, S. P. DenBaars, and J. S. Speck, J. Appl. Phys. **85**, 6470 (1999).

[98] A. Thamm, O. Brandt, Y. Takemura, A. Trampert, and K. H. Ploog, Appl. Phys. Lett. **75**, 944 (1999).

[99] H.-P. Schönherr, J. Fricke, K.-J. Friedland, R. Nötzel, and K. H. Ploog, Appl. Phys. Lett. **72**, 566 (1998).

[100] E. J. Heller and M. G. Lagally, Appl. Phys. Lett. **60**, 2675 (1992).

[101] H. Heinke, V. Kirchner, S. Einfeldt, and D. Hommel, Appl. Phys. Lett. **77**, 2145 (2000).

[102] T. Kozawa, T. Kashi, H. Kono, H. Nagase, K. Koide, and K. Manabe, Appl. Phys. Lett. **77**, 4389 (1995).

[103] T. Azuhata, T. Sola, K. Suzuki, and S. Nakamura, J. Phys. C **7**, L129 (1995).

[104] S. Strite and H. Morkoç, J. Vac. Sci. Technol. B **10**, 1237 (1992).

[105] O. Ambacher, M. Arzberger, D. Brunner, H. Angerer, F. Freudenberg, N. Esser, T. WEethkamp, K. Wilmers, W. Richter, and M. Stutzmann, MRS Internet J. Nitride Semicond. Research **2**, 22 (1997).

[106] M. Ramsteiner, J. Menniger, O. Brandt, H. Yang, and K. Ploog, Appl. Phys. Lett. **69**, 1276 (1996).

[107] J. Neugebauer and C. G. V. de Walle, Appl. Phys. Lett. **69**, 503 (1996).

[108] F. A. Ponce, D. P. Bour, W. Götz, and P. J. Wright, Appl. Phys. Lett. **68**, 57 (1996).

[109] J. Elsner, R. Jones, P. K. Sitch, V. D. Porezag, M. Elstner, T. Frauenheim, M. I. Heggie, S. Öberg, and P. R. Briddon, Phys. Rev. Lett. **79**, 3672 (1997).

[110] P. Hirth and J. Lothe, *Theory of Dislocations* (Wiley-Interscience, New York, 1982).

[111] D. C. Look and R. J. Molnar, Appl. Phys. Lett. **70**, 3377 (1997).

[112] A. Rizzi, R. Lantier, F. Monti, H. Lüth, F. D. Sala, A. D. Carlo, and P. Lugli, J. Vac. Sci. Technol. B **17**, 1674 (1999).

[113] G. Martin, A. Botchkarev, A. Rockett, and H. Morkoç, Appl. Phys. Lett. **68**, 2541 (1996).

[114] T. Deguchi, K. Sekiguchi, A. Nakamura, T. Sota, R. Matsuo, S. Chichibu, and S. Nakamura, Jpn. J. Appl. Phys. **38**, L914 (1999).

[115] R. Dingle, D. D. Sell, S. E. Stokowski, and M. Ilegems, Phys. Rev. B **4**, 1211 (1971).

[116] A. Niwa, T. Ohtoshi, and T. Kuroda, Jpn. J. Appl. Phys. **35**, L599 (1996).

[117] K. Domen, K. Horino, A. Kuramata, and T. Tanahashi, Appl. Phys. Lett. **71**, 1996 (1997).

[118] B. Gil and A. Alemu, Phys. Rev. B **56**, 12446 (1997).

[119] N. Grandjean, B. Damilano, S. Dalmasso, M. Leroux, M. Laügt, and J. Massies, J. Appl. Phys. **86**, 3714 (1999).

[120] N. Grandjean, B. Damilano, J. Massies, G. Neu, M. Teissere, I. Grzegory, S. Porowski, M. Gallart, P. Lefebvre, B. Gil, and M. Albrecht, Appl. Phys. Lett. **88**, 183 (2000).

[121] N. Yoshimoto, T. Matsuoka, T. Sasaki, and A. Katsui, Appl. Phys. Lett. **59**, 2251 (1991).

[122] B. Yang, O. Brandt, B. Jenichen, J. Müllhäuser, and K. H. Ploog, J. Appl. Phys. **82**, 1918 (1997).

[123] T. Nagatomo, T. Kuboyama, H. Minamino, and O. Omoto, Jpn. J. Appl. Phys. **28**, 1334 (1989).

[124] I. Ho and G. B. Stringfellow, Appl. Phys. Lett. **69**, 2701 (1996).

[125] J. M. van Hove, P. P. Chow, A. M. Wowchak, J. J. Klaassen, R. Hickman, and C. Polley, J. Vac. Sci. Technol. B **16**, 1286 (1998).

[126] N. Bertru, O. Brandt, M. Wassermeier, and K. Ploog, Appl. Phys. Lett. **68**, 31 (1996).

[127] O. Brandt, G. E. Crook, K. Ploog, J. Wagner, and M. Maier, Appl. Phys. Lett. **59**, 2730 (1991).

[128] T. Takeuchi, C. Wetzel, S. Yamaguchi, H. Sakai, H. Amano, I. Akasaki, Y. Kaneko, S. Nakagawa, Y. Yamaoka, and N. Yamada, Appl. Phys. Lett. **73**, 1691 (1998).

[129] C. Wetzel, T. Takeuchi, H. Amano, and I. Akasaki, Phys. Rev. B **61**, 2159 (2000).

[130] T. Wang, D. Nakagawa, M. Lachab, T. Sugahara, and S. Sakai, Appl. Phys. Lett. **74**, 3128 (1999).

[131] P. G. Eliseev, P. Perlin, J. Lee, and M. Osiński, Appl. Phys. Lett. **71**, 569 (1997).

[132] Y.-H. Cho, G. H. Gainer, A. J. Fischer, J. J. Song, S. Keller, U. K. Mishra, and S. P. DenBaars, Appl. Phys. Lett. **73**, 1370 (1998).

[133] P. Perlin, C. Kisielowski, V. Iota, B. A. Weinstein, L. Mattos, N. A. Shapiro, J. Krueger, E. R. Weber, and J. Yang, Appl. Phys. Lett. **73**, 2778 (1998).

[134] K. L. Teo, J. S. Colton, P. Y. Yu, E. R. Weber, M. F. Li, W. Liu, K. Uchida, K. Tokunaga, N. Akutsu, and K. Matsumoto, Appl. Phys. Lett. **73**, 1697 (1998).

[135] D. Doppalapudi, S. N. Basu, K. F. Ludwig, and T. D. Moustakas, Appl. Phys. Lett. **84**, 1389 (1998).

[136] M. K. Behbehani, E. L. Piner, S. X. Liu, N. A. El-Masry, and S. M. Bedair, Appl. Phys. Lett. **75**, 2202 (1999).

[137] E. I. Rashba, Sov. Phys. Semicond. **8**, 807 (1975).

[138] B. Damilano, N. Grandjean, J. Massies, L. Siozade, and J. Leymarie, Appl. Phys. Lett. **77**, 1268 (2000).

[139] O. Brandt, J. Ringling, K. H. Ploog, H.-J. Wünsche, and F. Henneberger, Phys. Rev. B **58**, R15977 (1998).

[140] S. Chichibu, T. Sota, K. Wada, and S. Nakamura, J. Vac. Sci. Technol. B **16**, 2204 (1998).

[141] V. Ramachandran, R. M. Feenstra, W. L. Sarney, L. Salamanca-Riba, J. E. Northrup, L. T. Romano, and D. W. Greve, Appl. Phys. Lett. **75**, 808 (1999).

[142] L. T. Romano, J. E. Northrup, A. J. Ptak, and T. H. Myers, Appl. Phys. Lett. **77**, 2479 (2000).

[143] A. Mohammed, C. Trager-Cowan, P. G. Middleton, K. P. O'Donnell, W. Van Der Stricht, I. Moerman, and P. Demeester, Inst. Phys. Conf. Ser. **157**, 235 (1997).

[144] L. Chernyak, A. Osinsky, H. Temkin, J. W. Yang, Q. Chen, and M. A. Khan, Appl. Phys. Lett. **69**, 2531 (1996).

[145] U. Jahn, S. H. Kwok, M. Ramsteiner, R. Hey, H. T. Grahn, and E. Runge, Phys. Rev. B **54**, 2733 (1996).

Danksagung

Es ist mir eine große Freude, auf den letzten Seiten dieser Dissertation meinen tiefen Dank allen auszusprechen, die durch ihre Unterstützung ganz wesentlich zum Gelingen der Arbeit beigetragen haben. Ganz besonders danken möchte ich …

…Prof. Dr. Klaus H. Ploog für sein großes Interesse an dieser Arbeit, seine ständige moralische, fachliche und finanzielle Unterstützung sowie die Organisation einer wichtigen Konferenzreise nach Japan.

…Prof. Dr. Fritz Henneberger, der das Zweitgutachten übernahm und stets an dieser Arbeit interessiert war.

…Prof. Dr. Friedhelm Bechstedt für die Übernahme des Drittgutachtens.

…Dr. Oliver Brandt, dessen Enthusiasmus, Erfahrung und Unterstützung entscheident zum Erfolg dieser Arbeit beitrugen. In zahlreichen Diskussionen in Laboren, unserem gemeinsamen Büro sowie diversen Kneipen hörte er mir mit endloser Geduld zu und lenkte meine Aufmerksamkeit immer wieder auf Aspekte, die mir sonst vielleicht nicht aufgefallen wären. Unsere gemeinsame Begeisterung für irische Kultur und deutsche Sprache prägte viele vergnügliche Abende abseits des Hausvogteiplatzes.

…Andreas Thamm für drei Jahre zusammen verbrachte Zeit im Abenteuerland Wissenschaft, viele unterhaltsame Diskussionen, physikalische Erfahrungsaustausche und gemeinsame Erfolge wie etwa die ungeahnte Perfektion in der Klebetechnik von Substraten. Sowohl in Berlin als auch auf Bildungsreisen erwies er sich als zuverlässiger und ausdauernder Kenner dionysischer Gepflogenheiten.

…Hans-Peter Schönherr, ohne dessen Erfahrung und Sachverstand nicht die für die Optimierung der Schichtqualität nötige große Zahl an Proben zustande gekommen wäre, da er bei technischen Problemen der MBE-Anlage stets die korrekte Lösung parat hatte und diese absolut zuverlässig ausführte.

…Dr. Manfred Ramsteiner, der mit seiner guten Laune eine freundschaftliche Atmosphäre erzeugte und zusammen mit Dr. Manfred Giehler jederzeit ein offenes Ohr für Raman-Messungen hatte.

…Dr. Matthias Wassermeier, dessen hanseatische Art und Optimismus für ein gutes Arbeitsklima sorgten.

…Dr. Lutz Schrottke für seine Geduld und Unterstützung bei allen Problemen mit der Photolumineszenz-Apparatur.

…Dr. Rangarajan Muralidharan für die gemeinsame Optimierung der Wachstumsbedingungen, die eine sichere Basis für die weitere Arbeit darstellte.

…Dr. Uwe Jahn, der mir die Vielfalt von Tokio zeigte und zusammen mit Dr. Johann Menniger die Kathodolumineszenz-Messungen durchführte.

…Björn Rau und Dr. Joachim Puls für die polarisationsabhängigen Photolumineszenz-Messungen sowie Dr. Hans-Jürgen Wünsche für viele Erklärungen zur theoretischen Physik in einer auch für Experimentalphysiker verständlichen Sprache.

…Dr. Achim Trampert, der mir immer mit Begeisterung strukturelle Eigenschaften von Nitriden und TEM-Aufnahmen erläuterte.

…Dr. Helmar Kostial für das vielfältige Prozessieren und Austesten der Homodioden.

…Dr. Holger Grahn für die zeitaufgelösten Photolumineszenz-Messungen an den GaN / (Al,Ga)N Proben.

…Steven Grijsels, der die Elektrolumineszenz-Messungen an den Homodioden durchführte.

…Doris Spaniol, Peter Schützendübe und Michael Höricke für ihre Hilfe bei diversen technischen Fragen.

…Martin Reiche für viele hochauflösende XRD-Messungen.

…Dr. Leander Tapfer für die SIMS-Messungen an den (In,Ga)N / GaN-Proben, die wesentlich zum Verständnis des Segregationsprozesses beitrugen.

…Dr. Martin Kästner, der mich beim Essen und dem täglichen Gang zum Supermarktregal immer über magnetische Materialien auf dem Laufenden hielt und die graphische Benutzeroberfläche des Röntgen-Simulationsprogramms realisierte.

…Ilka Schuster, deren Hilfe die Anfertigung diverser Poster und Folien erheblich erleichterte.

…dem Personal von „Irish Times" und dem „Brechtkeller" für die vorzügliche Bewirtung während all der Nachsitzungen in den letzten Jahren.

…der Volkswagen-Stiftung für die finanzielle Unterstützung.

…der Deutschen Forschungsgemeinschaft, die mir eine wichtige Konferenzreise nach China ermöglichte.

…meiner Mutter Edith Waltereit für die Unterstützung während des Studiums.

…Anja, die mit viel Verständnis manche Entbehrung auf sich nahm.

Lebenslauf

Patrick Waltereit, geb. 7. Dezember 1971 in Münster / Westf.

1978—1982	Grundschule in Hamburg.
1982—1991	Gymnasium in Hamburg.
08 / 1991—10 / 1992	Zivildienst in Hamburg.
10 / 1992—09 / 1994	Grundstudium der Physik an der Universität Hamburg.
10 / 1994—06 / 1995	Erasmus-Stipendiat am Imperial College, London.
10 / 1995—09 / 1996	Hauptstudium an der Freien Universität Berlin.
10 / 1996—09 / 1997	Anfertigung der Diplomarbeit am Interdisciplinary Research Centre (Imperial College, London) in der Arbeitsgruppe von Dr. J. Fernández mit dem Thema *A study of strain relaxed SiGe/Si films by Scanning Force Microscopy and X-Ray Diffraction*, Betreuung: Prof. Dr. M.-Ch. Lux-Steiner.
02 / 1998	Diplomprüfung in Physik (Freie Universität Berlin).
03 / 1998—01 / 2001	Anfertigung der vorliegenden Dissertation am Paul-Drude-Institut für Festkörperelektronik in der Arbeitsgruppe von Dr. O. Brandt, Betreuung: Prof. Dr. K. H. Ploog.

Selbstständigkeitserklärung

Hiermit erkläre ich, die vorliegende Dissertation *(Al,Ga,In)N heterostructures grown along polar and non-polar directions by plasma-assisted molecular beam epitaxy* selbstständig und ohne unerlaubte Hilfe angefertigt zu haben.

Ich habe mich anderwärts nicht um einen Doktorgrad beworben und besitze einen entsprechenden Doktorgrad nicht.

Ich erkläre die Kenntnisnahme der dem Verfahren zugrunde liegenden Promotionsordnung der Mathematisch-Naturwissenschaftlichen Fakultät I der Humboldt-Universität zu Berlin.

Patrick Waltereit

Berlin, 26. Januar 2001